

SCANNING TUNNELING MICROSCOPY STUDY OF DEFECTS AND DEVICES IN
TOPOLOGICAL MATERIALS

By

Michael Gottschalk

A DISSERTATION

Submitted to
Michigan State University
in partial fulfillment of the requirements
for the degree of

Physics – Doctor of Philosophy

September 6, 2022

ABSTRACT

SCANNING TUNNELING MICROSCOPY STUDY OF DEFECTS AND DEVICES IN TOPOLOGICAL MATERIALS

By

Michael Gottschalk

Topological phases in condensed matter systems have received tremendous interest in the past two decades. Theoretical work has shown how topological invariants can be calculated from the band structures in a wide range of insulating systems that contain an energy gap. Broadly speaking, these topological invariants are quantities that are invariant under continuous deformation so long as specific symmetries hold and the energy gap stays open. What separates topological states of matter from traditional phases is the concept of bulk-boundary correspondence. The topology of the vacuum is trivial, so if the bulk of a material is topologically non-trivial, the energy gap must close at the boundary between the two. This creates conducting states at the boundaries, or edges, of the material; the conducting states within the gap have specific properties. Strong, 3D topological insulators, such as Bi_2Se_3 , are materials that are insulating in the bulk with conducting surface states due to bulk-boundary correspondence. The surface states are topologically protected from local perturbations and feature a linear dispersion relation, known as the Dirac cone. Bi_2Se_3 is one of the most widely studied topological insulators due to the relative simplicity of its band structure with a single Dirac cone. In this work, I study the effects of N_2 gas on the surface states of Bi_2Se_3 , which appears to p-type dope the density of states spectra measured with a scanning tunneling microscope. Topological superconductors have also garnered great interest for their potential applications in topological quantum computing. The second half of this dissertation is focused on describing, fabricating, and measuring a potential platform for a possible topological superconducting state known as a Majorana zero mode. These devices feature Nb sputtered on Bi_2Se_3 that is patterned into Josephson junctions with e-beam lithography techniques.

ACKNOWLEDGEMENTS

I have to begin by thanking my wife, Albertina Mays Gottschalk, for standing by me through all of the trials and tribulations in graduate school and before. She helped me get back up when tips would crash and devices would break. We got through the COVID-19 pandemic together in a one bedroom apartment, and we only got a little sick of each other. There have also been great times together! Albertina taught me how to love, laugh, and celebrate. I can't wait to share all of the highs and lows of life with her by my side.

My parents, Bill and Diane Gottschalk, gave me every opportunity to succeed in life. They taught me the value of hard work and gave me the independence to think for myself.

Stuart Tessmer, my advisor, not only taught me how to be a scientist, he showed me the value of kindness and patience in all endeavors. He is not a man who would compromise on his virtues to see results.

Our theory collaborators, Bhanu Mahanti and Malsoon Lee, worked tirelessly with us for years to push the gas exposure study forward. I cannot thank them enough for their hard work.

I would bet that Reza Loloee holds the record for "most acknowledgements in MSU condensed matter physics dissertations." For good reason! His support for the research we do cannot be overstated. All of our cryogenic experiments and many of our devices have been aided by Reza in one way or another.

For four years, Eric Goodwin was my constant companion in the lab. Whether it was making talks for the journal club or staying late to get the microscope pushed down, we always had each other's back. He abandoned me to go work at Northrop Grumman, but I don't hold that against him because I'll be joining him there soon.

The future of the Tessmer group is in Elinore McLain's capable hands. We only had one year together, but she drinks information through a fire hose. I'm confident she will find great success in the future.

Bob Klaes is an interesting character and a fantastic friend. I owe him for getting me and Albertina through the pandemic. Our conversations may not have always been "productive," but they were never dull.

TABLE OF CONTENTS

CHAPTER 1	INTRODUCTION	1
CHAPTER 2	BASIC PRINCIPLES & KEY PHYSICAL THEORIES	4
2.1	Principles of Scanning Tunneling Microscopy	4
2.2	Theory of Topological Band Structures	11
2.3	Theory of Strong, 3D Topological Insulators	18
2.4	Theory of Topological Superconductivity	24
CHAPTER 3	SCANNING TUNNELING MICROSCOPY METHODOLOGY	30
3.1	Microscope Design and Procedures	30
3.2	Cryostat Design and Procedures	33
3.3	Tip Fabrication and Testing	37
CHAPTER 4	GAS EXPOSURE MEASUREMENT METHODOLOGY	41
4.1	Effects of Selenium Vacancies in Bi_2Se_3	41
4.2	Time-Resolved Room Temperature Measurements	45
4.3	Atomic Resolution Topography	47
CHAPTER 5	GAS EXPOSURE RESULTS AND ANALYSIS	49
5.1	Experimental Results	49
5.2	Theoretical Results	52
CHAPTER 6	JOSEPHSON VORTEX EXPERIMENT DESIGN, METHODS AND SIM- ULATIONS	58
6.1	Device Motivation and Design	58
6.2	Device Fabrication	63
6.3	Theoretical Calculations	74
CHAPTER 7	JOSEPHSON VORTEX RESULTS	81
7.1	Device Fabrication Results	81
7.2	Scanning Tunneling Microscopy Results	83
CHAPTER 8	CONCLUSIONS	90

LIST OF FIGURES

Figure 2.1	An example of a classical object encountering a potential barrier. A ball with initial velocity v encounters a hill of height h . If $\frac{1}{2}mv^2 < mgh$, then the ball will not go over the hill. The ball needs kinetic energy in excess of the potential energy of the barrier to reach the other side (neglecting friction and air resistance). This is not the case in quantum mechanics where a particle can tunnel through potential barriers.	5
Figure 2.2	A diagram of the 1D square tunneling barrier problem. The solutions for the Schrodinger equation in regions I and III is a sine wave. Inside of the tunneling barrier, region II, the solution is $\Psi(z) \propto e^{-kz}$. This means that the probability of finding the particle on the other side of the barrier decays exponentially with the width of the barrier. Unlike the classical situation, this probability is non-zero. Adapted from TBD.	6
Figure 2.3	A schematic of a basic STM set-up. The tip position is controlled with piezoelectric tubes. Piezoelectrics are materials that precisely expand and contract with applied voltages, making them ideal for the precision control needed for scanning probe methods. The metallic tip is separated by a few angstroms from the sample. There is a bias voltage applied between the tip and the sample. Scanning the tip over the sample while keeping the tunneling current constant requires the tip-sample separation to be constant. The computer records the position of the tip as it is scanned over the sample to create a 3D topographical image of the surface. Adapted from Ref [39].	8
Figure 2.4	A diagram of the tip and sample states involved in quantum tunneling. The energy, E , is plotted against the density of states, ρ , for both the tip and the sample. The bias voltage causes the Fermi levels in the two materials to misalign. States with energies between E_F and $E_F + V$ are available in the sample for electrons in the tip to tunnel into. The resulting tunneling current is given by equation 2.5.	9
Figure 2.5	A random Hamiltonian parameterized with a single parameter, R . This Hamiltonian has three energy levels $E_n(R)$ that are dependent upon the value of the parameter. With one parameter, the plot is 1D lines embedded in 2D space. In general, with N parameters, the energy levels form an ND manifold embedded in $N+1D$ space.	12

Figure 2.6	A diagram of the classical Hall effect experiment. The thin conducting slab, often referred to as a Hall bar, has a voltage applied along the x -axis. An external magnetic field is applied in the z -axis, creating a Hall voltage, V_H to develop along the y -axis. The geometry shown here is for negative charge carriers. Positive charge carriers would be deflected in the opposite direction. Adapted from TBD.	15
Figure 2.7	A cartoon of electron cyclotron orbits in a 2DEG with an applied out-of-plane magnetic field. Due to the exclusion principle, only two electrons can occupy the same space in the 2DEG. This means that the degeneracy of the Landau levels is dependent on the size of the orbits and therefore the magnetic field. Increasing the magnetic field creates smaller orbits, increasing the degeneracy of the Landau levels. Adapted from Ref [13].	17
Figure 2.8	A diagram of the number of electrons at a given energy in a quantum Hall system. The degeneracy of the Landau levels is dependent on the strength of the magnetic field, so the filling factor, ν , changes with changing magnetic field. Pictured here is the situation with $\nu = 2$. If the magnetic field were to double in magnitude, then the number of electrons that can fit in a Landau level would increase by two-fold. This means that only the bottom Landau level would be occupied with $\nu = 1$	18
Figure 2.9	A diagram demonstrating bulk-boundary correspondence with a quantum Hall system with Chern number $n = 1$. With $n = 1$, a single conducting chiral edge channel forms at the boundary. The number of edge channels is equal to the Chern number. Adapted from [13].	19
Figure 2.10	The periodic table of topological phases. Topological phases are classified by their symmetry class and dimensionality. The symmetries are time-reversal, Θ , particle-hole, Ξ , and chiral, $\Pi = \Xi\Theta$. If the system has a symmetry, it's indicated with ± 1 , where the sign is the value of the symmetry squared. A 0 indicates the system does not have that symmetry. Highlighted in blue are the topological phases discussed in this dissertation. (a) The quantum Hall effect, quantum anomalous Hall effect or Chern insulator. This phase is discussed in Section 2.2. (b) The Kitaev chain. This phase is discussed in Section 2.4. (c) The $p_x + ip_y$ superconductor. This phase is also discussed in Section 2.4. (d) The quantum spin Hall effect. Discussed in this section. (e) The strong, 3D topological insulator. Also discussed in this section. Adapted from Ref [13].	20
Figure 2.11	The helical edge states in the QSHE can be constructed from a Chern insulator with an odd number of chiral edge states and their time-reversed twin. Pictures here is the situation with $N = 1$ chiral edge states.	22

Figure 2.12 An example of the two possible ways states can cross the Fermi level with Kramers degeneracy and time-reversal symmetry. At the Kramers degenerate points Γ_a and Γ_b , the Kramers pairs need to rejoin. (a) The Kramer pairs rejoin in a loop with an even number of Fermi level crossings. These conducting states are not topologically protected. Perturbations could push the loop away from the Fermi level. (b) The Kramer pairs form a connected chain from the valence band to the conduction band with an odd number of Fermi level crossings. These conducting states are topologically protected. Adapted from [13]. 23

Figure 2.13 The Brillouin zone in 3D with time-reversal symmetry. This cube has six faces on which a \mathbb{Z}_2 topological invariant can be defined. The strong topological invariant is only non-trivial if the \mathbb{Z}_2 topological invariants on opposite faces of the cube are different. 24

Figure 2.14 The Dirac cone formed at the boundary of a TI. States with opposite spins from the valence and conduction bands cross the Fermi level with a linear dispersion relation. Adapted from Ref [13]. 25

Figure 2.15 The two ways that Majorana modes can be paired in a 1D chain. (a) Topologically trivial pairing of Majorana modes within fermion modes. (b) Topologically non-trivial pairing of Majorana modes between fermion modes. This leaves two unpaired Majorana modes at the ends of the chain. Adapted from [31]. 27

Figure 2.16 A cartoon of the Majorana braiding operation described by Equation 2.46. Before the braid, the qubit is in the state $|00\rangle$. After the braid, the qubit is in state $\frac{1}{\sqrt{2}}(|00\rangle - i|11\rangle)$ 29

Figure 3.1 (a) A diagram of the sample holder with three ramps. These ramps rest on the carrier piezo-tubes. Applying a voltage to the carrier piezo-tubes causes them to oscillate back and forth, using the inertia of the sample holder to bring the sample closer to the tip step by step. (b) A tip fully installed into the microscope. Vacuum grease keeps the tip attach to its piezo-tube. A gold wire is soldered to the tunneling current lead, creating a conducting path from the tip to the control box. 31

- Figure 3.2 (Color Online) (Green) Glove box, used to prepare samples before loading. (Red) Sample loading arm. This arm allows the sample to be loaded in-situ after being prepared in the glove box. (Orange) Microscope and the top of the cryostat. The full microscope extends out of the picture. After the sample has been loaded and the top of the cryostat has been vacuum pumped, the gate valve can be opened, allowing the microscope to be pushed down into the cryostat. (Blue) Oxford Instruments cryostat. The cryostat is insulated with an outer vacuum chamber. It holds cryogenic liquids in a bath. This bath is thermally connected to the sample space, so the experiments are typically conducted at the same temperature as the boiling point of the cryogenic liquids. 34
- Figure 3.3 A diagram demonstrating the technique for cutting sharp tips. By positioning the Pt/Ir wire close to the end of the vise and using longer lengths of wire, a consistent, sharp bias is created. Moving the cutters in the direction indicated by the arrow helps prevent the tip being blunted by the cutters. 39
- Figure 4.1 The crystal structure of Bi_2Se_3 . A single quintuple layer is highlighted by the box. From bottom to top the five layers are Se, Bi, Se, Bi, Se. The quintuple layers are weakly attracted to each other by Van der Waals forces. Within the quintuple layer, the atoms are covalently bound. Adapted from Ref[41]. 42
- Figure 4.2 Representative tunneling conductance spectroscopy taken on n-type doped Bi_2Se_3 at a temperature of 77K, divided into three distinct regions. Bi_2Se_3 is commonly n-type doped due to selenium vacancy defects. (a) The valence band, characterized by the high density of states. It's estimated here that the valence band ends at -400meV. (b) The Dirac cone which comes to a minimum known as the Dirac point at approximately -280meV. The Dirac cone is characterized by linear density of states as a function of energy. (c) The conduction band, characterized by the high density of states. In n-type doped samples it is common to find the edge of the conduction band close to the Fermi level (0V on the tunneling conductance spectroscopy.) 43
- Figure 4.3 Ref[41]. Calculated level splitting in Bi_2Se_3 with the dashed line indicating the Fermi level. The levels shown here are the p-orbitals closest to the Fermi level from both Bi and Se: Bi ($6s^26p^3$) and Se ($4s^24p^4$). (I) Includes only contributions due to chemical bonding. Highlighted in the box are $|P1^+\rangle$ and $|P2^-\rangle$, which are the levels closest to the Fermi level. The superscripts \pm indicate the parity of the states. Chemical bonding causes these states to hybridize, pushing the Bi level up and the Se levels down. (II) This stage adds contributions due to the crystal field. Here, the z orbitals split off from the x and y orbitals leaving $|P1^+_z\rangle$ and $|P2^-_z\rangle$ at the Fermi level. (III) Finally, the effects of spin-orbit coupling are included. This splits the z orbitals away from the now-combined $x + iy$ orbitals. The two states closest to the Fermi level cross the Fermi level, thereby changing the total ground state parity of the system, driving it into the topological phase. 44

Figure 4.4 (a) First observation of subsurface Se vacancy defects in current imaging tunneling spectroscopy with 30 x 30 nm scan range. The bias voltage was set to -0.45 V, indicating heightened density of states at that energy. These clover-leaf features are due to the effects of the vacancy traveling up the p bonds. (b) Tunneling spectroscopy at various distances from the center of a clover-leaf indicated by numbers in nanometers on the right. These spectra confirm the effect of the defect is to create extra states at -0.45 eV. (c) Observations of the topographic effects of many different Se vacancies. Depending on which Se atom is vacant, the characteristics of the clover-leaf are different. Adapted from Ref[36](a),(b) and Ref[5](c). 45

Figure 4.5 Diagram of the gas exposure experiment. (a) Ultra-high purity (UHP) N₂ source from the building's liquid nitrogen boil-off. (b) UHP He gas cylinder. Both the N₂ and He sources lead to a line going into the flow meter (c). The gas sources can be shut off independently. At least one source is always on to ensure air does not backflow into the glove box (e). The STM (d) is attached to the glove box by flange. 46

Figure 4.6 The glove box used for the room temperature gas exposure experiments. It was designed and built by Joe Kitzman during his summer project in the Tessmer group, so it is frequently referred to as the "Joe Box." Tape is wrapped around the front panel to create a better seal. It's clear that the box is overpressured when the yellow gloves are compressed by the pressure in the box. 47

Figure 5.1 (a) Representative tunneling conductance spectra acquired on Bi₂Se₃ cleaved in He (black) and exposed to N₂ (red) for 35 minutes. These spectra are each an average of 50 curves taken at room temperature at the same sample location with a tunneling barrier established by a -0.5 V bias applied to the sample and a tunneling current set point of 0.3 nA with the tunneling conductance normalized to the value at 0.1 V. The inset is a smaller scale focused on the Dirac points of the two spectra. (b) Tunneling current vs. tip distance from the initial set point measurements demonstrating a robust tunneling barrier throughout the experiment. Both tunneling barriers are calculated to be greater than 5 eV, consistent with the work function of the material. The exponential decay fits are solid lines on the plot. (c) A compilation of identified Dirac point energies taken continuously at the same spot. The crystal was first cleaved in He and spectra were taken at a single location on the surface. $t = 0$ is set when the N₂ gas was introduced to the system. Data taken before the scale break are extracted from averages of 50 spectra. After the scale break, we show a final point representing an average of 800 spectra taken the next day. The dashed line is a phenomenological guide to the eye. . . . 51

- Figure 5.2 STM topographic images. The images were acquired at 77 K with a bias voltage of -0.450 V and a set current of 1 nA. These images have been flattened via polynomial background fitting. (a) Topography shows the triangular spectroscopic signature of sub-surface defects. (b) Atomic resolution topography with indications of surface vacancy defects with a zoomed-in inset showing the atomic resolution. (c) Topography corrected with the autocorrelation function. 52
- Figure 5.3 (a) and (b) Calculated density of states for He and N adsorbed Bi₂Se₃ in the presence of Se vacancy. (c) and (d) DOS calculations corresponding to the energy scale of tunneling measurements. DOS contributions from top layer representing surface atoms and middle layer representing atoms in bulk Bi₂Se₃ are shown. The lowest energy structure of the top quintuple layer of Bi₂Se₃ with a Se vacancy with dopant of (e), (f) He and (g), (h) N are shown where (e) and (g) show top view and (f) and (h) show side view of the structures. Color code: (a)-(d) grey-TDOS, red-*Se* top layer *Se*, blue-Bi top layer, orange-middle layer *Si*, turquoise-middle layer *Bi*, green-dopant.; (e)-(h) magenta - *Bi*, green - *Se*, yellow - *He*, and blue - *N*. 54
- Figure 5.4 (a) is a plot of the change in the Helmholtz free energy of the N₂ molecule as it interacts with the surface. (b) and (c) show a top and side view of the final position of the N atoms, respectively. Color code of atoms: green – *Se*, magenta – *Bi*, blue – *N*. 57
- Figure 6.1 (a) Diagram of an S-TI-S Josephson junction. According to the Fu-Kane theory, a linearly dispersing 1D line of Majorana modes forms along the *x*-axis in the junction when the phase difference across the junction $\phi = \pi$. The plan for the experiment is to study vortices in such junctions which theoretically support Majorana zero modes. (b) The dispersion relation for the 1D Majorana modes forms the solid black lines crossing zero energy. The dashed lines are the same modes with the addition of a mass term. (c) An S-TI-S tri-junction. This geometry is proposed as a viable platform for exchanging Majorana zero modes. (d) A phase diagram for the tri-junction. Majorana modes form in the junction when the phase relationship of the three superconductors lies within the grey regions. Adapted from Ref [8]. 60

Figure 6.2	<p>The experimental results of Roditchev and collaborators from Ref [28]. (a) Topography of the surface along with a schematic. Pb islands are clearly imaged along with the wetting layer (WL). (b) A tunneling conductance map on the surface with no applied magnetic field at zero bias. As expected, the tunneling conductance on the superconducting islands is suppressed at zero bias due to the formation of the superconducting energy gap. The superconducting proximity effect opens a gap in the normal metal WL close to the islands. (c) A tunneling conductance map on the surface with a 60 mT applied external magnetic field. The superconducting gap closes as vortices form on and between the islands. Tunneling conductance returns to the baseline level observed in the normal metal far from an island. (d) A plot of tunneling conductance as a function of energy at various locations on the surface: the superconducting islands (S), the normal metal wetting layer (WL) far from an island, a point between two islands (J), and a point close to a single island (P). (e) Plots of tunneling conductance as a function of energy between two islands with no applied field. (f) Plots of tunneling conductance as a function of energy between two islands with 60 mT applied magnetic field.</p>	62
Figure 6.3	<p>My experimental plan, inspired by the theoretical work in Ref [8] and the experimental work in Ref [28]. S-TI-S Josephson junctions are formed with 30 nm thick Nb fingers (S) on 20 QL of Bi₂Se₃ (TI.) The fingers are 500 nm wide and are spaced 300 nm apart. An external magnetic field creates vortices between the superconducting Nb. The experimental signature is distinct from that in Figure 6.2 (f) in that the Majorana zero modes could create additional conductance at zero energy above the baseline. This means that tunneling conductance as a function of bias voltage would show a peak at zero bias rather than simply a diminished energy gap.</p>	63
Figure 6.4	<p>Film thicknesses for various negative e-beam resists. The spin time is 30s for all curves. The thickness of maN-2401 after 30s at 3000 rpm is 0.1 μm. Adapted from Ref TBD.</p>	64
Figure 6.5	<p>(Top) This is the condition of the device when I begin my portion of the device fabrication process. This is 20 QL of Bi₂Se₃ grown via molecular beam epitaxy with 30 nm of sputtered Nb mounted on a sapphire substrate. (Bottom) This is the condition of the device after spin-coating with resist. ma-N 2401 is a negative e-beam resist. Negative resist remains on the sample after patterning and developing. The role of the resist is to protect portions of the Nb during etching.</p>	65
Figure 6.6	<p>(Top) This is the state of the device after patterning and developing. The resist that was exposed by the e-beam during patterning is insoluble, so it remains on the surface of the sample. (Bottom) This is the state of the device after RIE. The resist protects the Nb during etching leaving the Nb patterned into the desired geometry.</p>	67

Figure 6.7	Amount of Nb etched as a function of time. This process used CBrF ₃ plasma instead of CF ₄ . It's clear that there is a delay before the etching process takes off. The parameters of the RIE should be selected such that the Nb is quickly etched away after the delay. This makes it easier to terminate the process before the plasma begins to etch the Bi ₂ Se ₃ . Adapted from Ref [1].	68
Figure 6.8	The completed device after removing the remaining e-beam resist.	70
Figure 6.9	An example of ideal amplitude and phase response as a function of driving frequency. The amplitude should peak at the resonant frequency while the phase resembles a sigmoid function. Adapted from Ref [40].	72
Figure 6.10	A diagram of a 3 x 3 array of line junction array elements. Arrays used for the experiment are 20 x 20. The array elements are 50 x 50 μm with a 10 μm buffer region between them. The buffer region is simply Bi ₂ Se ₃ with no Nb on top.	73
Figure 6.11	A plot of conductance in units of conductance quanta as a function of energy in units of $t = \frac{\hbar^2}{2a^2m}$. The system is a quantum wire, and the plot shows the expected quantized conductance steps.	77
Figure 6.12	(Left) An electron density map at zero energy over sites in a tight-binding model using Equation 6.11 with a spatially varying phase. The density map was calculated in the Kwant Python package using a kernel polynomial method (KPM). There is noise in the calculation due to the fact that the KPM uses random vectors. The system is divided into two regions. For sites with $x < 0$ the phase is set to $\phi = 0$. Sites with $x > 0$ have phase $\phi = y2\pi/W + \pi$ where $W = 60$ is the width of the system. This means that the phase difference varies linearly along the width of the system from 0 to 2π . The phase offset is chosen such that $\phi = \pi$ in the center of the system. We observe a bright region in the junction where $\phi = \pi$, indicating enhanced density of states at zero energy. (Right) A plot of the density of states as a function of energy in units of the superconducting gap Δ . This plot was taken by averaging together the contributions of the 5 central sites from the map on the left. We see that there is a peak in the DOS at zero energy. This is the expected experimental signature in future studies on these system.	79

- Figure 6.13 (Left) An electron density map at zero energy over sites in a tight-binding model using Equation 6.11 with a spatially varying phase. The density map was calculated in the Kwant Python package using a kernel polynomial method. The system is divided into three regions with three different superconducting phases. All sites with $y < 0$ have $\phi = 0$, sites with $y > 0$ and $x < 0$ have $\phi = \phi_1 = \pi/2$, and sites with $y > 0$ and $x > 0$ have $\phi = \phi_2 = 3\pi/2$. This puts the junction into the shaded region of phase space shown in Figure 6.1(d) that corresponds to the topological state. We observe a bright spot in the junction when the phases are tuned to lie in this region, indicating enhanced density of states at zero energy. (Right) Tri-junction diagram adapted from [8]. 80
- Figure 7.1 3D image of tapping mode AFM topography on an early S-TI-S device made with 30 nm of Nb sputtered on Bi_2Se_3 . The Nb is $50 \mu\text{m}$ long, $0.35 \mu\text{m}$ wide, spaced $0.15 \mu\text{m}$ apart. This topography shows the edge of an array element so that the depth of the fingers can be compared with the Bi_2Se_3 buffer region. We can see that the Nb fingers have small gaps partially filled in with tapered edges. This device was made before the recipe was finalized. We can see clear evidence of leftover resist on the six fingers on the right side of the image. 83
- Figure 7.2 Tapping mode AFM topography on an S-TI-S device made with 30 nm of Nb sputtered on Bi_2Se_3 . The Nb is $50 \mu\text{m}$ long, $0.5 \mu\text{m}$ wide, spaced $0.3 \mu\text{m}$ apart. This device was made after the recipe was finalized. (Left) A wide-range $20 \times 20 \mu\text{m}$ scan showing the quality of the device over large distance scales. (Right) 3D image of $3.6 \times 3.6 \mu\text{m}$ topography taken from the region highlighted in green. Small-range topography is necessary to get detailed images of the junctions. The fingers are fully separated, and the height of the topography in the junctions is the same as the buffer region, indicating that the Nb in the junctions fully etched. 84
- Figure 7.3 (Left) Short-range AFM topography on the highlighted region in Figure 7.2. This image was corrected with a standard 3-point flattening procedure and polynomial background correction. (Right) The height profile along the green line in the topography image. The Nb is $30 \pm 1 \text{ nm}$ tall. This indicates that virtually no Bi_2Se_3 was etched. 84
- Figure 7.4 A completed device mounted on an STM sample disc. This device is adhered to the sample disc with vacuum grease, so we can move the device laterally when aligning the STM tip. The device is on an insulating sapphire substrate, so there needs to be a conducting path from the surface of the device to the sample disc. This is accomplished with a gold wire silver painted to the sample disc and the device. The $1.2 \times 1.2 \text{ mm}$ array of junctions is visible to the naked eye from certain angles. It's almost impossible to see the junctions after the sample disc is loaded in the microscope, so I used silver paint to frame the array. 85

Figure 7.5 A photo taken with a Samsung Galaxy S22 Ultra at 100x zoom of a completed device loaded into the STM. The array is invisible to the naked eye, but the silver paint provides land marks to guide me during alignment. It's ideal for the device to be properly aligned while the sample disc is in the full +Y direction, so that during low temperature experiments, there is a simple prescription to find the area of interest. 86

Figure 7.6 (Left) Room temperature STM $1 \times 1 \mu\text{m}$ topography on an S-TI-S device. STM topography is higher-resolution than AFM topography, but the scan range is more limited. STM topography is also generally noisier than AFM topography at room temperature. At room temperature, it is possible to fit two fingers in one scan window. (Right) The height profile along the green line in the topography image. The Nb is $32 \pm 3 \text{ nm}$ tall, as expected. 88

Figure 7.7 (Left) STM topography on the edge of a Nb finger at 4.2 K. The topography shows an extended, sloping edge of the finger. (Right) The height profile along the green line in the topography image. 88

Figure 7.8 (Left) The same STM topography as shown in Figure 7.7. A green star shows a single spectroscopy location. (Right) STM spectroscopy taken at the green star. In black is the experimental data showing a clear gap at zero bias. A theoretical BCS spectroscopy is plotted in red. The theory uses the mean free path of the Cooper pairs as the only free parameter with the superconducting energy gap at zero temperature fixed at the nominal value for Nb at $\Delta = 3.05 \text{ meV}$ and the temperature fixed at $T = 4.2 \text{ K}$ 89

CHAPTER 1

INTRODUCTION

This work is centered around two experiments exploring topological phases in condensed matter physics. The first experiment presents evidence for a novel N_2 gas exposure effect on the 3D topological insulator (3D TI), Bi_2Se_3 . The second experiment centers around a proposed topological superconductor platform with superconductor-TI-superconductor (S-TI-S) Josephson junctions. These experiments are explained over the course of eight chapters, including the introduction (Chapter 1) and conclusions (Chapter 8).

Chapter 2 provides background information necessary to understand the experimental techniques and systems. It starts with the principles of scanning tunneling microscopy (STM), the main experimental probe. Many features of STM can be understood from a basic understanding of quantum tunneling. Knowing just that the quantum tunneling probability falls off exponentially with distance goes a long way in explaining the STM's ability to create topographic images of material surfaces. The chapter goes on to explain how this picture becomes less clear when the atomic details of surfaces and probe are considered. The rest of the chapter is devoted to explaining topological phases in condensed matter systems. It begins with geometric (Berry) phase, a quantity calculated over closed curves in the parameter space of parameter-dependent Hamiltonians. A related quantity, Berry curvature, can be used to calculate the topological invariant for quantum Hall effect systems, the Chern number. Chern numbers are also a good framework for calculating the topological invariant in quantum spin Hall effect (QSHE) systems. 3D TIs are shown to be a natural extension of the QSHE to three dimensions. Finally, I give an introductory look at topological superconductivity and Majorana zero modes (MZMs). MZMs are zero energy states on the boundaries of topological superconductors with the unique property of non-Abelian exchange statistics. Non-Abelian in this context means that exchanging the positions of MZMs is a non-commuting operation. This has potential applications for topological quantum computation.

Chapter 3 explains the STM implementation in the Tessmer lab, the cryostat design, and the tip-cutting procedures. The procedures common among all of the STM measurements are shared here. These details will help the reader understand not only how the experiments were done but how they were designed. In the first section, the advantages and limitations of the Besocke STM design are explored. One of the advantages is the large, lateral coarse positioning range. This advantage turns into a disadvantage when looking for a small region of interest on a large sample. The next section explains the cryostat procedures, how it is cooled, and how samples are loaded. These details are key in STM experiments where a clean surface is vital. Finally, I share the tip fabrication and testing process. Tips are mechanically cut by hand with wire cutters. Cutting consistently sharp tips requires a carefully-controlled technique. A sharp tip and a good sample are the two most critical components of an STM experiment.

Chapter 4 features the methodology of the gas exposure experiment, along with some more background information on Bi_2Se_3 and the role Se vacancies play in the spectra of electronic states in the material. The primary measurement was carried out at room temperature in an overpressured glove box. Initially, the glove box was overpressured with He to create an inert baseline environment. Tunneling spectroscopy measurements were acquired while N_2 gas flowed into the glove box. The results are presented in Chapter 5. We observed a positive shift in the Dirac point energy in the Bi_2Se_3 spectra over time. These results are explained theoretically by N_2 binding to Se vacancy pairs on the surface of the material.

Chapter 6 explains the proposed topological superconductor devices. It begins with an explanation of the inspiration for the experiment in the literature. Theory suggests that vortices in S-TI-S Josephson junctions may support MZMs. Experiments have been conducted in the literature studying normal metal (SNS) Josephson vortices. The vortices were imaged with an STM creating a tunneling conductance map of the surface. Vortices show up as a closing of the superconducting energy gap in that system. The situation changes slightly for an S-TI-S Josephson vortex where it's expected that there is a conductance peak at zero bias, based on simulations I carried out utilizing

the theoretical models in the literature. To fabricate these devices, I used e-beam lithography (EBL) and reactive ion etching (RIE). Developing the recipe for the devices required many iterations. The results of the device fabrication process are shared in Chapter 7. AFM images show that Nb fingers on Bi_2Se_3 are in the geometry required for imaging line junctions in our STM setup. STM spectroscopy confirms that the thin-film Nb is superconducting at 4.2 K. Future work in the Tessmer group will be done to look at vortices in these devices.

CHAPTER 2

BASIC PRINCIPLES & KEY PHYSICAL THEORIES

The chapter provides the background information necessary to understand the experimental techniques, design, and the underlying physics. There are four sections. The first section explains the theoretical principles of scanning tunneling microscopy (STM) and how they can be applied to topographical and spectroscopic measurements. Next, there is a section on the general theory of topological band structures. Here, we see how Berry phase can be used to calculate the topological invariant in the quantum Hall effect: the Chern number. In the next section this concept is extended to systems with different symmetries and dimensionality, the quantum spin Hall effect and the strong, 3D topological insulator (3D TI). The final section explores the boundaries of topological superconductors which theoretically support exotic quasiparticles known as Majorana zero modes (MZMs). These final two systems, the 3D TI and MZMs, are the systems studied throughout the rest of the dissertation. The discussions of Berry phase, quantum Hall effect, and quantum spin Hall effect are included to provide a more complete understanding of MZMs and 3D TIs.

2.1 Principles of Scanning Tunneling Microscopy

One of the surprising results from the development of quantum mechanics is quantum tunneling. Quantum tunneling refers to the fact that when measuring a particle's position, there is a finite probability that the particle is measured on the other side of a potential barrier. In classical mechanics, for a particle to move past a potential barrier, it needs to have kinetic energy greater than the potential barrier. The potential barrier will slow down the particle as kinetic energy is transformed into potential energy and the particle can emerge on the other side. This makes intuitive sense when one considers how this process plays out in gravitational potentials. A ball at the bottom of a hill of height h needs to overcome a gravitational potential energy of approximately mgh where m is the mass of the ball and g is the acceleration due to gravity. If the ball has kinetic energy of $\frac{1}{2}mv^2 > mgh$, it will have enough energy to roll over the hill (ignoring losses due to air

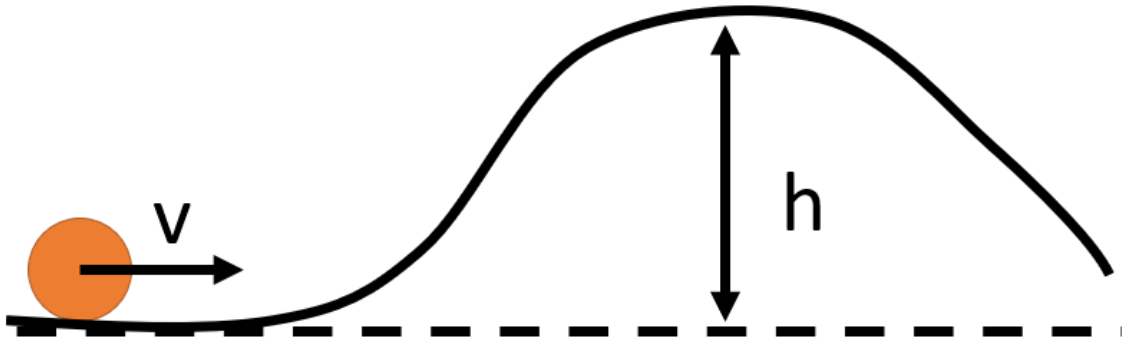


Figure 2.1 An example of a classical object encountering a potential barrier. A ball with initial velocity v encounters a hill of height h . If $\frac{1}{2}mv^2 < mgh$, then the ball will not go over the hill. The ball needs kinetic energy in excess of the potential energy of the barrier to reach the other side (neglecting friction and air resistance). This is not the case in quantum mechanics where a particle can tunnel through potential barriers.

resistance and friction.)

The situation is completely different in quantum mechanics. In quantum mechanics, the outcomes of position measurements on a particle are probabilistically determined by the absolute value of the wavefunction squared $|\Psi(x)|^2$, a complex function. In the most basic formulation, the wavefunction is determined by the time-independent Schrodinger equation,

$$H\Psi = E\Psi. \quad (2.1)$$

Here H is the Hamiltonian. The Hamiltonian is an operator that acts on the wavefunction, and the wavefunction solutions to the Schrodinger equation are eigenfunctions of this operator. For a particle in one dimension, z , $H = \frac{-\hbar^2\partial_z^2}{2m} + V(z)$. There are some simple potentials in which this equation can be solved exactly. One such potential is the square potential barrier:

$$V(z) = \begin{cases} 0 & \text{if } z < 0 \\ V_B & \text{if } 0 \leq z \leq d \\ 0 & \text{if } z > d. \end{cases} \quad (2.2)$$

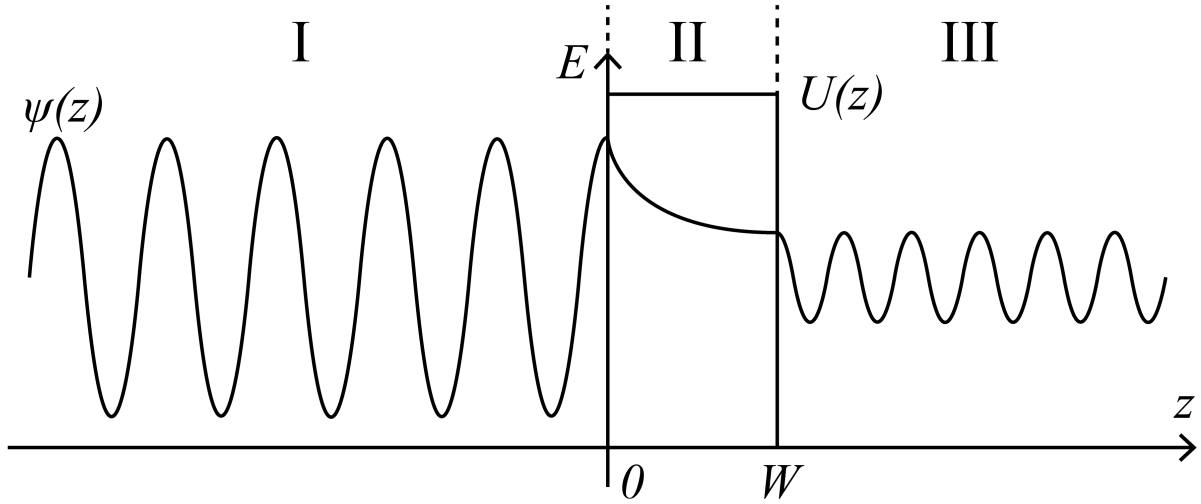


Figure 2.2 A diagram of the 1D square tunneling barrier problem. The solutions for the Schrodinger equation in regions I and III is a sine wave. Inside of the tunneling barrier, region II, the solution is $\Psi(z) \propto e^{-\kappa z}$. This means that the probability of finding the particle on the other side of the barrier decays exponentially with the width of the barrier. Unlike the classical situation, this probability is non-zero. Adapted from TBD.

Here the potential barrier $V_B > E$. It's a simple exercise to show that the solution to Equation 2.1 in the barrier region, $0 \leq z \leq d$, is then:

$$\Psi(z) \propto e^{-\kappa z}, \quad (2.3)$$

where κ is defined to be $\kappa^2 = \frac{2m}{\hbar^2}(V_B - E)$. In contrast with the classical situation where the particle would be unable to overcome the potential barrier, the quantum particle has a finite probability to be measured on the other side. This probability diminishes exponentially with the width of the potential barrier.

STM topography is based on this exponential dependence. Electrons in a metal tip close to the sample surface of the material are able to tunnel through the potential barrier of the vacuum and into the surface. These electrons will create a tunneling current, I , proportional to $|\Psi|^2$ in the sample, resulting in:

$$I \propto e^{-2\kappa d}. \quad (2.4)$$

Here d is the distance between the tip and the sample. This tunneling current only develops if there are available electronic states for the electrons to tunnel into. If the tip and sample are at the same electric potential, the Fermi levels in the two materials will match each other at equilibrium. This means that there are no open electronic states for the electrons to tunnel into without changing energy. An applied voltage between the tip and sample moves their Fermi levels relative to each other. Ideally, the tunneling current can be approximated with this relationship:

$$I(V) \propto \int_{E_F}^{E_F+V} \rho(E)T(E, V)dE. \quad (2.5)$$

$T(E, V)$ is the transmission barrier coefficient which includes the effects of the potential barrier between the tip and the sample and the details of the wave functions on each side of the barrier. $\rho(E)$ is the density of electronic states in the sample material. The density of states in the metallic tip is assumed to be approximately constant in the energy ranges typical for STM (± 1 eV). Equations 2.4 and 2.5 taken together mean that with a constant bias voltage and a constant current set point, the tip and sample must be a constant distance apart from each other. By scanning the tip over the surface while maintaining a constant current, a 3D image of the surface is produced. The exponential dependence of the tunneling current makes this topographical mapping method highly sensitive to variations in the height of features on the surface of the sample. At low voltages, $T(E, V)$ is approximately flat, so Equation 2.5 implies that measurements of dI/dV as a function of V are directly proportional to the spectrum of the sample's density of states, ρ , as a function of energy in units of eV, shown in equation 2.6. This is a powerful measurement technique utilized in many of our experiments.

$$\frac{dI}{dV} \propto \rho(E) \quad (2.6)$$

STM is sensitive enough to resolve individual atoms in topography measurements. Understanding atomic-resolution topography requires going beyond the simple model of Equation 2.4. In particular, it's ambiguous what the tip-sample separation, d , means in an atomic context. After all, the locations of electrons are not well-described by a single number, and the tip is not a single point

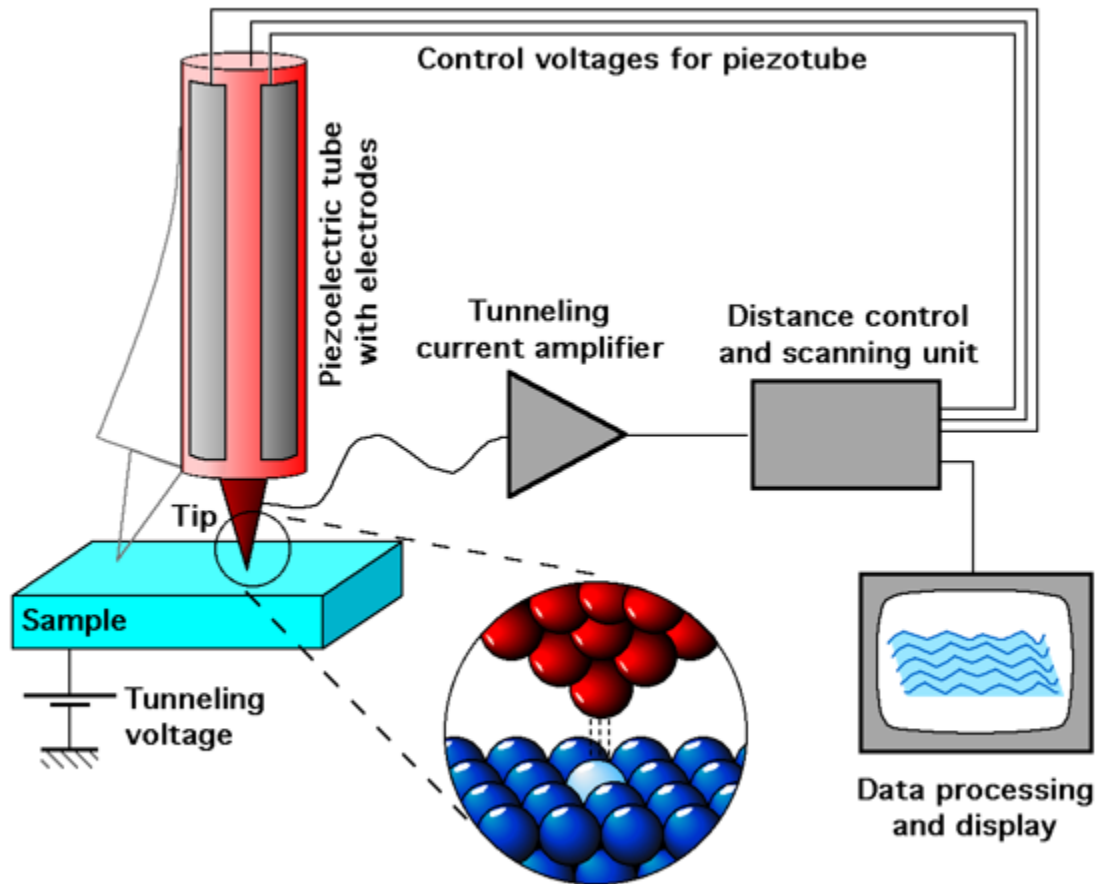


Figure 2.3 A schematic of a basic STM set-up. The tip position is controlled with piezoelectric tubes. Piezoelectrics are materials that precisely expand and contract with applied voltages, making them ideal for the precision control needed for scanning probe methods. The metallic tip is separated by a few angstroms from the sample. There is a bias voltage applied between the tip and the sample. Scanning the tip over the sample while keeping the tunneling current constant requires the tip-sample separation to be constant. The computer records the position of the tip as it is scanned over the sample to create a 3D topographical image of the surface. Adapted from Ref [39].

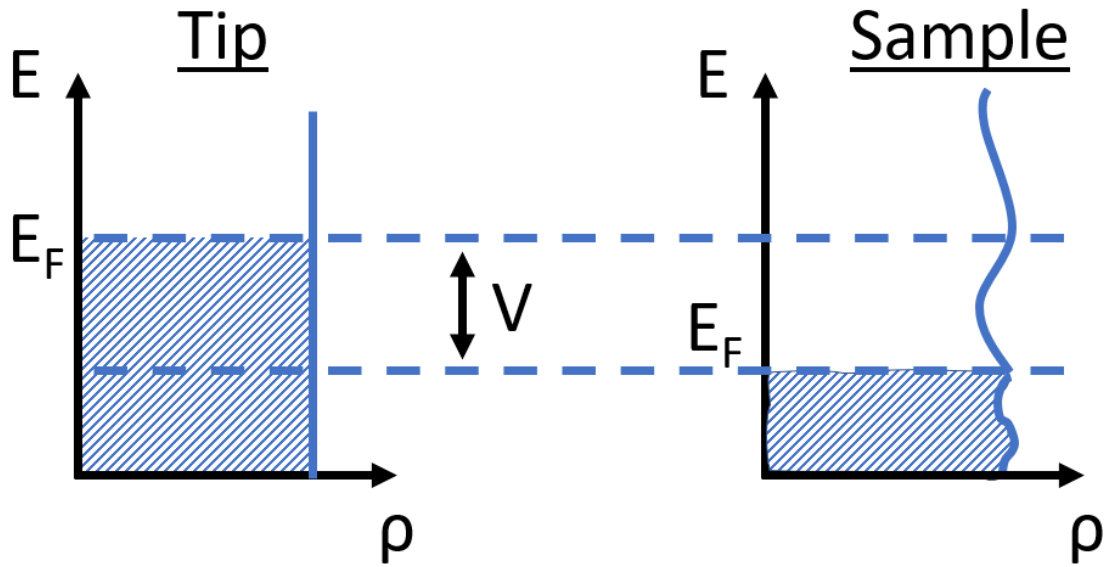


Figure 2.4 A diagram of the tip and sample states involved in quantum tunneling. The energy, E , is plotted against the density of states, ρ , for both the tip and the sample. The bias voltage causes the Fermi levels in the two materials to misalign. States with energies between E_F and $E_F + V$ are available in the sample for electrons in the tip to tunnel into. The resulting tunneling current is given by equation 2.5.

in space. Even the concept of "topography" is poorly defined at this scale. What, then, is being measured in atomic-resolution STM imaging?

The measurement method is the same as described earlier, so to understand atomic-resolution topography we need to understand how the tunneling current would depend on the features of the sample. Exact modeling of the interactions of the tip and sample are highly complex; however, with typical separation distances, the system can be treated as weakly coupled and analyzed with perturbation theory. The tunneling current in the first order of perturbation theory is:

$$I = \frac{2\pi e}{\hbar} \sum_{\mu,\nu} \{f(E_\mu)[1 - f(E_\nu)] - f(E_\nu)[1 - f(E_\mu)]\} |M_{\mu\nu}|^2 \delta(E_\nu + V - E_\mu) \quad (2.7)$$

Here the subscripts μ, ν differentiate between the two sides of the tunneling barrier (tip and sample). $f(E)$ is the Fermi occupation function of electronic states, V is the applied voltage, $M_{\mu\nu}$ is the tunneling matrix element between states ψ_μ and ψ_ν . At low temperatures, the Fermi occupation

function is approximated with a step function giving us:

$$I = \frac{2\pi}{\hbar} e^2 V \sum_{\mu, \nu} |M_{\mu\nu}|^2 \delta(E_\mu - E_F) \delta(E_\nu - E_F) \quad (2.8)$$

This expression is simple to understand, with the exception of the tunneling matrix elements. Bardeen showed that the tunneling matrix elements can be expressed as [2]:

$$M_{\mu\nu} = \frac{\hbar^2}{2m} \int d\mathbf{S} \cdot (\psi_\mu^* \nabla \psi_\nu - \psi_\nu \nabla \psi_\mu^*) \quad (2.9)$$

The integral is over any surface lying entirely inside of the tunneling barrier between the tip and the sample. We see then that the matrix elements depend on the wavefunctions from the tip and sample in the tunneling barrier region. Writing these wavefunctions as plane waves and substituting into the previous equation gives us:

$$M_{\mu\nu} = -\frac{4\pi^2 \hbar^2}{m} \int d\mathbf{q} a_q b_q^* \kappa_q e^{-\kappa_q z_t} e^{i\mathbf{q} \cdot \mathbf{x}_t} \quad (2.10)$$

Here \mathbf{q} is the momentum, a_q and b_q^* are normalization constants in the tip and sample, κ_q is defined as $\kappa_q^2 = \kappa^2 + |\mathbf{q}|^2$, z_t and \mathbf{x}_t are the vertical and lateral components of the tip position, respectively. This expression recovers the exponential fall-off of the tunneling current as a function of tip-sample separation in $e^{-\kappa_q z_t}$, and it accounts for lateral variations in the electron density over the surface. For an ideal tip modeled a point source of current at position \mathbf{r}_t . Equation 2.8 reduces to

$$I \propto \sum_{\nu} |\psi_\nu(\mathbf{r}_t)|^2 \delta(E_\nu - E_F) \equiv \rho(\mathbf{r}_t, E_F) \quad (2.11)$$

at small voltages. $\rho(\mathbf{r}_t, E_F)$ is the local density of states at the Fermi level in the material. In this picture, an ideal STM is purely measuring the charge density in the material without needing to consider the full tip-sample system. This picture is surprisingly applicable to tips with a finite radius of curvature by designating \mathbf{r}_t to be the location at the center of curvature.

The discussion up to this point has assumed a uniform, flat tunneling barrier between the tip and the sample. This is a convenient approximation; however, the tunneling barrier is not flat.

It's distorted by the mismatch in Fermi levels of the two materials and the applied voltage. The apparent barrier height is defined as

$$\phi_A \equiv \frac{\hbar^2}{8m} \left(\frac{d \ln I}{dz} \right)^2 \quad (2.12)$$

In the ideal case, the tunneling current has an exponential dependence on the tip-sample separation, so $\frac{d \ln I}{dz}$ would be independent of z . Experiments have shown that in the limit $z \rightarrow \infty$, $\phi_A(z) \rightarrow \Phi_{avg}$, the average of the tip and sample work functions. Hence, measuring the tunneling current as a function of z provides a direct measure of the apparent tunneling barrier.

2.2 Theory of Topological Band Structures

We begin our discussion of topological band structures by considering Berry phase or geometric phase. Geometric phase is a phase acquired by a particle during adiabatic time evolution. The unitary time evolution operator, $U_T(t) = e^{iHt/\hbar}$ generates a dynamical phase of $\theta_T(t) = Et/\hbar$ when applied to eigenstates of the Hamiltonian. This is not valid, however, if the Hamiltonian is explicitly time varying. Berry phase allows for a time-varying Hamiltonian. A general, time-varying Hamiltonian can be written as $H(\mathbf{R})$ where $\mathbf{R} = (R_1, R_2, \dots)$ is a generic set of N parameters upon which the Hamiltonian explicitly varies. These parameters are free to evolve in time. The adiabatic theorem states that for slowly varying Hamiltonians, particles starting in the n th eigenstate will remain in the n th eigenstate:

$$H(\mathbf{R}) |n(\mathbf{R})\rangle = E_n(\mathbf{R}) |n(\mathbf{R})\rangle. \quad (2.13)$$

This eigenvalue equation is defined in the N -dimensional parameter space over the range of possible values for the parameters. If the parameter space has one dimension, the energy eigenvalues, $E_n(\mathbf{R})$ can be plotted as lines in a 2D space, (one dimension for the parameters and another for the energy) as shown in Figure 2.5. For a two-dimensional parameter space, this plot would be 2D surfaces embedded in 3D space. In general, they form an N -dimensional manifold embedded in $N+1$ -dimensional space. We are interested in the time evolution of a wavefunction in this manifold $|\psi(t)\rangle = e^{-i\theta(t)} |n(\mathbf{R}(t))\rangle$. Due to the adiabatic theorem, $|\psi(t)\rangle$ remains in the $|n(\mathbf{R}(t))\rangle$ orbital,

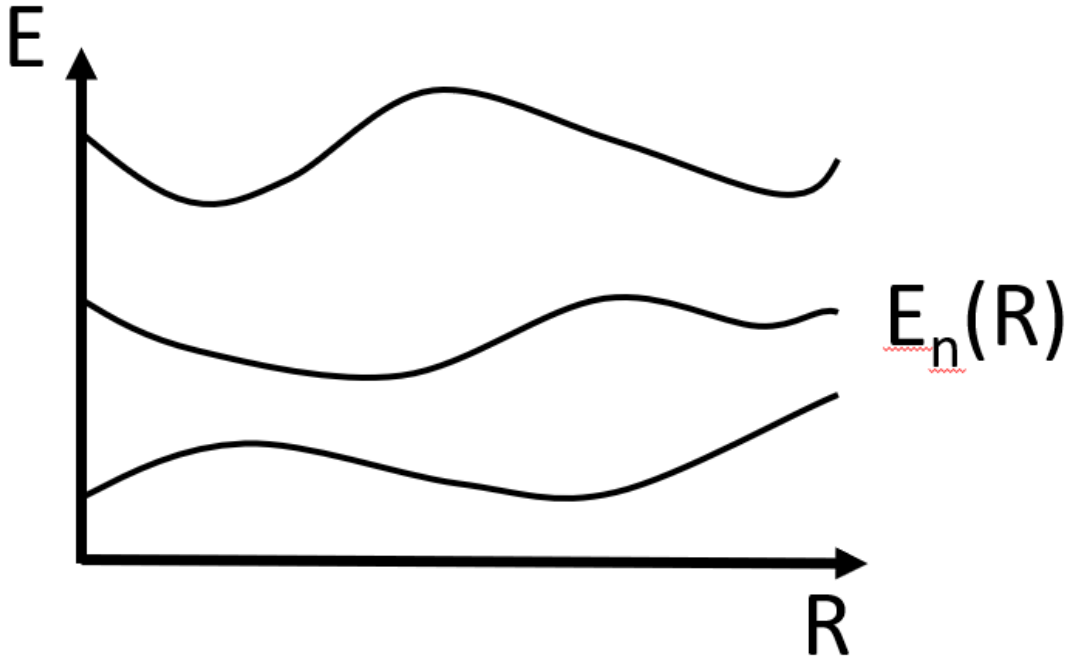


Figure 2.5 A random Hamiltonian parameterized with a single parameter, R . This Hamiltonian has three energy levels $E_n(R)$ that are dependent upon the value of the parameter. With one parameter, the plot is 1D lines embedded in 2D space. In general, with N parameters, the energy levels form an N D manifold embedded in $N+1$ D space.

but its phase, $\theta(t)$ is free to change. $\theta(t)$ must at least include the dynamical phase. Berry's insight was that the phase includes a geometric component, as well.

To explore the time-evolution of $|\psi(t)\rangle$, we begin by writing the time-dependent Schrodinger equation for $|\psi(t)\rangle$:

$$H(\mathbf{R}(t)) |\psi(t)\rangle = i\hbar \frac{d}{dt} |\psi(t)\rangle \quad (2.14)$$

Acting on $|\psi(t)\rangle$ with H and expanding $|\psi(t)\rangle$ into $e^{-i\theta(t)} |n(\mathbf{R}(t))\rangle$ we get:

$$E_n(\mathbf{R}(t)) |n(\mathbf{R}(t))\rangle = \hbar \left(\frac{d}{dt} \theta(t) \right) |n(\mathbf{R}(t))\rangle + i\hbar \frac{d}{dt} |n(\mathbf{R}(t))\rangle \quad (2.15)$$

Mutiplied on the left by $\langle n(\mathbf{R}(t))|$ and assuming the states are normalized at all t gives us:

$$E_n(\mathbf{R}(t)) - i\hbar \langle n(\mathbf{R}(t))| \frac{d}{dt} |n(\mathbf{R}(t))\rangle = \hbar \left(\frac{d}{dt} \theta(t) \right) \quad (2.16)$$

We are interested in finding the phase $\theta(t)$. All that is left to do is rearrange and integrate to get:

$$\theta(t) = \frac{1}{\hbar} \int_0^t E_n(\mathbf{R}(t')) dt' - i \int_0^t \langle n(\mathbf{R}(t')) | \frac{d}{dt'} | n(\mathbf{R}(t')) \rangle dt' \quad (2.17)$$

The first term is the dynamical phase from $U_T(t) = e^{iHt/\hbar}$, giving us $\theta_T(t) = \frac{1}{\hbar} \int_0^t E_n(\mathbf{R}(t')) dt'$.

The remaining term is the Berry phase:

$$\gamma_n(t) = i \int_0^t \langle n(\mathbf{R}(t')) | \frac{d}{dt'} | n(\mathbf{R}(t')) \rangle dt' \quad (2.18)$$

This phase is often referred to in the literature as the geometric phase, as it depends only on the geometry of the eigenstates as they evolve along a path C in parameter space. In fact, explicit time evolution can be removed from the definition of Berry phase:

$$\gamma_n = i \int_C \langle n(\mathbf{R}) | \nabla_{\mathbf{R}} | n(\mathbf{R}) \rangle d\mathbf{R} \quad (2.19)$$

The Berry phase is only gauge-independent (and therefore physical) if this path is closed. Such an integral over a closed path is reminiscent of electromagnetism. Indeed, we can define a vector potential, called the Berry connection:

$$\mathbf{A}_n(\mathbf{R}) = i \langle n(\mathbf{R}) | \frac{\partial}{\partial \mathbf{R}} | n(\mathbf{R}) \rangle \quad (2.20)$$

The Berry phase can be calculated by integrating this vector potential over closed paths:

$$\gamma_n = \int_C d\mathbf{R} \cdot \mathbf{A}_n(\mathbf{R}) \quad (2.21)$$

Berry phase has a wide range of applications. The discussion up to the point has been very general. For most applications of Berry phase, we can restrict our discussion to 3D parameter spaces, as the parameters are usually 3D position space or 3D momentum space. 3D momentum space is of particular interest in solid state physics. One of the most powerful advances in solid state physics was the development of band theory. This relies on utilizing the periodic symmetry in crystals. Crystals are comprised of unit cells that can be translated onto each other with unit vectors. In band theory, the electronic states in a crystal are described with Bloch wave functions:

$$\psi_{(l,n)} = e^{ikn} u_l. \quad (2.22)$$

The l index indicates the orbital within a unit cell, \mathbf{n} is a vector of integers describing the location of the unit cell, u_l is the part of the wavefunction that repeats in each unit cell, and \mathbf{k} is the crystal momentum periodically defined in the Brillouin zone such that $0 \leq k_i \leq 2\pi$ and $k_i(0) = k_i(2\pi)$ (with the lattice spacing conveniently defined to be 1). The Hamiltonian can be parameterized with \mathbf{k} , giving us the Bloch equation,

$$H(\mathbf{k})u(\mathbf{k}) = E(\mathbf{k})u(\mathbf{k}), \quad (2.23)$$

which is highly reminiscent of Equation 2.13. For a 3D crystal, \mathbf{k} is 3D, as well. With the parameter space restricted to three dimensions, a very useful definition is the Berry curvature:

$$F_{ij} = \langle \nabla_i n(\mathbf{k}) | \nabla_j n(\mathbf{k}) \rangle - \langle \nabla_j n(\mathbf{k}) | \nabla_i n(\mathbf{k}) \rangle. \quad (2.24)$$

Finally, we are ready to examine a topological phase. The first system we will look at is the quantum Hall effect. The quantum Hall effect was first observed by Klaus von Klitzing in 1980 [18]. The classical Hall effect had been observed over a century earlier by Edwin Hall in 1879 [12], this was an experiment on a thin, conducting bar with an applied voltage along its x-axis, shown in Figure 2.6. This generates a current through the bar. An out-of-plane magnetic field is then applied which applies a Lorentz force on the charge carriers in the bar, $\mathbf{F} = q(\mathbf{E} + \mathbf{v} \times \mathbf{B})$. This diverts the charge carriers to the sides of the bar along the y-axis which creates another voltage:

$$V_H = \frac{I_x B_z}{nte} \quad (2.25)$$

V_H is the Hall voltage, I_x is the current in the x-direction, B_z is the out of plane magnetic field, n is the charge carrier density, t is the thickness of the bar, and e is the charge of an electron. A resistance can be defined along the y-direction. This is the Hall resistance, and it's easy to show that:

$$R_H = \frac{1}{ne} \quad (2.26)$$

In this classical Hall effect, the Hall resistance can take on any value. This is not the case in the quantum Hall effect.

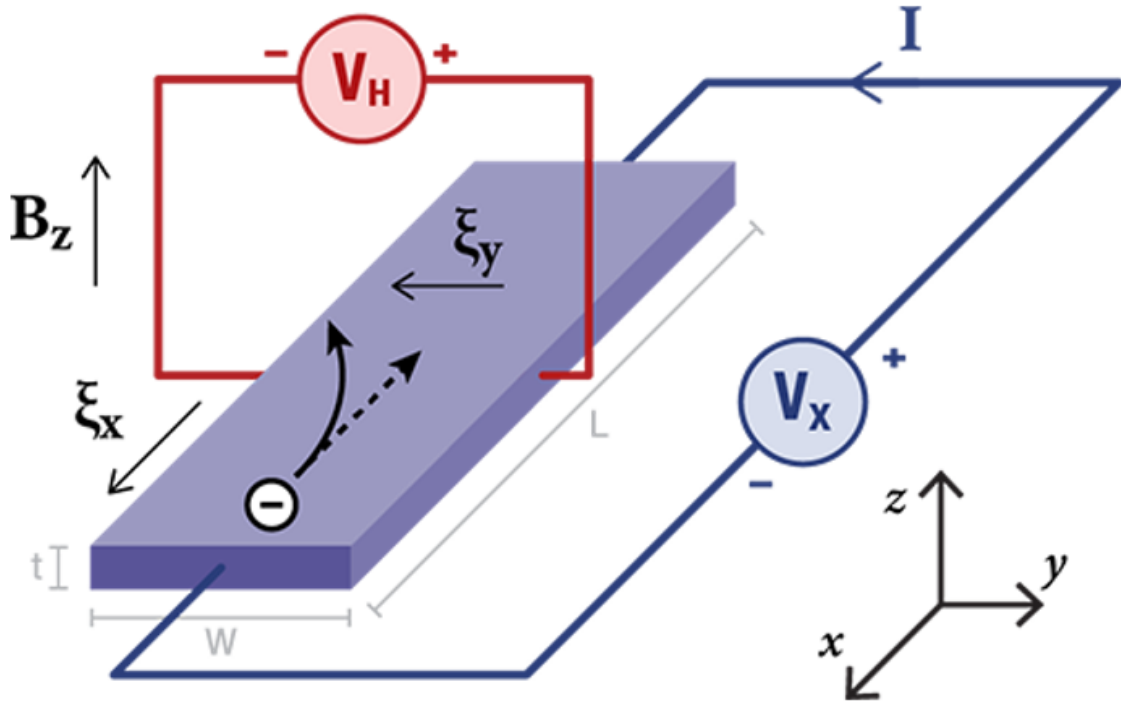


Figure 2.6 A diagram of the classical Hall effect experiment. The thin conducting slab, often referred to as a Hall bar, has a voltage applied along the x-axis. An external magnetic field is applied in the z-axis, creating a Hall voltage, V_H to develop along the y-axis. The geometry shown here is for negative charge carriers. Positive charge carriers would be deflected in the opposite direction. Adapted from TBD.

In the quantum hall effect, the Hall resistance can take on only quantized values:

$$R_{xy} = \frac{h}{e^2\nu} \quad (2.27)$$

ν is called the filling factor, and it only takes on integer values (the fraction quantum Hall effect is outside of the scope of this dissertation.) The key to von Klitzing's experiment was the use of a 2D electron gas (2DEG) at low temperature (1.5 K) with a strong magnetic field (up to 18 T.) Electrons in the 2DEG undergo cyclotron motion and form highly degenerate Landau levels, as shown in Figures 2.7 and 2.8. The quantum numbers determining the location of the cyclotron orbit do not affect the energy, so we can think of the number of allowed electrons per Landau level as the being equivalent to the number of cyclotron orbits that can fit in the area, A , of the 2DEG:

$$N_B = \frac{AeB}{2\pi\hbar} \quad (2.28)$$

Which can then be used to calculate the number of filled Landau levels or the filling factor:

$$\nu = \frac{hn_{2D}}{eB} \quad (2.29)$$

So far, we have described the quantum Hall effect without any topological arguments. Indeed, historically the quantum Hall effect was understood without such arguments until Thouless' landmark paper in 1994 [35]. What role, then, does topology play in understanding the quantum Hall effect? Part of what makes the quantum Hall effect such a remarkable experiment is the level of precision in the measurement. The Hall conductance, $\sigma_{xy} = \nu \frac{e^2}{h}$ takes on integer values of the conductance quantum, $\frac{e^2}{h}$. Klitzing used this measurement to independently calculate the fine-structure constant to seven significant figures. Such precision is very unusual in condensed matter systems where imperfections in device quality will typically add significant uncertainty to the measurements.

Topological phases are characterized by a topological invariant: a quantity which does not change due to smooth deformations so long as the energy gap remains open. These phases are said to be "topologically protected" because they are immune to local perturbations and defects. The topological invariant can be calculated for any insulator, including the vacuum. If the value of the topological invariant is equal to that of the vacuum, the insulator is said to be topologically trivial. For the quantum Hall effect, the topological invariant is the Chern number:

$$n = \frac{1}{2\pi} \int d^2\mathbf{k} \cdot \mathbf{F} \quad (2.30)$$

Which is calculated by integrating over the Berry curvature over the Brillouin zone. This topological invariant can take on integer values with $n = 0$ being the topologically trivial phase. The Hall conductance is $\sigma_{xy} = \frac{e^2}{h}n$. We see, then, that there is a one-to-one correspondence between the Chern number and the filling factor, ν . This explains why the measurement of the quantized Hall conductance is not sensitive to device defects.

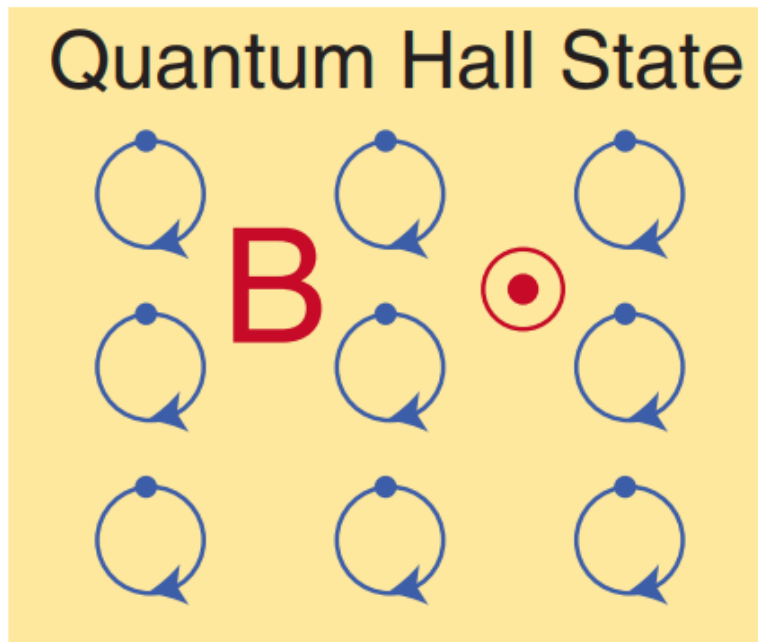


Figure 2.7 A cartoon of electron cyclotron orbits in a 2DEG with an applied out-of-plane magnetic field. Due to the exclusion principle, only two electrons can occupy the same space in the 2DEG. This means that the degeneracy of the Landau levels is dependent on the size of the orbits and therefore the magnetic field. Increasing the magnetic field creates smaller orbits, increasing the degeneracy of the Landau levels. Adapted from Ref [13].

Furthermore, it explains another aspect of the quantum Hall effect: the integer number of conducting chiral edge channels. This effect is a special case of a feature ubiquitous to topological phases, bulk-boundary correspondence. Consider a quantum Hall system with $n = 1$ like Figure 2.9. In the material, the value of the Chern number is 1, but the material has a boundary. Typically, on the other side of the boundary is a topologically trivial insulator, like the vacuum. I said earlier that the topological invariant cannot change under smooth deformations so long as the energy gap remains open. The laws of physics are smooth, so how is it possible to transition from the topological bulk of the material to the topologically trivial exterior? The answer is simple: the gap must close. States closing the gap and crossing the Fermi are conducting, so this bulk-boundary correspondence perfectly explains the existence of conducting edge channels.

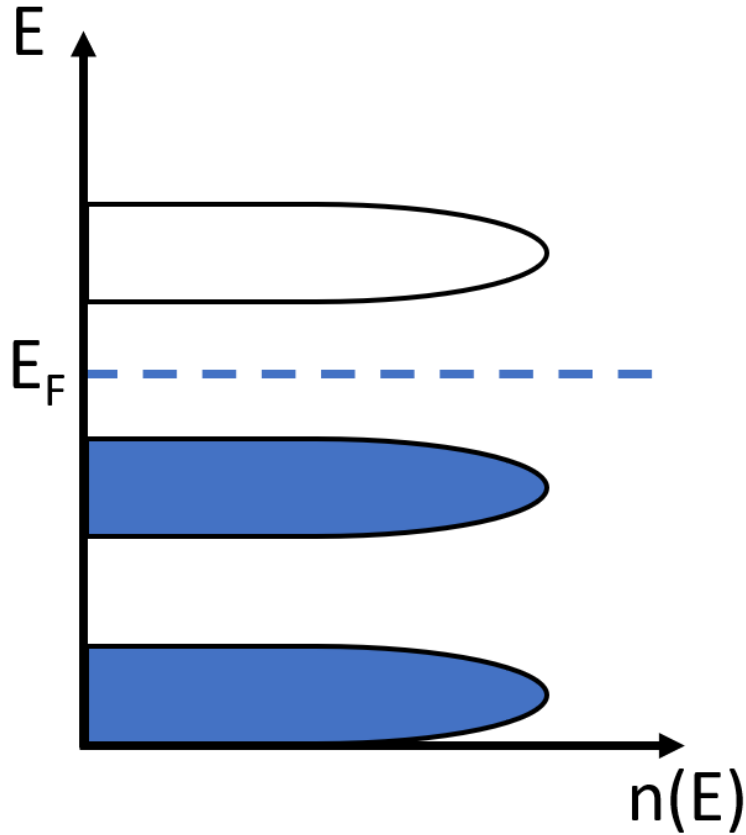


Figure 2.8 A diagram of the number of electrons at a given energy in a quantum Hall system. The degeneracy of the Landau levels is dependent on the strength of the magnetic field, so the filling factor, ν , changes with changing magnetic field. Pictured here is the situation with $\nu = 2$. If the magnetic field were to double in magnitude, then the number of electrons that can fit in a Landau level would increase by two-fold. This means that only the bottom Landau level would be occupied with $\nu = 1$.

2.3 Theory of Strong, 3D Topological Insulators

Since the discovery of the quantum Hall effect as an example of a topological phase, there has been tremendous theoretical and experimental development in the study of topological phases [13]. Topological phases can be categorized based on the dimensionality of the system and the symmetries of the Hamiltonian, as shown in Figure 2.10. There are three symmetries used to classify condensed matter systems: time-reversal symmetry Θ , particle-hole symmetry Ξ , and chiral symmetry $\Pi = \Xi\Theta$. To determine the class of equivalent Hamiltonians, it's necessary to consider which of these three symmetries it has, and the values of $\Theta^2 = \pm 1$ and $\Xi^2 = \pm 1$.

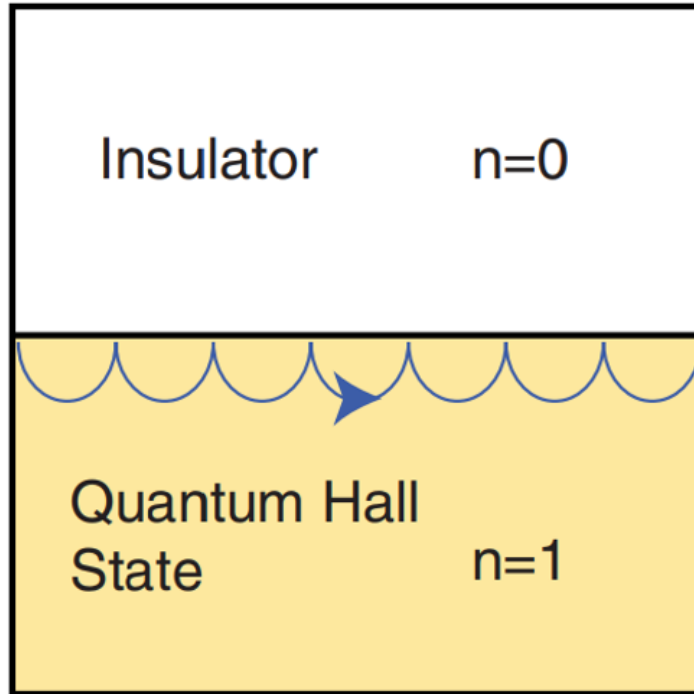


Figure 2.9 A diagram demonstrating bulk-boundary correspondence with a quantum Hall system with Chern number $n = 1$. With $n = 1$, a single conducting chiral edge channel forms at the boundary. The number of edge channels is equal to the Chern number. Adapted from [13].

The symmetry class, along with the dimensionality determines whether the system can support a topological phase and the allowed values of the topological invariant. For example, the quantum Hall effect violates all of the symmetries, so it falls into symmetry class A with $d = 2$. Looking at Figure 2.10, we can see that the topological invariant is a \mathbb{Z} topological invariant, meaning it can take on integer values.

In this Section, I will discuss two other topological phases: the quantum spin Hall effect (QSHE) and the strong, 3D topological insulator (3D TI). The 3D TI is the only system directly relevant to the experiments in this dissertation; however, it is possible to derive the existence of one topological phase from another. Note that in Figure 2.10 there is a structure to which symmetry classes and dimensionalities support a topological phase. The QSHE is from symmetry class AII ($\Theta^2 = -1$) with $d = 2$, and its topological nature can be deduced from by adding time-reversal symmetry to

AZ	Symmetry			d		
	Θ	Ξ	Π	1	2	3
A	0	0	0	0	(a) \mathbb{Z}	0
AIII	0	0	1	\mathbb{Z}	0	\mathbb{Z}
AI	1	0	0	0	0	0
BDI	1	1	1	\mathbb{Z}	0	0
D	0	1	0	(b) \mathbb{Z}_2	(c) \mathbb{Z}	0
DIII	-1	1	1	\mathbb{Z}_2	\mathbb{Z}_2	\mathbb{Z}
AII	-1	0	0	0	(d) \mathbb{Z}_2	(e) \mathbb{Z}_2
CII	-1	-1	1	\mathbb{Z}	0	\mathbb{Z}_2
C	0	-1	0	0	\mathbb{Z}	0
CI	1	-1	1	0	0	\mathbb{Z}

Figure 2.10 The periodic table of topological phases. Topological phases are classified by their symmetry class and dimensionality. The symmetries are time-reversal, Θ , particle-hole, Ξ , and chiral, $\Pi = \Xi\Theta$. If the system has a symmetry, it's indicated with ± 1 , where the sign is the value of the symmetry squared. A 0 indicates the system does not have that symmetry. Highlighted in blue are the topological phases discussed in this dissertation. (a) The quantum Hall effect, quantum anomalous Hall effect or Chern insulator. This phase is discussed in Section 2.2. (b) The Kitaev chain. This phase is discussed in Section 2.4. (c) The $p_x + ip_y$ superconductor. This phase is also discussed in Section 2.4. (d) The quantum spin Hall effect. Discussed in this section. (e) The strong, 3D topological insulator. Also discussed in this section. Adapted from Ref [13].

the chiral edge modes in a quantum Hall system (also known as a Chern insulator.) Furthermore, the topological invariant for 3D TIs can be deduced from extending the QSHE topological invariant to three dimensions.

We start by considering a Chern insulator with N chiral edge modes. When time-reversal symmetry is applied to this system, the number of edge modes doubles, as shown in Figure 2.11. Now there is an equal number of modes propagating in each direction. The effects of disorder are captured in a $2N \times 2N$ scattering matrix:

$$S = \begin{pmatrix} r & t \\ t' & r' \end{pmatrix} \quad (2.31)$$

Here r and t are block matrices corresponding to reflection and transmission, respectively. The prime indicates if the reflection/transmission is on states on the left or right side of the scattering region. These blocks have dimensions $N \times N$. If the edge states are susceptible to disorder, then it's possible to create the condition $t = t' = 0$ by adding more disorder. In the scattering process, the current is conserved, so r becomes unitary, $r^\dagger r = r'^\dagger r' = 1$. Time-reversal symmetry places further constraints on the scattering matrix:

$$S = \Theta^2 S^T \quad (2.32)$$

The edge states are electrons, spin 1/2 particles with $\Theta^2 = -1$. Equation 2.32 therefore implies that S is anti-symmetric ($S = -S^T$). If $t = 0$, then r must be simultaneously unitary and anti-symmetric. This is possible for even N , but it is impossible for odd N .

Anti-symmetric matrices with an odd number of dimensions must have an eigenvalue $\lambda = 0$ while unitary matrices have $|\lambda_i|^2 = 1$ for all λ_i . This contradiction implies that $t = 0$ is impossible for odd N , and the mode with $\lambda = 0$ in the reflection matrix is transmitted with unit probability. The protected mode is doubled by time-reversal symmetry giving us two counter-propagating edge states with opposite spin, known as helical edge states. There are two possible phases: the topologically trivial phase with even N and the topologically non-trivial phase with odd N . Such

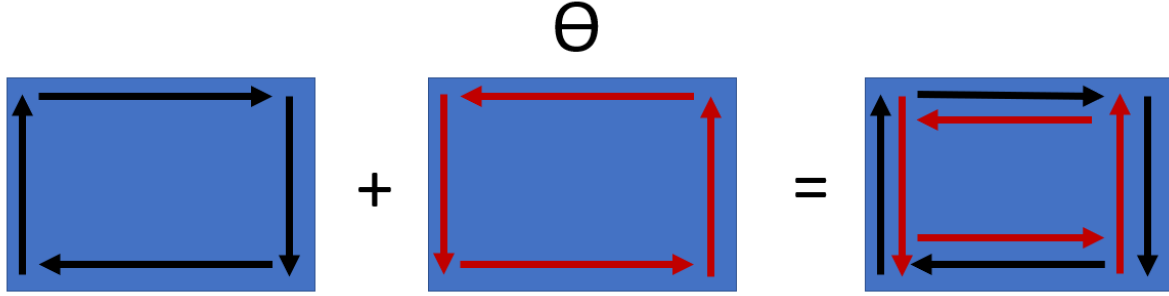


Figure 2.11 The helical edge states in the QSHE can be constructed from a Chern insulator with an odd number of chiral edge states and their time-reversed twin. Pictures here is the situation with $N = 1$ chiral edge states.

a situation implies that the topological invariant is of the \mathbb{Z}_2 type where it can take on only two values. Qualitative arguments looking at just the properties of states crossing the band gap of a system with $\Theta^2 = -1$, and therefore Kramers' degeneracy, reach the same conclusion, as shown in Figure 2.12.

Calculating the topological invariant in the general case from properties of the bulk is rather involved [16]. Adding the condition that spin in the z -direction S_z is conserved makes the calculation much simpler. The Chern numbers for spin-up and spin-down electrons become separable. These Chern number can be combined into a single quantity, $n_\sigma = (n_\uparrow - n_\downarrow)/2$, that can then be used to calculate the \mathbb{Z}_2 topological invariant:

$$\nu = n_\sigma \pmod{2} \quad (2.33)$$

Here $\nu = 0$ is the topologically trivial phase, and $\nu = 1$ is the topologically non-trivial phase. This result is consistent with the analysis of the scattering matrix. In the case where we start with a Chern insulator with a single edge mode ($N = 1$), then $n_\uparrow = 1$, and $n_\downarrow = -1$ giving us $n_\sigma = 1$ and $\nu = 1$.

When we go from 2D to 3D, the topological insulator can be characterized with four topological invariants, $(\nu_0; \nu_1\nu_2\nu_3)$. Each of these topological invariants are of the \mathbb{Z}_2 type. The first invariant,

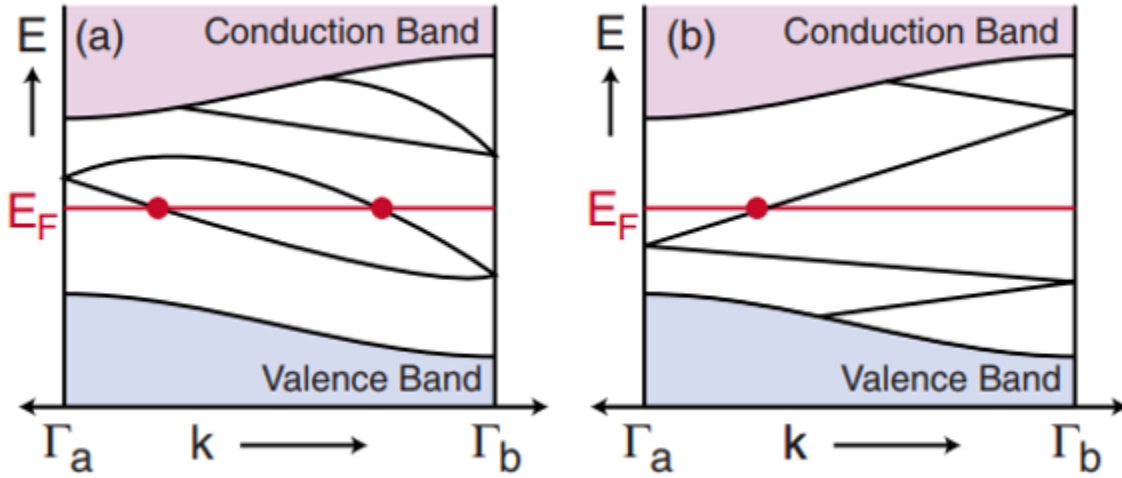


Figure 2.12 An example of the two possible ways states can cross the Fermi level with Kramer degeneracy and time-reversal symmetry. At the Kramer degenerate points Γ_a and Γ_b , the Kramer pairs need to rejoin. (a) The Kramer pairs rejoin in a loop with an even number of Fermi level crossings. These conducting states are not topologically protected. Perturbations could push the loop away from the Fermi level. (b) The Kramer pairs form a connected chain from the valence band to the conduction band with an odd number of Fermi level crossings. These conducting states are topologically protected. Adapted from [13].

ν_0 is the "strong" topological invariant protected by time-reversal symmetry. The other invariants are considered "weak" because they are not protected by time-reversal symmetry and can be localized with disorder. To understand the origin of these four \mathbb{Z} , we need to look at the 3D Brillouin zone. Time-reversal symmetry creates the condition:

$$\Theta \mathcal{H}(\mathbf{k}) \Theta^{-1} = \mathcal{H}(-\mathbf{k}) \quad (2.34)$$

This means that a plot of energy as a function of \mathbf{k} has reflection symmetry from \mathbf{k} to $-\mathbf{k}$, and the Brillouin zone is fully defined from $k_i \in \{0, \pi\}$. The Brillouin zone is a cube with six surfaces at $k_{x,y,z} = 0$ or π , as shown in Figure 2.13. It's possible to calculate a QSHE \mathbb{Z}_2 invariant for each of these six surfaces; however, there is a constraint $\nu_x(0)\nu_x(\pi) = \nu_y(0)\nu_y(\pi) = \nu_z(0)\nu_z(\pi)$. Any one of these products is the strong invariant $\nu_0 = \nu_i(0)\nu_i(\pi)$. The weak invariants are then defined on the three surfaces, $\nu_{1,2,3} = \nu_{x,y,z}(\pi)$.

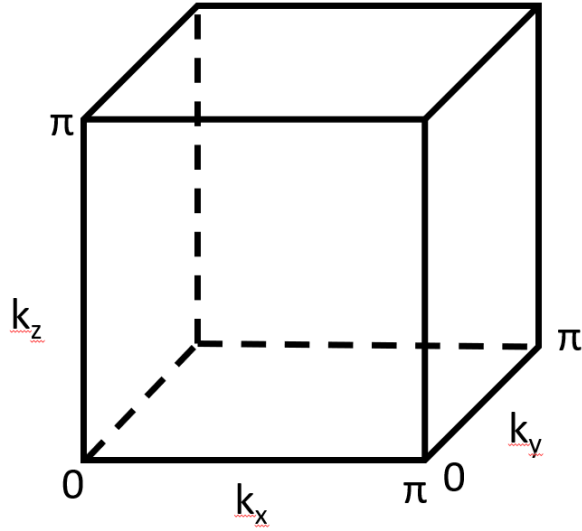


Figure 2.13 The Brillouin zone in 3D with time-reversal symmetry. This cube has six faces on which a \mathbb{Z}_2 topological invariant can be defined. The strong topological invariant is only non-trivial if the \mathbb{Z}_2 topological invariants on opposite faces of the cube are different.

Bulk-boundary correspondence in the 3D TI manifests as a 2D time-reversal symmetric conducting surface state. While the bulk of the TI is insulating, the surface of the material is conducting. This conducting surface state has a linear dispersion relation, referred to a Dirac cone which comes down to a Kramers degenerate Dirac point. A 3D TI in general has an odd number of Dirac cones and Dirac points, but the simplest case (the case studied in the rest of this dissertation) has a single Dirac cone described by:

$$\mathcal{H}_{surface} = -i\hbar v_F \vec{\sigma} \cdot \vec{\nabla} \quad (2.35)$$

Where v_F is the Fermi velocity and $\vec{\sigma}$ are Pauli matrices. Time-reversal symmetry also means that the Dirac cone states with opposite spin have opposite momentum, as well. This is shown in Figure 2.14.

2.4 Theory of Topological Superconductivity

Majorana fermions were first proposed by Ettore Majorana in 1937 as solutions to the Dirac equation [25]. These fermions had the unique property of being their own antiparticle. Majorana fermions have not been observed to exist in nature as fundamental particles; however, they may

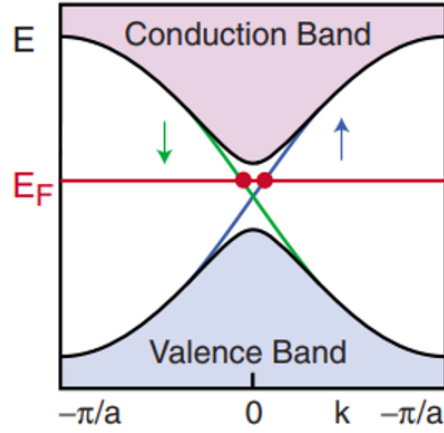


Figure 2.14 The Dirac cone formed at the boundary of a TI. States with opposite spins from the valence and conduction bands cross the Fermi level with a linear dispersion relation. Adapted from Ref [13].

exist as quasiparticles on the boundaries of topological superconductors. These quasiparticles are distinct from the Majorana fermions theorized in three main ways: they are typically bound states, not free particles, they are at zero energy (due to the typical bulk-boundary correspondence arguments), and they are spinless and therefore not fermions. For these reasons, these quasiparticles are typically referred to as Majorana bound states (MBS) or Majorana zero modes (MZM) in the literature. Nonetheless, they obey the fundamental Majorana relation, $\gamma = \gamma^\dagger$, showing that they are created and annihilated with the same operator, and they have other interesting properties that are impossible in 3+1 dimensions.

The second quantization fermion creation and annihilation operators can be written as a pair of Majorana operators, γ_1 and γ_2 :

$$c^\dagger = \frac{1}{2}(\gamma_1 + i\gamma_2), \quad c = \frac{1}{2}(\gamma_1 - i\gamma_2) \quad (2.36)$$

Rearrange the equation, and we see that the MZMs are an equal-weight superposition of electrons and holes:

$$\gamma_1 = c + c^\dagger, \quad \gamma_2 = i(c - c^\dagger) \quad (2.37)$$

It's easy to verify that $\gamma = \gamma^\dagger$. From the anti-commutation relation for fermionic creation and annihilation operators, $[c_n^\dagger, c_m]_+ = \delta_{nm}$, it's similarly simple to derive $[\gamma_i, \gamma_j]_+ = 2\delta_{ij}$ and $\gamma^2 = 1$. Up to this point these operators are simply a mathematical trick. The only way to observe the properties of the MZMs is to isolate individual Majorana quasiparticles. This seems impossible given that condensed matter systems are comprised of electrons, Dirac fermions with pairs of Majoranas.

The key idea to physically realize MZMs came from Alexei Kitaev [17]. His idea, known now as the Kitaev chain, was that in a 1D chain of fermions, a Hamiltonian with coupling between neighboring Majorana operators can be created. A topologically trivial 1D chain of N fermions has $2N$ Majorana operators paired with each other like so:

$$H = (i/2)\mu \sum_{n=1}^N \gamma_{2n-1}\gamma_{2n} \quad (2.38)$$

With chemical potential μ . This is shown in Figure 2.15. If the Majorana modes on adjacent sites pair up, the topologically non-trivial result is:

$$H = it \sum_{n=1}^{N-1} \gamma_{2n+1}\gamma_{2n} \quad (2.39)$$

There are two unpaired Majorana modes at the opposite ends of the chain that do not appear in the Hamiltonian. These modes would therefore have zero energy while the modes in the bulk of the chain have energy t . To understand what physical system might support such pairing, substitute Equation 2.37 into Equations 2.39 and 2.38. The result is the tight-binding Hamiltonian:

$$H = -\mu \sum_n c_n^\dagger c_n - t \sum_n (c_{n+1}^\dagger c_n + h.c.) + \Delta \sum_n (c_n c_{n+1} + h.c.) \quad (2.40)$$

With onsite potential μ , hopping amplitude t , and p-wave superconducting pairing Δ . Equation 2.39 is recovered for $\Delta = t$ and $\mu = 0$, while Equation 2.38 is recovered for $\Delta = t = 0$ and $\mu \neq 0$. Fine-tuning to a single point in parameter space is impossible in practice. Kitaev showed that the chain is in the topological phase so long as $\mu < |2t|$. Before we can calculate the topological invariant we need the Bogoliubov-de Gennes (BDG) Hamiltonian in momentum space:

$$H(k) \equiv \langle k | H_{BDG} | k \rangle = (-2t \cos k - \mu)\tau_z + 2\Delta \sin k \tau_y \quad (2.41)$$

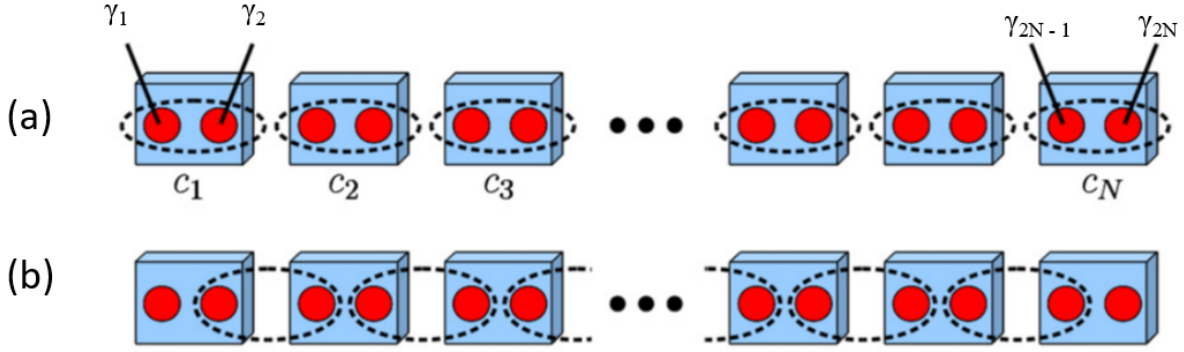


Figure 2.15 The two ways that Majorana modes can be paired in a 1D chain. (a) Topologically trivial pairing of Majorana modes within fermion modes. (b) Topologically non-trivial pairing of Majorana modes between fermion modes. This leaves two unpaired Majorana modes at the ends of the chain. Adapted from [31].

Here τ_i are Pauli matrices for the particle-hole degree of freedom. The \mathbb{Z}_2 topological invariant, Q , is calculated from the sign of the Pfaffian of the Hamiltonian at $H(k=0)$ and $H(k=\pi)$:

$$(-1)^Q = \text{sign}(\text{Pf}[iH(0)]\text{Pf}[iH(\pi)]) \quad (2.42)$$

If the right hand side is negative, then $Q = 1$, and the Hamiltonian is topologically non-trivial. Otherwise, $Q = 0$, and the Hamiltonian is trivial.

Just as we upgraded the QSHE in 2.3 from 2D to 3D, we can take the Kitaev chain from 1D to 2D. By coupling a stack of Kitaev chain, we can get the 2D Hamiltonian:

$$H(k_x, k_y) = -[2t(\cos k_x + \cos k_y) + \mu]\tau_z + \Delta(\sin k_x \tau_y - \sin k_y \tau_x) \quad (2.43)$$

There was some sleight of hand here where the coupling strength between the chains was fine-tuned so that the Hamiltonian would come out in a cleaner form. Not to worry, as this tuning is not enough to close the gap and change the topological invariant. We are interested in zero-energy states at zero-momentum, so let's expand this Hamiltonian about $\mathbf{k} = \mathbf{0}$:

$$H(k_x, k_y) \approx [t(k_x^2 + k_y^2) - \mu + 4t]\tau_z + [i\Delta(k_x + ik_y)\tau_+ + \text{h.c.}] \quad (2.44)$$

Here $\tau_+ = (\tau_x + i\tau_y)/2$. The superconducting pairing is p-type and proportional to $k_x + ik_y$. This suggests that topological superconductors in 2D are $p_x + ip_y$ superconductors. It was Krauss et al who showed theoretically that MZMs form in vortices of these superconductors [20].

It's unlikely that topological superconductors and MZMs would have garnered so much attention if there wasn't an exciting application for them. Quantum computing is a topic of great interest (and funding) at the moment. Quantum computers process information in the form of two-level quantum systems, called qubits. To run the computation, it's necessary to affect the qubit states with unitary transformations. Unfortunately, quantum systems are notoriously fragile and prone to decoherence, creating errors in the computation. MZMs offer a solution to this problem in the form of topological protection and non-Abelian exchange statistics.

The two-level system for the MZMs is the presence $|1\rangle$ or absence $|0\rangle$ of a fermion. The unitary transformation that exchanges the positions of two MZMs is:

$$U = \exp\left\{\pm\frac{\pi}{4}\gamma_n\gamma_m\right\} = \frac{1}{\sqrt{2}}(1 \pm \gamma_n\gamma_m) \quad (2.45)$$

In a basis with four Majoranas, there are four possible qubit states: $|00\rangle$, $|01\rangle$, $|10\rangle$, and $|11\rangle$. Exchanging the first two Majoranas with U_{12} only adds a phase because these are MZMs belonging to the same fermion. However, exchanging the middle two Majoranas with U_{23} changes the fermion occupations. For example:

$$U_{23}|00\rangle = \frac{1}{\sqrt{2}}(|00\rangle - i|11\rangle) \quad (2.46)$$

This is shown schematically in Figure 2.16. Successive exchanges, also called braids, of MZMs will navigate the qubit Hilbert space, enabling quantum computation. These states will be topologically protected from local perturbations so long as the perturbation is not strong enough to unwind a braid or close the gap. This approach to quantum computing is called topological quantum computing. There is great experimental interest in producing, measuring, and manipulating MZMs.

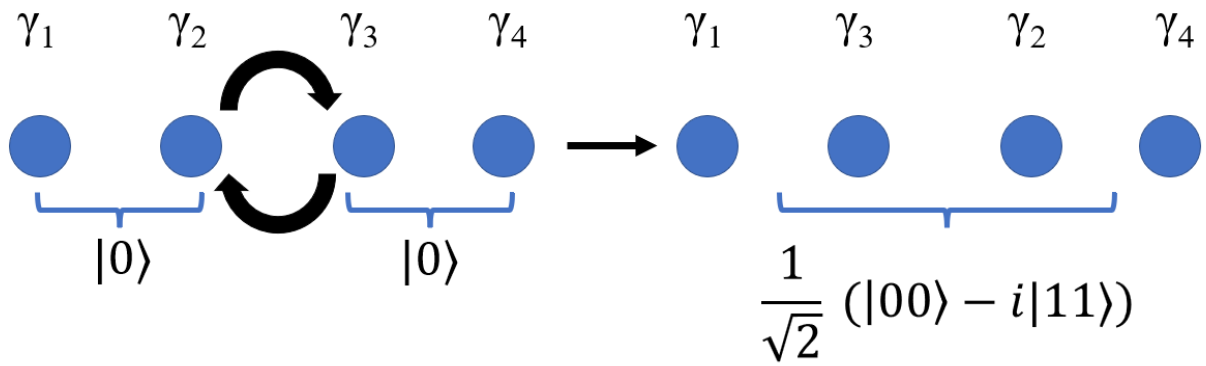


Figure 2.16 A cartoon of the Majorana braiding operation described by Equation 2.46. Before the braid, the qubit is in the state $|00\rangle$. After the braid, the qubit is in state $\frac{1}{\sqrt{2}}(|00\rangle - i|11\rangle)$.

CHAPTER 3

SCANNING TUNNELING MICROSCOPY METHODOLOGY

This chapter details the specifics of how scanning tunneling microscopy (STM) measurements are conducted in the experiments detailed in following chapters. This begins with diagrams and explanations of the microscope design, including the beetle-style sample positioning system. Details are also provided on the cryostat design and the functions of the electronics control box, along with basic procedures. All of these details are relevant to the experimental designs in this thesis. For example, the beetle-style sample mounting system, originally designed by Besocke [3], is the primary reason samples are designed to be uniform on millimeter length scales. Otherwise, finding the area of interest creates a blind needle-in-a-haystack problem. This chapter concludes with detailed procedures on how tips are prepared and tested.

3.1 Microscope Design and Procedures

The primary cryogenic research STMs were constructed by the first graduate students in the Tessmer group, based on the Besocke design [3]. Sergei Urazhdin and Stuart Tessmer drafted the specific details of each part, most of which were machined by the Department of Physics and Astronomy Machine Shop. Other graduate students have since iterated on these microscopes, but the core design remains unchanged.

These microscopes utilize the inertial or "stick slip" motion of piezo tubes to rotate the sample into range of the tip or move the sample laterally for coarse positioning. This motion is commonly referred to as "walking." The tip sits on a piezo tube of its own that controls the feedback of the tip and the scan area. Piezo electric materials are materials that expand and contract linearly and precisely in response to applied voltages. In our set-up, one can apply a maximum of ± 130 V to the tip piezo with calibrations values as follows at room temperature: $X = 29.31$ nm/V, $Y = 36.22$ nm/V, $Z = 2.704$ nm/V (as measured by my predecessor M. Gasseller). By convention, the $\pm X$

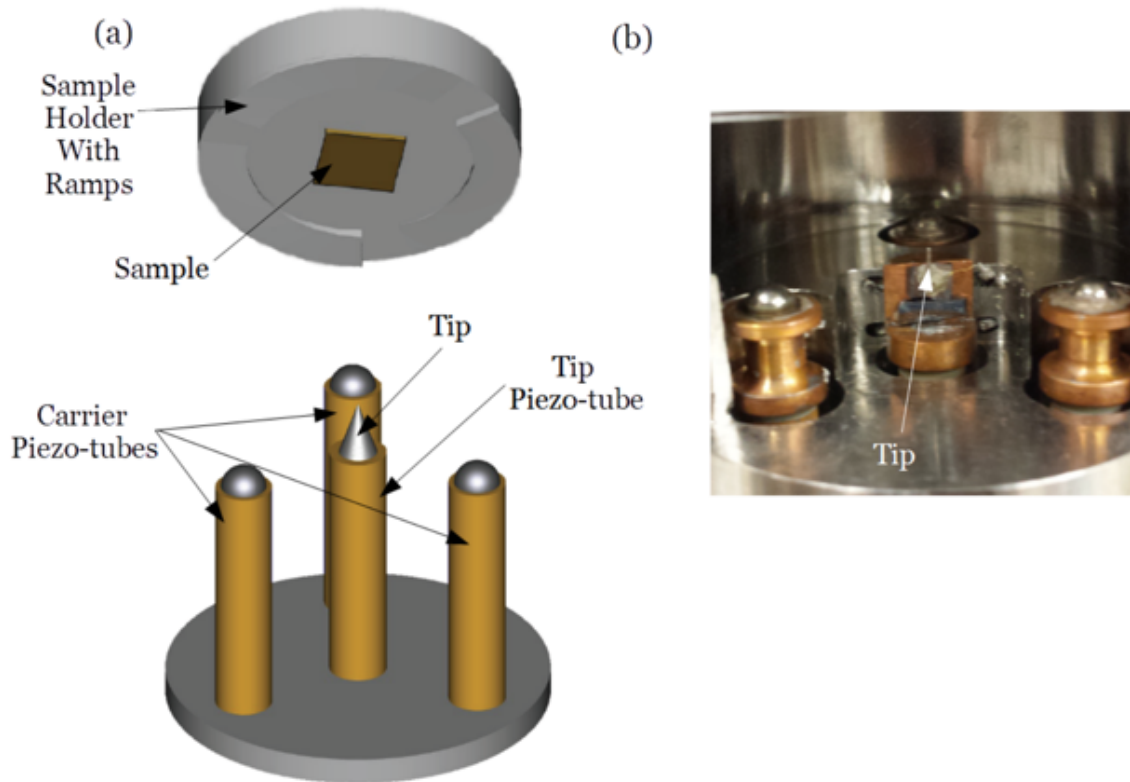


Figure 3.1 (a) A diagram of the sample holder with three ramps. These ramps rest on the carrier piezo-tubes. Applying a voltage to the carrier piezo-tubes causes them to oscillate back and forth, using the inertia of the sample holder to bring the sample closer to the tip step by step. (b) A tip fully installed into the microscope. Vacuum grease keeps the tip attach to its piezo-tube. A gold wire is soldered to the tunneling current lead, creating a conducting path from the tip to the control box.

directions refer to moving the sample left (-) and right (+), and the $\pm Y$ directions refer to moving the sample out of (-) and into (+) the opening where the sample disc is loaded into the microscope. The $\pm Z$ directions correspond to moving the sample closer (-) and further from the tip (+). What this means practically, is that there is a trade-off in how much voltage is allocated to the scan area size and how much voltage is allocated to feedback. If the scan area too large, the tip will not be able to retract when it encounters features too tall for the feedback range.

A big advantage of this style of scanning probe microscope is that the sample can be moved up to 1 mm laterally, so the tip can conceivably explore over a wide range. This design can create

an issue, however, that is referred to simply as the "needle in a haystack" problem. Some samples and devices may only have a small area that is interesting for the experiment. Because the tip can land anywhere within a 1 mm diameter circle, it's possible that the tip doesn't find these regions of interest.

There are some key techniques to deal with the "needle in a haystack" problem. The most effective solution is simply to study samples and devices that are uniform over millimeter length scales. For example, the gas exposure experiments detailed in chapters 4 & 5 were conducted on the surface of Bi_2Se_3 crystals with lateral dimensions on the order of several millimeters. The Josephson junction experiments detailed in chapters 6 & 7 were conducted on devices that are 1x1 mm sized arrays on 5x5 mm sized substrates. To aid with aligning the area of interest with the tip, the sample is sometimes adhered to the sample disc with vacuum grease with a gold wire and silver paint creating a conducting path from the sample surface to the sample disc. Vacuum grease is sticky and pliable at room temperatures, but it solidifies at low temperatures. It is therefore possible to move the sample laterally over the sample disc and center the area of interest over the tip. Ideally, the area of interest can be reached by walking the sample to the end of its range in one of the four cardinal directions: $\pm X$ and $\pm Y$. That way, at low temperature, the area can be found by walking for several minutes in that direction and then walking into range.

The microscope is controlled by the RHK R9 control box. This box controls all of the important functions of the STM: piezo voltages, bias voltage, current measurement, feedback control. There are two types of procedures it can run to move the sample: Fast and Feedback Detect. The Fast walking pattern moves the sample while keeping the feedback on the tip unlimited. Then, if the sample comes in range of the tip, the feedback needs to react to prevent the tip from crashing into the sample. This is very likely to damage the tip. This walking method is only used for lateral sample moves for this reason.

Feedback Detect performs a discrete number of walking steps with the tip feedback fully retracted. Then, it will unlimit the feedback, causing the tip to push forward until it detects tunneling current. If it fails to find tunneling current, it will retract again and move the sample several more times. This walking method is much safer; however, it's also much slower. That's not an issue at room temperature when the piezo tubes are able to move their maximum amplitudes. However, at lower temperatures this walking method may fail to move the sample at all, unless the walking parameters have been finely tuned. We can test the walking method at room temperature by limiting the maximum voltage the amplifiers will put on the walking piezotubes. To test how the microscope would move at liquid helium temperatures, for example we would divide the 150 V by 5.5 to get 27 V. If the sample is unable to move with this restriction, then we can change the number of steps taken between feedback cycles. If the number of steps is too low, the sample won't move at all. If the number is too high, the sample will crash into the tip when it comes in range. I have found that 10 cycles is a good middle-ground for liquid helium experiments.

3.2 Cryostat Design and Procedures

There are two cryostats in the Tessmer lab: one in the main lab area and another in a small, acoustically shielded room, B131A. The research presented in this thesis was taken on the B131A system. This cryostat was produced by Oxford Instruments. The main components, detailed in Figure 3.2, are: the main bath, the 1K pot, the outer vacuum chamber (OVC), the inner vacuum chamber (IVC), and the sample space.

The vacuum spaces should be pumped in the following order: OVC, IVC, then sample space. The OVC is lined with Mylar sheets that reflects photons that would otherwise radiate heat away from the cryostat. These sheets are fragile, so the vacuum pump line must be pumped to $< 10^{-4}$ torr before opening the OVC valve. This valve must be opened slowly to restrict the flow rate of gas particles leaving the chamber. Ideal base pressures for the OVC are $< 5 \times 10^{-6}$ torr, achieved typically in 24 hours. The IVC is a very small space that is pumped to suitable ($< 5 \times 10^{-6}$ torr) pressures in less than two hours. After it has been pumped out, the IVC is typically back-filled

with helium exchange gas to improve thermal contact between the main bath and the sample space. This is accomplished by purging a rubber gas line with ultra-high purity helium gas and pinching it off 5cm from the IVC. The IVC valve is then opened and closed, allowing the pinched-off volume of helium gas into the chamber. Finally, the sample space is prepared by connecting the vacuum pump line to the top of the cryostat and opening the gate valve. It typically takes multiple days to reach a suitable base pressure $< 5 \times 10^{-6}$ torr.

Cryogenic liquids are transferred into the main bath to cool the cryostat and the microscope in order to achieve greater energy resolution in tunneling spectroscopy experiments. Liquid nitrogen and liquid helium are the two primary cryogenic liquids used in this cryostat. The boiling point of liquid nitrogen is 77 K. It's much warmer and cheaper than liquid helium, so the primary purpose of using liquid nitrogen is to pre-cool the cryostat to use liquid helium more efficiently. Because the cost of liquid nitrogen is so low, there are no efforts to recover the gaseous nitrogen that evaporates out of the cryostat.

Transferring liquid nitrogen is a simple process of connecting the "liquid" line of the transfer Dewar to the input line of the main bath, slightly opening the valve on the transfer Dewar, and allowing the residual pressure in the transfer Dewar force in the liquid nitrogen into the main bath. Care is taken to attach a hose to the exhaust of the main bath to vent the gaseous nitrogen out of the confined space of B131A and mitigate the risk of asphyxiation. The liquid nitrogen has to be pumped back out of the main bath before liquid helium can be transferred. To accomplish this, a source of nitrogen gas, typically from the free supply coming from the wall, is connected to the exhaust of the main bath. A thin metal tube has to mate with the fitting on the input line of the main bath. There is a distinct feeling when the tube is securely connected. It's crucial that there is a good connection. Otherwise, the liquid nitrogen will not be able to leave the main bath.

Once all of the liquid nitrogen is out of the cryostat, liquid helium can be transferred. Transferring liquid helium is a slightly more involved process. To begin with, the transfer line for liquid helium

is double-walled lined with vacuum. It's recommended to vacuum pump out the transfer line if it hasn't been pumped in the last 6 months. One end of the transfer line is slowly lowered into the transfer Dewar until a cold jet of gas blows out of the other end. This side of the transfer line then needs to be quickly secured to the input line to the main bath. The residual pressure in the transfer Dewar is sufficient to begin the transfer. Helium gas from a cylinder can be used to overpressure the transfer Dewar and move the liquid helium more quickly as the residual pressure dissipates. Throughout this process, the exhaust of the main bath is connected to the quick-connections that leads to the liquid helium recycle system in the sub-basement. There is a gas flow meter attached to this line that is used to monitor how quickly the transfer is progressing. It's critical that the transfer does not happen too quickly to avoid overloading the recycle system and therefore waste helium gas. Also, slower transfers will generally be more efficient, so long as losses in the transfer line do not begin to dominate. Acceptable measured flow rates should be between 0.1 and 0.5 ft³/s.

To improve thermal contact with the main bath, it is sometimes desirable to put exchange gas in the sample space. This must be done without the microscope in place, as the thermal shock would likely break the piezo tubes. Due to the sorption pump attached to the main bath, it is recommended that this be done after the main bath has been cooled. Otherwise, the sorption pump will absorb all of the exchange gas as it cools down. To keep the sorption pump and sample space clean, it's necessary to thoroughly purge the top of the sample space (above the gate valve) before opening the gate valve. Once this space is sufficiently purged, it is closed off from the helium line and the gate valve is opened, flushing the ultra-high purity helium gas in the volume into the sample space. This is done several times while watching the pressure in the sample space. Once a steady pressure of 100 mbar is in the sample space, the procedure is completed.

The microscope and sample can be loaded into the cryostat after it has been prepared with cryogenics and pumped to base pressure. It is sometimes expedient to load the microscope and sample into the cryostat before cooling, but performing the procedure in that order precludes the possibility of adding exchange gas to the sample space. The microscope is attached via vacuum

flange to the top of the sample space. Samples can be prepared in a glove box attached to the cryostat. The glove box is purged with inert gas to preserve the sample surface. Calculating the concentration of air remaining in the glove box follows a simple relationship, assuming perfect mixing:

$$n(t) = e^{-\frac{Q}{V}t} \quad (3.1)$$

Here $n(t)$ is the concentration of air in the vessel being purged, Q is the volumetric flow rate of the purging gas, V is the volume of the vessel being purged, and t is the time since the purging began. By measuring the flow rate of the gas and the volume of the chamber, it's possible to know how long to purge the glove box to achieve an air concentration of 0.00001 (the gas used to purge is ultra-high purity, meaning it is 99.999% pure, so a concentration of 0.00001 is the best that is achievable.) After the glove box has been purged, the sample can be cleaved with tape, exposing a clean surface, if it is a layered material. This sample can then be transferred to the microscope via the loading arm. The top of the cryostat is then sealed off from the glove box and vacuum pumped to base pressure. Finally, the gate valve can be opened, and the microscope can be lowered into the microscope. Quick changes in temperature ($>2\text{K}/\text{min}$) can damage the piezotubes, so the microscope is very slowly lowered into the cryostat while estimating the temperature with an Allen Bradley resistor.

3.3 Tip Fabrication and Testing

Tip quality is crucially important for STM experiments. There are two main methods for producing sharp metal tips: chemical etching and mechanical cutting. For the experiments presented in this thesis, the tips were produced by mechanical cutting. In principle, this is a very simple method. A Pt/Ir tip is cut with wire-cutters on a bias. The idea is that there should be one atom at the end of the tip that is closer than the others. In practice, if the tip is dull there can be distortions in the topography and spectroscopy. The presence of multiple atoms that may create sources of tunneling current into the surface can duplicate topographical features. A dull tip can also simply effectively average over the topographical features in a wide area, effectively limiting the resolution

of the topographic image. Spectroscopy can be distorted by a dull tip having an energetically small tunneling barrier. This tunneling barrier becomes non-linear as a bias voltage is applied between the tip and the sample. This effectively adds a symmetric "U" shaped contribution to the tunneling conductance centered around zero bias. Also, in materials with low carrier density, the presence of the tip can deplete the local charge carriers, which also would have the effect of symmeterizing the observed spectroscopy.

Producing a sharp tip via mechanical cutting is often an inconsistent procedure because it involves cutting a tip by hand. Any unsteadiness in the wire-cutters can cause them to brush against the tip, blunting it. This possibility is diminished by clamping the tip wire into a vice. The wire-cutters can rest against the edge of the vise. Carefully choosing the position of the wire in the vise allows a consistent, steep bias to be cut, as shown in Figure 3.3. By pivoting the cutters on the edge of the vice such that the cutter head moves up and away from the cut wire, it's less likely that unsteadiness will cause the cutters to blunt the tip, also shown in Figure 3.3. After the tip has been cut, it's cleaned with isopropyl alcohol and blown dry with N₂ gas. The tip is then affixed to a small silicon wafer fragment with silver paint. A gold wire is also affixed with the same silver paint. The completed tip is placed on the feedback piezotubes with vacuum grease. Like the procedure described in Section 3.1 for sample mounting, the vacuum grease is viscous at room temperature, but it solidifies at cryogenic temperatures, creating a rigid platform for the tip. The gold wire is soldered onto the tunneling current lead, creating the conducting pathway for the tunneling current.

Though this procedure consistently creates viable STM tips, it's still important to test the tips at room temperature to ensure their quality before proceeding with low-temperature experiments. Tips are tested with three primary methods: topography, spectroscopy, and tunnel barrier measurements. The first method, topography, is the most commonly employed due to its relative safety for the tip. Tips are typically tested on freshly-cleaved graphite samples. Graphite is chosen due to how cleanly it cleaves, leaving behind a flat surface. Because the feedback is on during topography and the

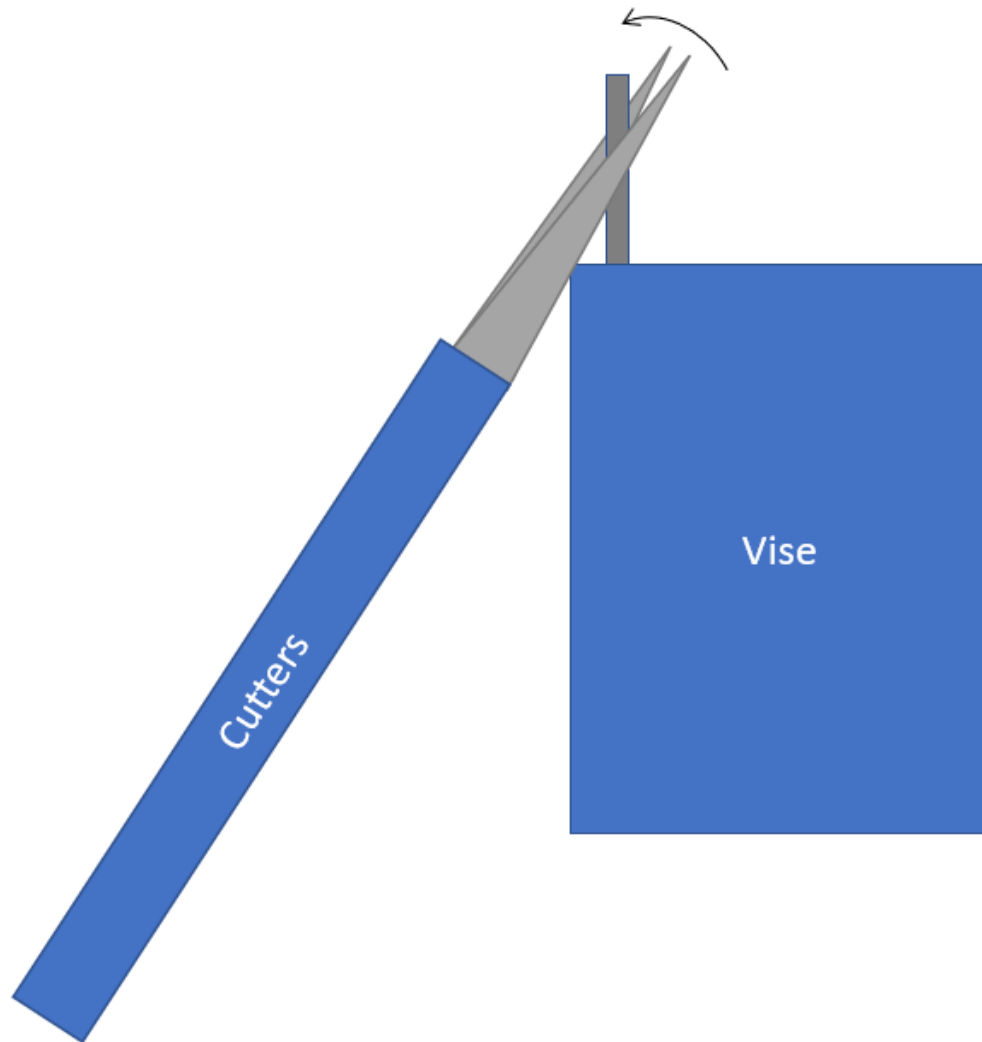


Figure 3.3 A diagram demonstrating the technique for cutting sharp tips. By positioning the Pt/Ir wire close to the end of the vise and using longer lengths of wire, a consistent, sharp bias is created. Moving the cutters in the direction indicated by the arrow helps prevent the tip being blunted by the cutters.

surface is so flat and clean, the tip is unlikely to collide with anything. The downside of this method is that experiments are typically focused on spectroscopy, and a tip can produce flat, low noise topography while still being undesirable for spectroscopy. If a step edge can be well-resolved by the topography, that provides strong evidence that the tip is suitable for spectroscopy; however, there are not step edges in every scan window.

The second method, spectroscopy, is a reliable way to determine if the tip is suitable for the experiment. It's necessary to do spectroscopy on a sample with spectroscopic signatures that can be resolved at room temperature, like Bi_2Se_3 . This method is, however, more dangerous for the tip. Feedback is off during spectroscopy, so vibrations that cause the tip and sample to drift closer to each other can cause the tip to make contact with the surface, blunting it. It's not impossible to do get reliable spectroscopy at room temperature, as detailed in Chapters 4 & 5. To achieve increased stability at room temperature, the spectroscopy should be conducted on a platform with a flange like the Joe Box.

The final tip testing method is a direct test of the quality of the tunneling barrier. Similar to spectroscopy, this method is conducted at a single location on the surface. The measurement is one of the tunneling current as a function of tip-sample separation by using the feedback to pull the tip away from the sample while measuring the tunneling current. This data can be fit with Equation 2.3 to provide an estimate for the height of the tunneling barrier. The tunneling barrier should be of a similar height as the work function of the material. Because the tip-sample separation is being used as the independent variable, this method also requires a high level of stability.

CHAPTER 4

GAS EXPOSURE MEASUREMENT METHODOLOGY

The objective of this experiment is to examine the effects N_2 gas can have on the density of electronic states in Bi_2Se_3 as measured by tunneling spectroscopy. First, this chapter will explain the salient features of the Bi_2Se_3 topological insulator. This includes the source of the topological phase, the effects of selenium vacancies, and the topographical signatures of selenium vacancies. All of this background information will comprise Section 4.1. Section 4.2 will detail how the experiments were carried out. Chapter 5 will contain the results and analysis for these experiments.

4.1 Effects of Selenium Vacancies in Bi_2Se_3

Bi_2Se_3 is one of the most widely studied strong, 3D topological insulators (TIs) due to several features that make it convenient for experimental probes. Bi_2Se_3 has a quintuple layer structure comprised of three layers of Se interspersed with two layers of Bi, as shown in Figure 4.1. Within a quintuple layer, the atoms are covalently bonded. The forces keeping the layers bound to each other are of the weaker, Van der Waals variety. This means that Bi_2Se_3 can be easily cleaved using scotch tape to peel off the top quintuple layers, exposing a fresh surface. Electronically, Bi_2Se_3 has a single Dirac cone with topological class (1;000) [13]. Theoretical details on topological phases and invariants can be found in Section 2.3. Furthermore, Bi_2Se_3 has a band gap of 0.3 eV which is large compared to the characteristic energy scales at room temperature, $kT = 25.85$ meV for $T = 300$ K. This means that the topological insulator behavior can be observed at room temperature. The single Dirac cone is a linear dispersion relation for 2D surface states. It is easy to show that a linearly dispersing, 2D electron gas also has density of states increase linearly with energy. This means that the STM spectroscopic signature of Bi_2Se_3 is distinct with a valence band, Dirac cone, and conduction band, as shown in Figure 4.2.

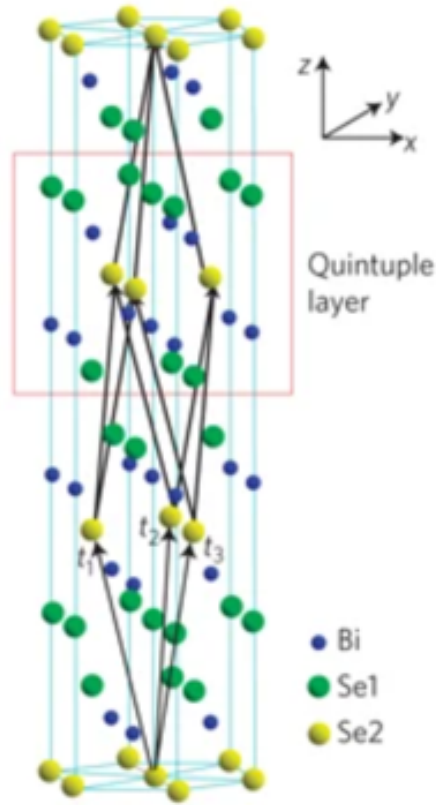


Figure 4.1 The crystal structure of Bi₂Se₃. A single quintuple layer is highlighted by the box. From bottom to top the five layers are Se, Bi, Se, Bi, Se. The quintuple layers are weakly attracted to each other by Van der Waals forces. Within the quintuple layer, the atoms are covalently bound. Adapted from Ref[41].

The details of how the topological phase arises in Bi₂Se₃ were worked out by Zhang *et al.* utilizing a key insight from Fu & Kane [7, 41]. Fu & Kane demonstrated that the \mathbb{Z}_2 topological invariant in TIs with inversion symmetry can be calculated from the total ground state parity. The topological invariant, $\nu = 0, 1$, can be calculated from

$$(-1)^\nu = \prod_i \delta_i. \quad (4.1)$$

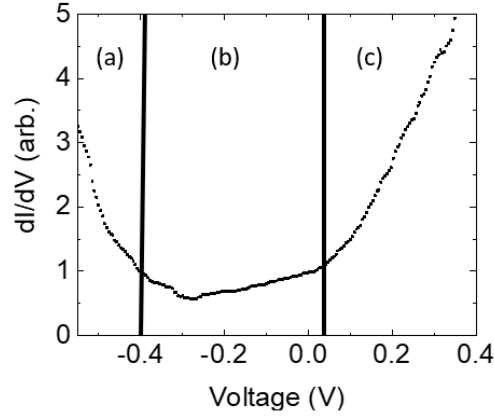


Figure 4.2 Representative tunneling conductance spectroscopy taken on n-type doped Bi_2Se_3 at a temperature of 77K, divided into three distinct regions. Bi_2Se_3 is commonly n-type doped due to selenium vacancy defects. (a) The valence band, characterized by the high density of states. It's estimated here that the valence band ends at -400meV. (b) The Dirac cone which comes to a minimum known as the Dirac point at approximately -280meV. The Dirac cone is characterized by linear density of states as a function of energy. (c) The conduction band, characterized by the high density of states. In n-type doped samples it is common to find the edge of the conduction band close to the Fermi level (0V on the tunneling conductance spectroscopy.)

Here, δ_i are quantities that are ± 1 and are indexed with the 8 high symmetry points in the 3D Brillouin Zone. The δ_i can be calculated from

$$\delta_i = \prod_{m=1}^N \xi_{2m}(\Gamma_i). \quad (4.2)$$

Where the $\xi_{2m}(\Gamma_i) = \pm 1$ are the parity eigenvalues of the occupied energy bands at the high symmetry points. The bands are counted in pairs because $\xi_{2m} = \xi_{2m-1}$ due to Kramers degeneracy. The δ_i can also be used to calculate the weak topological invariants, but that is outside the scope of this work [7]. Zhang *et al.* calculated the energy levels of the bands in Bi_2Se_3 while isolating the effects of different contributions to the band energy, shown in Figure 4.3. The result is that after chemical bonding and crystal field splitting effects have been accounted for, there are two energy levels, $|P1_Z^+\rangle$ and $|P2_Z^-\rangle$, with opposite parity close to the Fermi level. When spin orbit coupling is turned on, these bands invert, changing the total ground state parity. This drives the crystal into the topological phase.

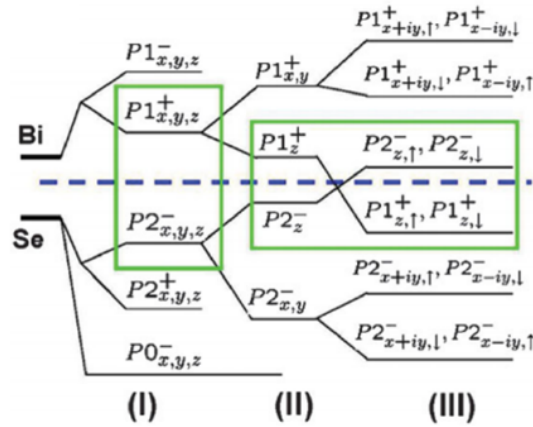


Figure 4.3 Ref[41]. Calculated level splitting in Bi_2Se_3 with the dashed line indicating the Fermi level. The levels shown here are the p-orbitals closest to the Fermi level from both Bi and Se: Bi ($6s^26p^3$) and Se ($4s^24p^4$). (I) Includes only contributions due to chemical bonding. Highlighted in the box are $|P1^+\rangle$ and $|P2^-\rangle$, which are the levels closest to the Fermi level. The superscripts \pm indicate the parity of the states. Chemical bonding causes these states to hybridize, pushing the Bi level up and the Se levels down. (II) This stage adds contributions due to the crystal field. Here, the z orbitals split off from the x and y orbitals leaving $|P1_z^+\rangle$ and $|P2_z^-\rangle$ at the Fermi level. (III) Finally, the effects of spin-orbit coupling are included. This splits the z orbitals away from the now-combined $x + iy$ orbitals. The two states closest to the Fermi level cross the Fermi level, thereby changing the total ground state parity of the system, driving it into the topological phase.

Though Bi_2Se_3 has several features that make it ideal for experimental probes, there is a major drawback with the material. Bi_2Se_3 tends to have Se vacancies with most growth methods which have the effect of n-type doping the band structure [36]. This means that the Dirac point is typically 300 meV below the Fermi level and the conduction band is close to the Fermi level. Without these surface vacancies, the Dirac point would be at the Fermi level [37]. This obfuscates one of the defining features of a topological insulator: an insulating bulk with conductive surface states. It also is sub-optimal for creating topological superconducting phases in heterostructures (more detail in Section 2.4). Subsurface vacancies create characteristic triangle-shaped features in topography when the bias voltage is tuned to be resonant with the defect states. Sergei Urazhdin in the Tessler group was the first to characterize these defect states in Reference [36]. This result has been reproduced in the literature, with a particularly detailed study by Dai *et al.* in Reference [5]. Figure 4.4 shows the Urazhdin and Dai results side-by-side. There are theoretical and experimental studies

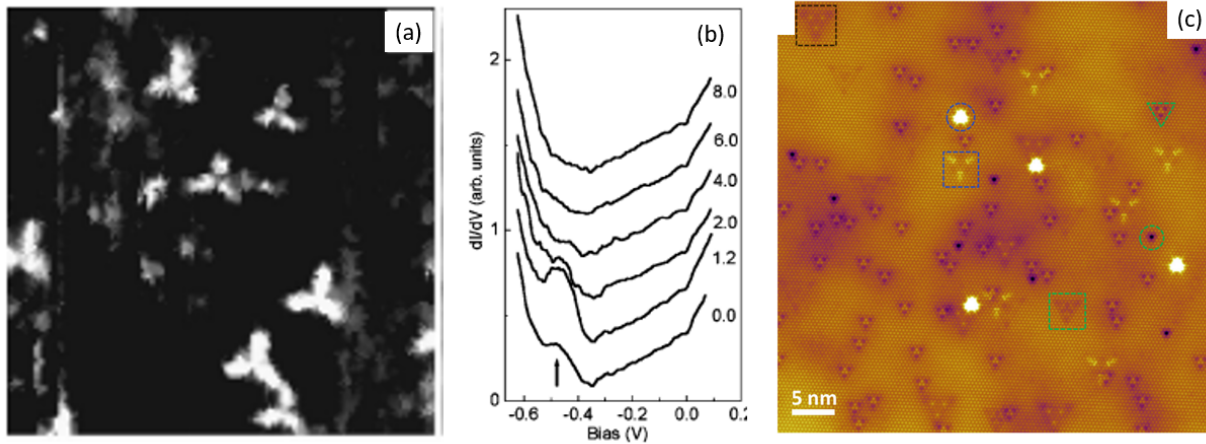


Figure 4.4 (a) First observation of subsurface Se vacancy defects in current imaging tunneling spectroscopy with 30 x 30 nm scan range. The bias voltage was set to -0.45 V, indicating heightened density of states at that energy. These clover-leaf features are due to the effects of the vacancy traveling up the p bonds. (b) Tunneling spectroscopy at various distances from the center of a clover-leaf indicated by numbers in nanometers on the right. These spectra confirm the effect of the defect is to create extra states at -0.45 eV. (c) Observations of the topographic effects of many different Se vacancies. Depending on which Se atom is vacant, the characteristics of the clover-leaf are different. Adapted from Ref[36](a),(b) and Ref[5](c).

that show NO_2 and O_2 gas can bind to these Se vacancies and p-type dope the material [19][14]. The experiment presented in the next section will explore the possibility of N_2 gas having a similar effect.

4.2 Time-Resolved Room Temperature Measurements

The experimental set-up is very simple. A glove box is over-pressured with ultra-high purity helium gas through a flow-meter. The glove box is the "Joe Box," so-called because it was constructed by Joe Kitzman during his summer project with the Tessmer group. A diagram of the experiment, along with a picture of the glove box can be seen in Figures 4.5 and 4.6. A single crystal of Bi_2Se_3 is cleaved with tape once the glove box has reached 99.999% purity. The amount of air remaining in the glove box is calculated using Equation 3.1 by measuring the volumetric flow rate, the time, and the volume of the glove box. Next, the cleaved Bi_2Se_3 is loaded into the microscope attached to the glove box with a flange. The sample is carefully walked into range using

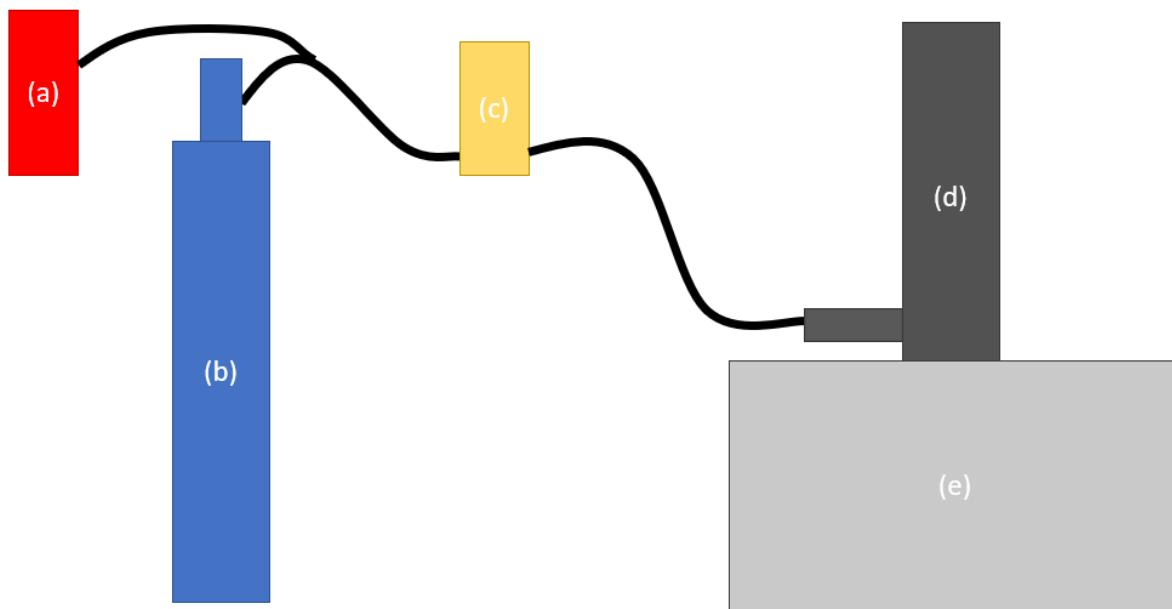


Figure 4.5 Diagram of the gas exposure experiment. (a) Ultra-high purity (UHP) N₂ source from the building's liquid nitrogen boil-off. (b) UHP He gas cylinder. Both the N₂ and He sources lead to a line going into the flow meter (c). The gas sources can be shut off independently. At least one source is always on to ensure air does not backflow into the glove box (e). The STM (d) is attached to the glove box by flange.

the Feedback Detect walking method to preserve tip quality. With the tip in range, tunneling barrier measurements are conducted to test the height of the tunneling barrier and the quality of the tip. Tunneling spectroscopy are taken at a single location on the surface over the course of 30 minutes to establish a baseline. The tunneling spectroscopy is paused so that the feedback can protect the tip while a source of ultra-high purity N₂ gas is turned on and the helium gas source is turned off, in that order. More tunneling spectroscopy is acquired at the same location over the course of 50 minutes. Finally, the tunneling barrier is measured again to see if it has changed over the course of the experiment. More details on all of the experimental methods employed here can be found in Chapter 3.

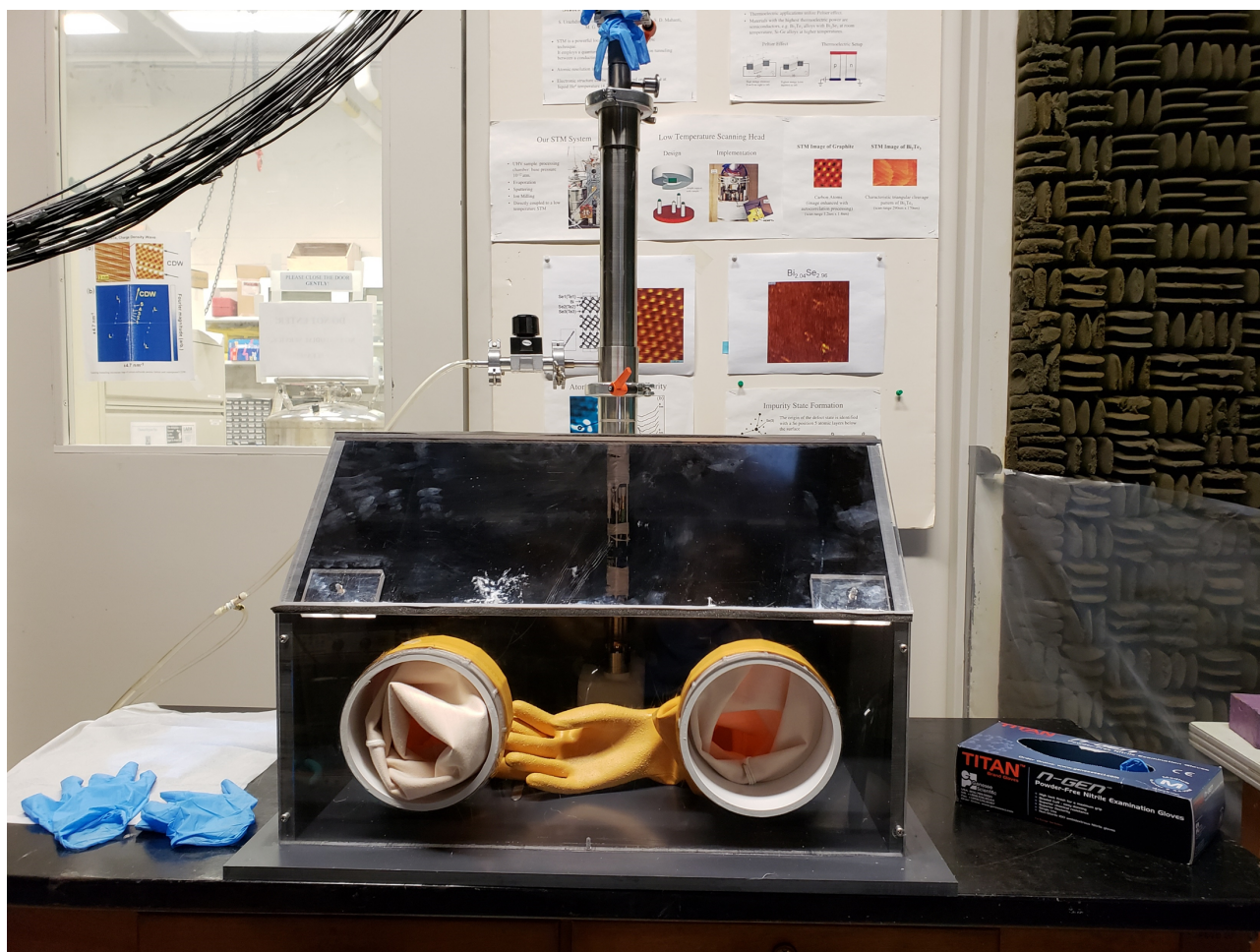


Figure 4.6 The glove box used for the room temperature gas exposure experiments. It was designed and built by Joe Kitzman during his summer project in the Tessmer group, so it is frequently referred to as the "Joe Box." Tape is wrapped around the front panel to create a better seal. It's clear that the box is overpressured when the yellow gloves are compressed by the pressure in the box.

4.3 Atomic Resolution Topography

The same Bi_2Se_3 crystals used in the experiment described in the previous section were loaded into the cryogenic STM apparatus. Details on this apparatus can be found in Section 3.2. The sample was loaded into the load-lock and cleaved after purging the space with helium gas. Cryostat preparation followed the usual procedure for experiments at 77 K. Topographic measurements were taken on the crystal in vacuum. Observing clover-leaf defects requires the bias voltage to be tuned to be resonant with the surface states. This means areas need to be scanned at a variety of bias

voltages between -500 and -300 mV until the defects are observed. It's possible to estimate the resonant voltage by taking tunneling conductance spectroscopy and setting the bias voltage 50 mV below the Dirac point energy, as shown in Figure 4.4(b); however, there can be significant local variations in the spectra. The signature defects were observed in this experiment at -450 mV bias voltage with 1 nA set current and the feedback integral gain set to 600 nm/V. With these settings, a nearby $5 \times 5 \mu\text{m}$ area was scanned in a 3x3 tiled grid of topographic scans. The position of the scan regions was controlled only using the tip piezo tube, not with sample coarse positioning. This process is designed to be a statistically independent survey of the defect concentration.

CHAPTER 5

GAS EXPOSURE RESULTS AND ANALYSIS

This chapter presents the results of the N₂ gas exposure study. The results of this experiment are quite surprising, as a 50 meV shift in the density of states of Bi₂Se₃ in the presence of nitrogen gas is observed over a time period of 50 minutes. The spectroscopic measurements were acquired in a room temperature glove box. Tunneling barrier measurements show that the effect is likely due to the exposure to gas and not the result of a deteriorating tunneling barrier. The observations are surprising given that molecular nitrogen has a strong triple bond, so it is a relatively inert gas. As discussed in the previous chapter, Bi₂Se₃ is intrinsically n-type doped due to selenium vacancies. These vacancies exist on the surface of the material and are highly attractive for N atoms; however, the attraction of a single vacancy is not strong enough to break the triple bond. To help provide a possible mechanism for this observation, Malsoon Lee at Pacific Northwest National Laboratory collaborated with us to theoretically model the energetics and dynamics of the system. Her calculations found that atomic nitrogen is attracted to selenium vacancies with a binding energy of 4.82 eV, approximately half of what's needed to break the triple bond. She also calculated the expected shift in the density of states from atomic nitrogen to be 450 meV. This suggests that neighboring pairs of vacancies could, in fact, dissociate the nitrogen molecule and produce the diminished shift that we observe experimentally. Furthermore, Malsoon created an *ab initio* molecular dynamics simulation that shows that this is the likely behavior of molecular nitrogen in the presence of a pair of vacancies. The magnitude of the shift is roughly consistent with the number of pairs of selenium vacancies observed via topographic measurements.

5.1 Experimental Results

The main experimental results are summarized in Figure 5.1, which shows the tunneling conductance spectra shift after being exposed to N₂ gas. It's difficult to determine the effect of the shift on the conduction and valence bands, due to thermal broadening. Even with no thermal broadening,

the transition from the bands to the Dirac cone can never precisely be determined. Instead, the easiest feature to identify in the curves is the Dirac point because the minimum of the curve has less ambiguity than the band edges. Nevertheless, there is still some uncertainty in determining the minimum of the curve. The size of the error bars in Figure 5.1(c) are given by the standard deviation of several measurements of the Dirac point energies taken before the N₂ flow began (before $t = 0$). As a guide to the eye, we include a curve based on the Langmuir adsorption model with a changing partial pressure [24]. It is not a theoretical fit to the data with measurable parameters. Here, it shows the qualitative expected behavior of the Dirac point energy over time if it is due to a gas adsorption process. The results show that the Dirac point energy shifts a total of 50 meV over the course of 50 minutes. Measurements of tunneling current as a function of tip-sample separation confirmed that the tunneling barrier remained consistent during this time frame. Usage of this method of tip characterization is explained in Section 3.3. The tunneling barrier measurements were conducted before the first spectra were taken and after the spectra were taken at $t = 50$ minutes. Spectra taken the next day on the sample as it remained in the N₂ environment are consistent with the interpretation that the effect has fully saturated. It should be noted, however, that contamination effects from other gases become more likely on these longer time scales. Ultra-high purity N₂ gas still has 0.001% other gases, and the glove box can outgas other contaminants, such as water vapor.

After the room temperature experiment, the sample was loaded into the cryostat for low-temperature (77K) topography measurements. The theoretical model, explained in detail in the next section, suggests that N₂ molecules can dissociate and bind to pairs of surface selenium vacancies. It also provides estimations of how the density of states spectra would be affected by nitrogen and other dopants. Topography measurements can show evidence of selenium vacancies and can offer a crude estimate of the concentration of these vacancies on the surface. This estimate, along with the density of states calculations, can be compared to the shift shown in Figure 5.1. Topography showing evidence of Se vacancy defects is shown in Figure 5.2. Because the clover-leaf signatures

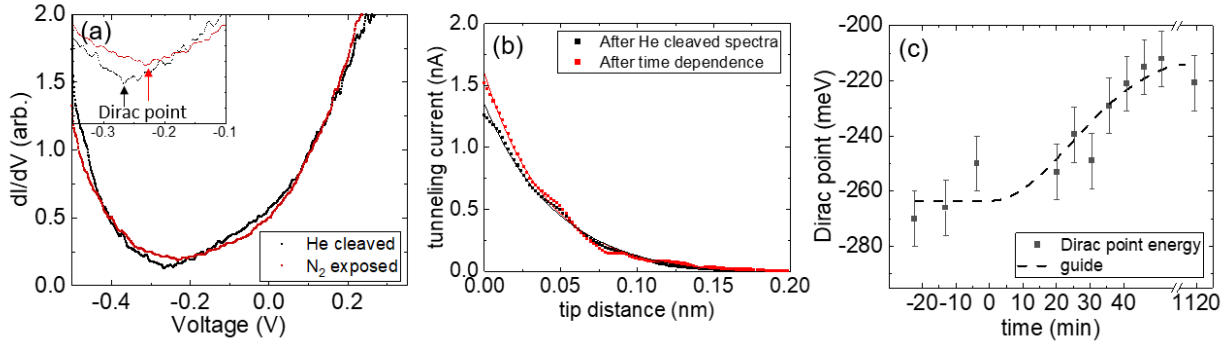


Figure 5.1 (a) Representative tunneling conductance spectra acquired on Bi_2Se_3 cleaved in He (black) and exposed to N_2 (red) for 35 minutes. These spectra are each an average of 50 curves taken at room temperature at the same sample location with a tunneling barrier established by a -0.5 V bias applied to the sample and a tunneling current set point of 0.3 nA with the tunneling conductance normalized to the value at 0.1 V. The inset is a smaller scale focused on the Dirac points of the two spectra. (b) Tunneling current vs. tip distance from the initial set point measurements demonstrating a robust tunneling barrier throughout the experiment. Both tunneling barriers are calculated to be greater than 5 eV, consistent with the work function of the material. The exponential decay fits are solid lines on the plot. (c) A compilation of identified Dirac point energies taken continuously at the same spot. The crystal was first cleaved in He and spectra were taken at a single location on the surface. $t = 0$ is set when the N_2 gas was introduced to the system. Data taken before the scale break are extracted from averages of 50 spectra. After the scale break, we show a final point representing an average of 800 spectra taken the next day. The dashed line is a phenomenological guide to the eye.

of subsurface defects are much larger than the atomic spacing, they are much easier to observe than surface vacancies. An example of observations of these defects in this experiment is shown in Figure 5.2(a). Reliably observing surface vacancies requires flawless atomic-resolution topography, as dark spots in the topography can be due to noise fluctuations or any non-conducting contaminant on the surface. Furthermore, multiple scans cannot be averaged together to enhance the signal-to-noise ratio due to drift. Figure 4.5(b) is an example of a 30×30 nm atomic resolution scan showing evidence of surface vacancies.

Formation energy calculations suggest that vacancies are approximately equally likely to be in any lattice location. This means that the count of subsurface vacancies is a reasonable proxy for surface vacancies. The result of this count is a Se vacancy concentration of $n_{\text{Se},V} = 6 \times 10^{-4}$. The direct count of surface vacancies from atomic resolution topography results in $n_{\text{Se},V} = 6 \times 10^{-3}$.

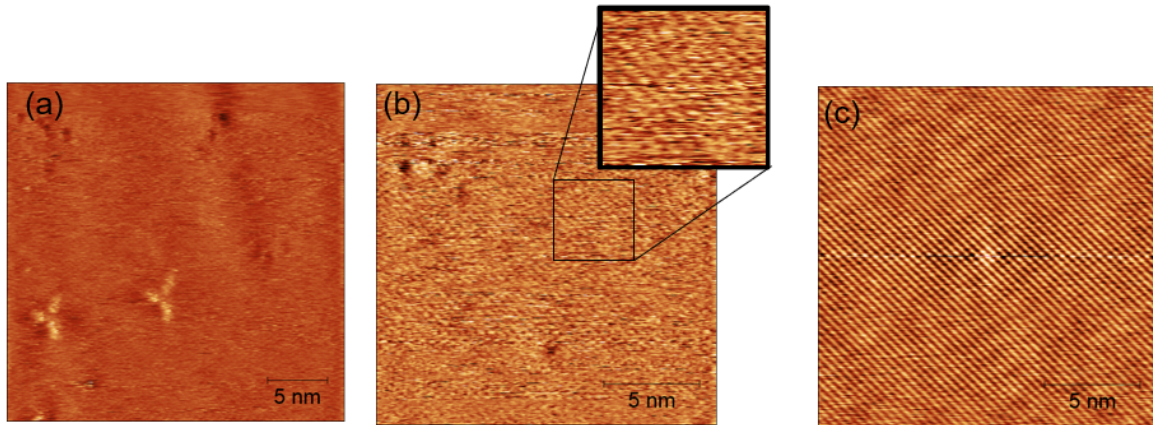


Figure 5.2 STM topographic images. The images were acquired at 77 K with a bias voltage of -0.450 V and a set current of 1 nA. These images have been flattened via polynomial background fitting. (a) Topography shows the triangular spectroscopic signature of sub-surface defects. (b) Atomic resolution topography with indications of surface vacancy defects with a zoomed-in inset showing the atomic resolution. (c) Topography corrected with the autocorrelation function.

Taking this upper-bound estimate of the defect concentration and assuming that all pairs of defects are occupied by a pair of nitrogen atoms, the result is a rough estimate of 30 meV for the total expected shift. This analysis neglects the possibility that given a N_2 molecule physisorbed near a Se vacancy forming a Se-V- N_2 complex, another Se vacancy can diffuse to the site of that complex and form a Se-VV- N_2 complex followed by the dissociation of the N_2 molecule. Fully exploring this possibility requires further careful analysis.

5.2 Theoretical Results

All credit for these theoretical calculations and simulations belong to Malsoon Lee and Subhendra Mahanti [9]. Using density functional theory (DFT), the surface local density of states for a 6 quintuple layer (QL) Bi_2Se_3 slab with a 3×3 supercell in the basal (xy) plane was calculated. The optimized lattice parameters of the supercell are $a = 12.414 \text{ \AA}$ and $c = 70.0 \text{ \AA}$ with 15 \AA interlayer space. As model systems, the slab was first prepared with and without a selenium vacancy on the surface Se layer, then added N_2 , N, and He (loosely referred to as dopants) on the surface. For the DFT studies scalar relativistic electronic structure calculations were carried out using the projector

augmented wave (PAW) methods [22] and the Perdew Burke Ernzerhof (PBE) generalized gradient corrected exchange correlation functional [26] as implemented in the VASP package [21]. An energy cutoff of 400 eV was used for the plane-wave expansion, with a total energy convergence on the order of 10^{-4} eV. Spin orbit interaction (which are essential to get the Dirac cone states) have been included using a second variational approximation [29]. Using optimized structures, total (TDOS) and projected density of states (PDOS) was calculated using $3 \times 3 \times 1$ k-points.

Ab initio molecular dynamics (AIMD) simulations combined with a Blue Moon ensemble method [33] were performed at $T = 300$ K as implemented in the CP2K package [23] to estimate the Helmholtz free energy of the dissociative adsorption of N_2 molecule into the surface in the presence of Se vacancies by computing the potential of mean force (PMF). Due to computational limitation, a model of 3QL Bi_2Se_3 slab with 6×6 supercell in the basal (xy) plane was adopted for this study. As a prelude to these calculations, Se-vacancy formation energy (E_f) was calculated to verify the existence of two Se vacancies on the surface so that two dissociated N atoms may be adsorbed on the surface. E_f was calculated using $E_f = E_{defect} - (E_{pristine} - n_{Se}\mu_{Se})$ where E_{defect} and $E_{pristine}$ are the total energies of the supercell with and without Se vacancies respectively, and n_{Se} is the number of Se vacancies and μ_{Se} is the chemical potential of Se [11]. μ_{Se} is obtained by calculating the energy per atom using a $2 \times 2 \times 2$ supercell of the α -monoclinic Se crystal [4].

To understand the origin of the shift in the energy of the Dirac point (relative to the Fermi energy) with N_2 exposed system, DFT calculations were performed. Structures were optimized with and without dopants of He/ N_2 /N on the surface in the presence and absence of Se vacancy on the surface whose structures are shown in Figure 5.3. Optimized structures of doped systems with Se vacancy reveal that both He atom and N_2 molecule are several angstroms above the surface. For a quantitative description of the position of the dopants with respect to the surface, a distance $\Delta z(X) = z(X) - z(Se1)$ is defined, where $z(X)$ is the z coordinate of X and Se1 is the surface Se atom. The calculations show $\Delta z(N) = -0.77 \text{ \AA}$, $\Delta z(He) = 2.01 \text{ \AA}$, and $\Delta z(N_2) = 2.06/3.16 \text{ \AA}$ with a Se vacancy. For the N_2 molecule, the difference in the z-coordinates of the two N atoms is 1.1 \AA ,

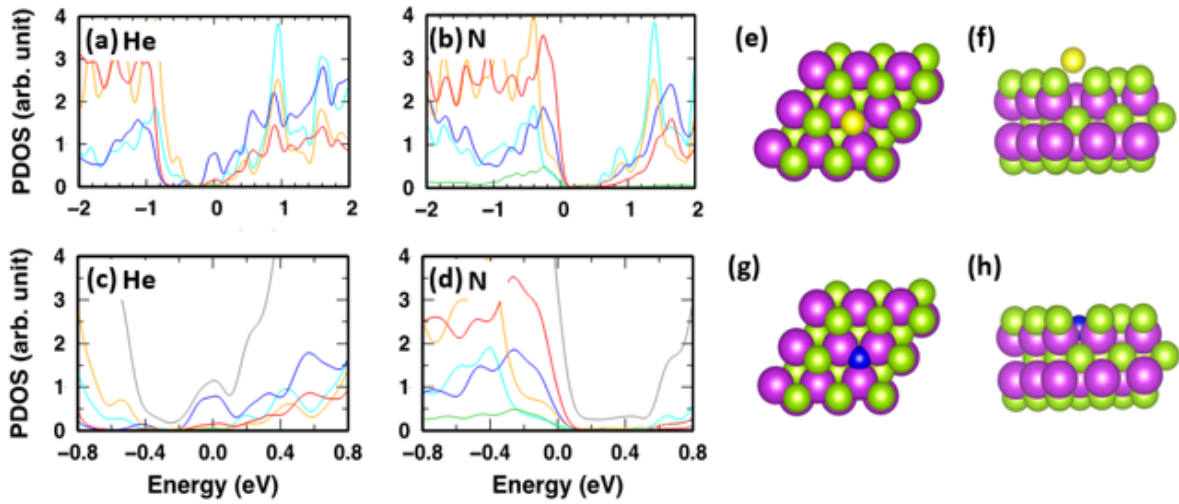


Figure 5.3 (a) and (b) Calculated density of states for He and N adsorbed Bi_2Se_3 in the presence of Se vacancy. (c) and (d) DOS calculations corresponding to the energy scale of tunneling measurements. DOS contributions from top layer representing surface atoms and middle layer representing atoms in bulk Bi_2Se_3 are shown. The lowest energy structure of the top quintuple layer of Bi_2Se_3 with a Se vacancy with dopant of (e), (f) He and (g), (h) N are shown where (e) and (g) show top view and (f) and (h) show side view of the structures. Color code: (a)-(d) grey-TDOS, red- Se top layer Se , blue- Bi top layer, orange-middle layer Se , turquoise-middle layer Bi , green-dopant.; (e)-(h) magenta - Bi , green - Se , yellow - He, and blue - N.

which is very close to the bond length of a N_2 molecule, 1.098 \AA , indicating that the molecular axis is nearly perpendicular to the surface in the presence of Se vacancy. These distances also suggest that He and N_2 molecule are physisorbed whereas N atom is chemisorbed in the presence of Se vacancy at the surface. In comparison, on the pristine surface, N atom is chemisorbed ($\Delta z = 1.3 \text{ \AA}$), while He and N_2 molecule are far away from the surface with $\Delta z = 3.26$ and $4.14/4.32 \text{ \AA}$. These results are consistent with the adsorption energy (E_{ad}) results as discussed below.

With optimized structures, the adsorption energy E_{ad} is estimated as the difference between the minimum energy of the combined system and the energy of the surface plus the energy of the free dopant. A negative E_{ad} implies the dopant is bound to the surface. The calculations show, for He, $E_{ad} = -0.02 \text{ eV}$ when the He is above the Se vacancy whereas the He atom does not bind with a clean surface which is consistent with Δz calculations (weak van der Waal's interaction is not

adequately incorporated in the theoretical calculations). For N_2 molecules, $E_{ad} = -0.36(-0.09)$ eV with (without) a Se vacancy. These numbers suggest that the He atoms and N_2 molecules are physisorbed on the surface with attraction to the Se vacancy, particularly by the N_2 molecules. In contrast, the calculations show that E_{ad} is the lowest when a N atom is brought to the selenium vacancy and the corresponding adsorption energy is -4.82 eV, indicating very strong chemical binding between the N atom and vacancy (actually, the neighboring Bi atoms of a Se vacancy). It is interesting to note that a neutral N atom binds rather strongly with the clean surface of Bi_2Se_3 showing $E_{ad} = -1.78$ eV compared with other dopants. Recently, Wang et al [38] have published a paper discussing the formation energy and electronic structure of N atom dopants (N replacing Se as defects) in bulk Bi_2Se_3 .

The density of states (DOS) were calculated of He/N adsorbed Bi_2Se_3 in the presence and absence of Se vacancy as shown in Figure 5.3. Figures 5.3(a) and 5.3(b) show the total DOS and contributions of adsorbed atom as well as Bi/Se atoms from different QL representing bulk (middle layers) and surface (top layer) in an energy range between -2 and 2 eV while Figure 5.3(c) and 5.3(d) show those in a narrow energy range between -0.8 and 0.8 eV. The calculations suggest a significant difference between the position of the chemical potential and the minimum of DOS in the gap region associated with the DP. For He, DP is 250 meV below the chemical potential, see Figure 5.3(c). Also one sees a small peak in the DOS near the chemical potential (Figure 5.3(c)), which is ascribed to the Se1 vacancy induced surface state [30]. Clearly, states above the DP are occupied by electrons donated by the Se1 vacancy. The situation changes when one has a bound N atom as shown in Figure 5.3(d). The Se1 vacancy induced surface defect state is moved away from the gap region. The chemical potential falls below the DP by 150 meV and even goes below the valence band maximum, indicating hole doping. The direction of the shift is consistent with the STM experiment. However, the magnitude of the shift in the calculations (400 meV) is much larger than what was observed in the experiment (50 meV.) This suggests that only a fraction of the selenium vacancies bind with N_2 molecules. Also, the experiment involves molecular N_2 , not

atomic N, and our calculations suggest that molecular N_2 would not cause the observed shift in the Dirac point. This leads to the suggestion that molecular N_2 somehow dissociates when interacting with the surface.

In order to understand the energetics of a molecular N_2 adsorbing as N atoms on the Bi_2Se_3 surface (with and without Se vacancy) one must look at the binding energy of a N atom on the Bi_2Se_3 surface. This is found here to be 1.78 eV without a Se vacancy and 4.82 eV with a Se vacancy. The nominal bond dissociation energy of a free N_2 molecule, that is the energy to break a N_2 molecule into two N atoms, is 9.79 eV [6]. Thus breaking the N_2 bond on a clean Bi_2Se_3 surface will cost nearly 4.97 eV, clearly impossible. However, if there are two Se vacancies then the energy cost to dissociate is only 150 meV, not difficult to circumvent. This possibility is examined with an *ab initio* molecular dynamics (AIMD) simulation combined with a Blue Moon sampling method, where the Helmholtz free energies are measured of N_2 molecule adsorption on the surface as a function of the z-distance between one of N atoms and the surface as plotted in Figure 5.4(a). It shows the adsorption free energy barrier of 140 meV, while its desorption energy barrier is 350 meV. These results indicate dissociative adsorption of N_2 molecule is favorable in the presence of two Se vacancies on the surface. Figures 5.4(b) and (c) are snapshots of the nitrogen atoms' positions when the free energy is minimized which occurred at the z-distance of 1 Å between the nitrogen atom and the surface. The figures clearly show that one nitrogen atom occupies one Se vacancy while the other atom is bound to one Se and one Bi atom below the surface instead of occupying the other vacancy.

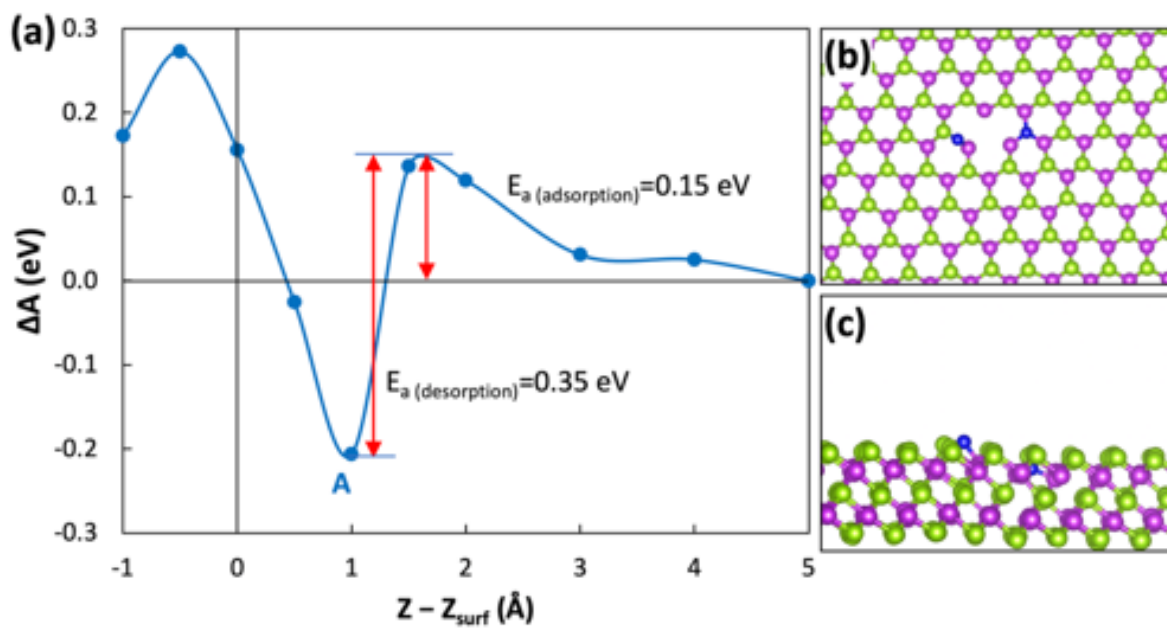


Figure 5.4 (a) is a plot of the change in the Helmholtz free energy of the N_2 molecule as it interacts with the surface. (b) and (c) show a top and side view of the final position of the N atoms, respectively. Color code of atoms: green – Se, magenta – Bi, blue – N.

CHAPTER 6

JOSEPHSON VORTEX EXPERIMENT DESIGN, METHODS AND SIMULATIONS

This chapter explains the experimental design, methods, and simulations for the Josephson vortex experiment. The Josephson vortex experiment is a proposal to look for Majorana zero modes in Josephson vortices on superconductor-topological insulator-superconductor (S-TI-S) structures. This experiment is theoretically motivated by a paper by Fu & Kane that suggests such a system may support Majorana zero modes [8]. The experimental design is also motivated by an experimental study by Rodichev and collaborators on Pb island Josephson junctions [8], who directly imaged Josephson vortices in traditional normal metal Josephson junctions (SNS). The vortices in these junctions show a diminished superconducting energy gap with the density of states (DoS) approaching the normal metal baseline at zero energy. A signature of the Majorana zero modes would be similar but with a peak at zero energy, as shown in my simulations at the end of the chapter. Creating an S-TI-S device requires several precise sample fabrication steps. For this experiment, the Josephson junctions will be long line junctions of niobium on Bi₂Se₃. These long islands of Nb, or "fingers," will have vortices form between them in the presence of an external magnetic field.

6.1 Device Motivation and Design

Theoretical work by Fu & Kane suggests that S-TI-S Josephson junctions may support Majorana states [8]. Their work begins with a simple Hamiltonian for the surface states on a strong, 3D, TI with a single Dirac cone:

$$H_0 = \psi^\dagger (-iv\vec{\sigma} \cdot \nabla - \mu)\psi \quad (6.1)$$

Where $\psi = (\psi_\uparrow, \psi_\downarrow)^T$ are electron field operators, $\vec{\sigma} = (\sigma^x, \sigma^y)$ are Pauli spin matrices, v is the Fermi velocity, and μ is the chemical potential. Superconductivity is added to this Hamiltonian directly. To achieve this situation physically, it is possible to use the superconducting proximity effect; essentially, superconducting electrons can leak into the TI by placing a superconducting

material next to it. It's convenient to work in the Nambu basis for superconductivity where $H = \Psi^\dagger \mathcal{H} \Psi / 2$ and $\Psi = ((\psi_\uparrow, \psi_\downarrow), (\psi_\downarrow^\dagger, -\psi_\uparrow^\dagger))^T$

$$\mathcal{H} = -iv\tau^z \sigma \cdot \nabla - \mu\tau^z + \Delta_0(\tau^x \cos \phi + \tau^y \sin \phi) \quad (6.2)$$

Here $\vec{\tau}$ are Pauli matrices acting on the particle/hole components of the wavefunction, Δ_0 is the superconducting energy gap, and ϕ is the superconducting phase. In the limit $\mu \gg \delta_0$, this Hamiltonian resembles the spinless $p_x + ip_y$ superconductor [8]. It was already predicted that vortices in a $p_x + ip_y$ superconductor could support Majorana bound states with non-Abelian statistics [27][15]. To find the solutions for bound states in vortices, it's convenient to work in cylindrical coordinates ($\Delta(r, \theta) = \Delta_0 e^{ir\theta}$) and set $\mu = 0$. Fu and Kane found the solutions for 0 energy bound states to be [8]:

$$\xi_0^\pm(r, \theta) = \chi^\pm e^{-\int_0^r dr' \Delta_0(r')/v} \quad (6.3)$$

Here $\chi^+ = ((0, i), (1, 0))^T$ and $\chi^- = ((1, 0), (0, -i))^T$. All that is left, is to break time-reversal symmetry and therefore Kramer's degeneracy. With Kramer's degeneracy, the 0 modes would come in pairs. Because Majorana modes are their own anti-particle, these modes would automatically annihilate. One way to overcome this obstacle is with an external magnetic field. This would add a Zeeman term to the Hamiltonian, breaking time-reversal symmetry. An external magnetic field has the added benefit of creating the necessary vortices to localize the Majorana zero modes.

Roditchev et al. have directly observed superconducting vortices in superconductor-normal metal-superconductor (SNS) junctions [28]. In their experiment, they were looking at superconducting lead islands interspersed with normal metal lead as the weak link for the Josephson junction. An out of plane magnetic field was applied, which causes the phase of the superconducting condensate to vary spatially according to:

$$\phi = \phi(r_2) - \phi(r_1) - (2e/\hbar) \int_{r_1}^{r_2} \vec{A} d\vec{l} \quad (6.4)$$

Here $\phi(r_i)$ is the phase of the superconducting condensate at positions r_i on the edge of the two junctions and \vec{A} is the vector potential for the external magnetic field. The vortices were observed

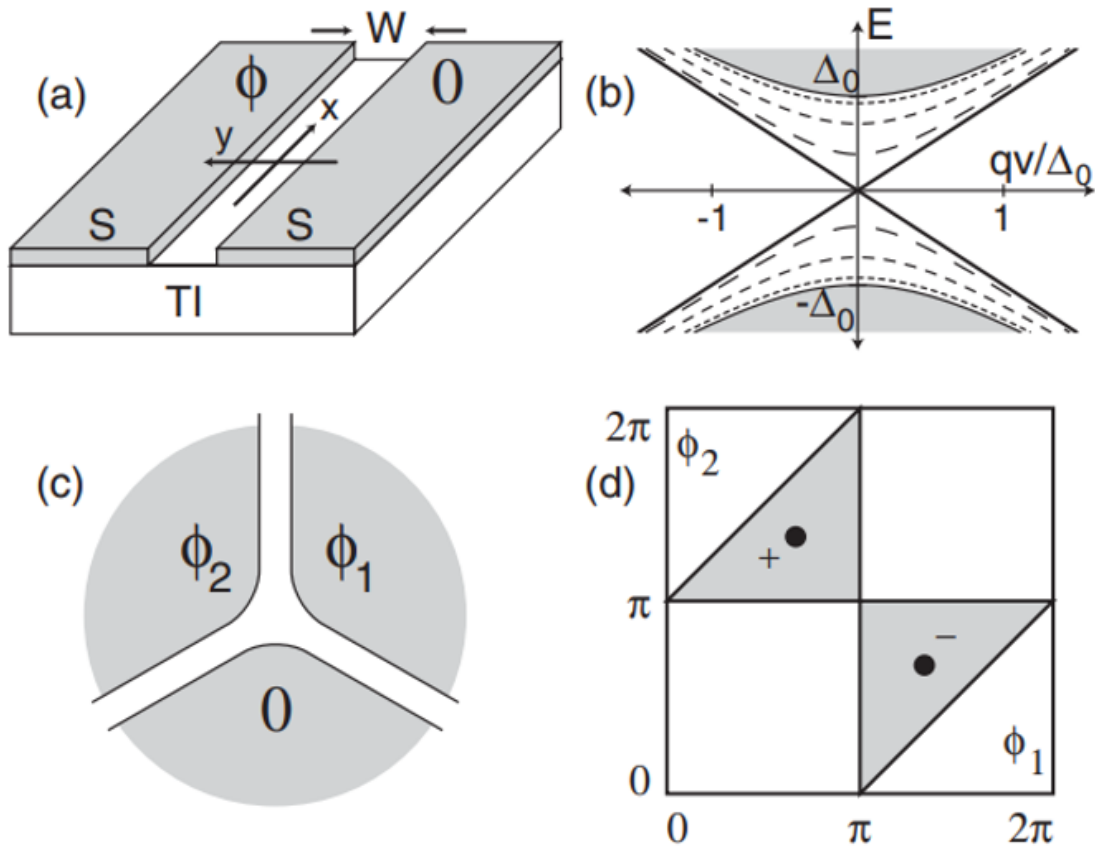


Figure 6.1 (a) Diagram of an S-TI-S Josephson junction. According to the Fu-Kane theory, a linearly dispersing 1D line of Majorana modes forms along the x-axis in the junction when the phase difference across the junction $\phi = \pi$. The plan for the experiment is to study vortices in such junctions which theoretically support Majorana zero modes. (b) The dispersion relation for the 1D Majorana modes forms the solid black lines crossing zero energy. The dashed lines are the same modes with the addition of a mass term. (c) An S-TI-S tri-junction. This geometry is proposed as a viable platform for exchanging Majorana zero modes. (d) A phase diagram for the tri-junction. Majorana modes form in the junction when the phase relationship of the three superconductors lies within the grey regions. Adapted from Ref [8].

using scanning spectroscopy at 0 bias with an STM. Superconducting regions in the material have fewer fermion states close to the Fermi level, as electrons close to the Fermi level will form Cooper pairs that are not detected with conventional spectroscopic techniques. This means that superconducting regions have depressed tunneling conductance at 0 energy, as shown in Figure 6.2(e). In Josephson vortices, the superconductivity is diminished by destructive interference in the weak link material between the superconducting condensates from the two nearby islands. Therefore, vortices are identifiable by flat tunneling conductance, as shown in Figure 6.2(f).

The plan for our experiment is to apply Fu & Kane's theory to Roditchev et al.'s experimental design. Instead of superconducting islands with normal metal as a weak link material, the experiment will have superconducting islands Nb islands with Bi_2Se_3 as a weak link material, creating an S-TI-S junction, as shown in Figure 6.3. The expected experimental signature is different than the SNS Josephson vortex experiment in that one expects enhanced tunneling conductance at 0 bias. This expectation is explored in Section 6.3. Nb is chosen for its high T_C and large superconducting gap, as well as its relatively short coherence length. Higher T_C and larger superconducting gap are advantageous for the formation and observation of Majorana zero modes. A short coherence length is necessary for the Nb to remain superconducting while fitting into the design constraints outlined in Section 3.1. The microscope can only accommodate 40nm of tip feedback in the z-direction while having enough lateral motion to scan the full width of the islands (300nm.) Bi_2Se_3 is chosen as the topological insulator due to the group's experience with the material, the large energy gap, and the simplicity of the single Dirac cone.

The sample will be cooled to 4.2K, well below Nb's T_C of 9.25K. An out of plane magnetic field will be applied to create superconducting vortices between the Nb islands. Another difference between this experimental design and the SNS vortex experiment, is the Nb islands will be long, parallel fingers to avoid the "needle in a haystack" problem described in Section 3.1. Each finger is $50\mu\text{m}$ long, 500nm wide spaced 300nm apart. These fingers will be grouped into arrays so that a 1 x 1mm area on the sample is covered with S-TI-S Josephson junctions. The next section will

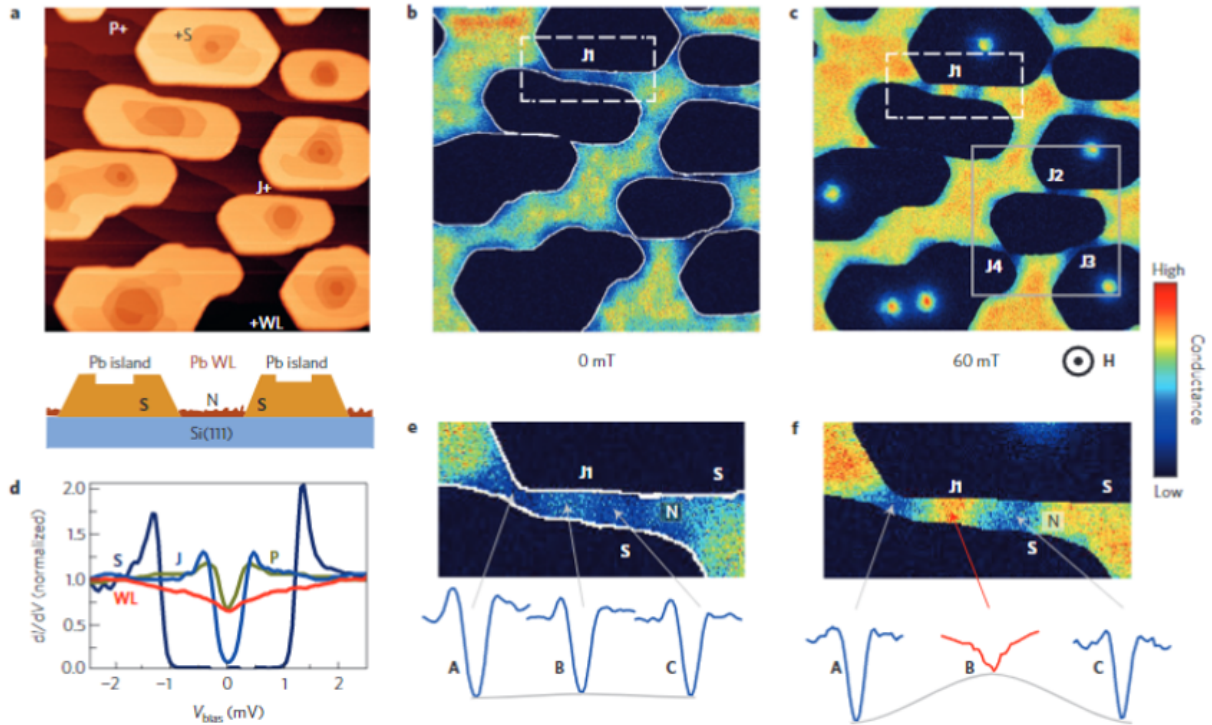


Figure 6.2 The experimental results of Roditchev and collaborators from Ref [28]. (a) Topography of the surface along with a schematic. Pb islands are clearly imaged along with the wetting layer (WL). (b) A tunneling conductance map on the surface with no applied magnetic field at zero bias. As expected, the tunneling conductance on the superconducting islands is suppressed at zero bias due to the formation of the superconducting energy gap. The superconducting proximity effect opens a gap in the normal metal WL close to the islands. (c) A tunneling conductance map on the surface with a 60 mT applied external magnetic field. The superconducting gap closes as vortices form on and between the islands. Tunneling conductance returns to the baseline level observed in the normal metal far from an island. (d) A plot of tunneling conductance as a function of energy at various locations on the surface: the superconducting islands (S), the normal metal wetting layer (WL) far from an island, a point between two islands (J), and a point close to a single island (P). (e) Plots of tunneling conductance as a function of energy between two islands with no applied field. (f) Plots of tunneling conductance as a function of energy between two islands with 60 mT applied magnetic field.

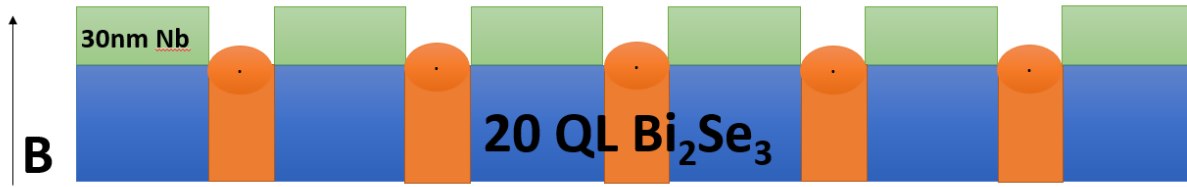


Figure 6.3 My experimental plan, inspired by the theoretical work in Ref [8] and the experimental work in Ref [28]. S-TI-S Josephson junctions are formed with 30 nm thick Nb fingers (S) on 20 QL of Bi_2Se_3 (TI.) The fingers are 500 nm wide and are spaced 300 nm apart. An external magnetic field creates vortices between the superconducting Nb. The experimental signature is distinct from that in Figure 6.2 (f) in that the Majorana zero modes could create additional conductance at zero energy above the baseline. This means that tunneling conductance as a function of bias voltage would show a peak at zero bias rather than simply a diminished energy gap.

explain the experimental techniques used to fabricate these devices.

6.2 Device Fabrication

The devices are fabricated using several different techniques. The base layer is 20 QL of Bi_2Se_3 grown via molecular beam epitaxy on a sapphire substrate by our collaborators at Penn State University lead by Anthony Richardella. Next, 30nm of niobium is sputtered on top of the Bi_2Se_3 by Reza Loloee at Michigan State University. This puts the device in the initial condition shown in Figure 6.5. The rest of the device fabrication is carried out in the Tessmer group. Two primary techniques are necessary to pattern the Nb into an array of fingers. The first is electron-beam lithography (EBL) and the second is reactive ion etching (RIE).

EBL begins with spin-coating e-beam resist onto the sample. Resist is a liquid, organic material designed such that its chemical and physical properties change after exposure to a beam of electrons. Because resist is a viscous liquid at room temperature, it can be evenly coated over the sample by spinning at a high rate (3000 rpm). The procedure begins by covering the resist spinner area with a disposable layer of aluminum foil. Resist is often hazardous, so it's important that all materials are properly collected and disposed of when the procedure is complete. A puck is chosen such that it is

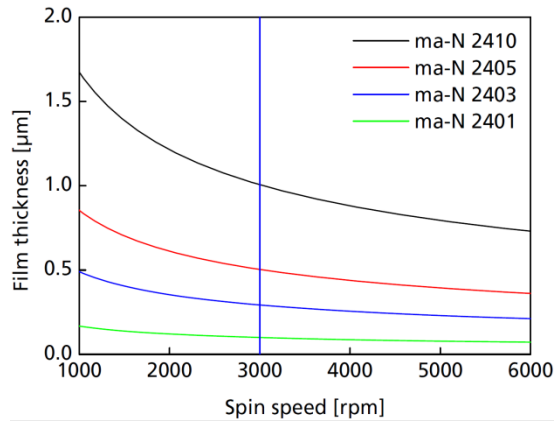


Figure 6.4 Film thicknesses for various negative e-beam resists. The spin time is 30s for all curves. The thickness of maN-2401 after 30s at 3000 rpm is 0.1 μm . Adapted from Ref TBD.

slightly smaller than the sample. It must be smaller so that the vacuum suction effectively adheres the sample to the puck. The sample is placed on the center of the puck, and the spinner is started by pressing a pedal. If the sample is not properly placed on the puck, the spinner does not start. Once the sample is spinning, the rotation speed and time can be chosen. For this procedure, we use 3000 rpm for 30s. The final thickness of the resist layer depends on the rotational speed and the time, as seen in the rotation curve in Figure 6.4. Once the speed and time are set, the spinner is stopped so that the resist can be dispensed onto the sample via pipette. This procedure uses MaN-2401 negative e-beam resist. To ensure the highest resist quality, the resist is pulled from the middle of its container, not the top or bottom of the liquid level. Resist is dispensed in a small drop in the center of the sample and the spinner is started up again. This small drop of liquid will spread into a thin layer by the centrifugal force of the spinner. Once the spinning is complete, the sample is brought over to a hotplate pre-heated to 90°C. The sample bakes on the hotplate for 60s. This solidifies the resist, leaving the sample in the state shown at the bottom of Figure 6.5.

The next step is the most critical for creating a high-quality device. Now that the resist has baked, it needs to be patterned with the e-beam. The e-beam used in this procedure is an SU5000 Schottky Field Emission Scanning Electron Microscope by Hitachi. Scanning electron microscopy (SEM) is a microscopy technique that focuses a beam of electrons at a material. Field emission electrons

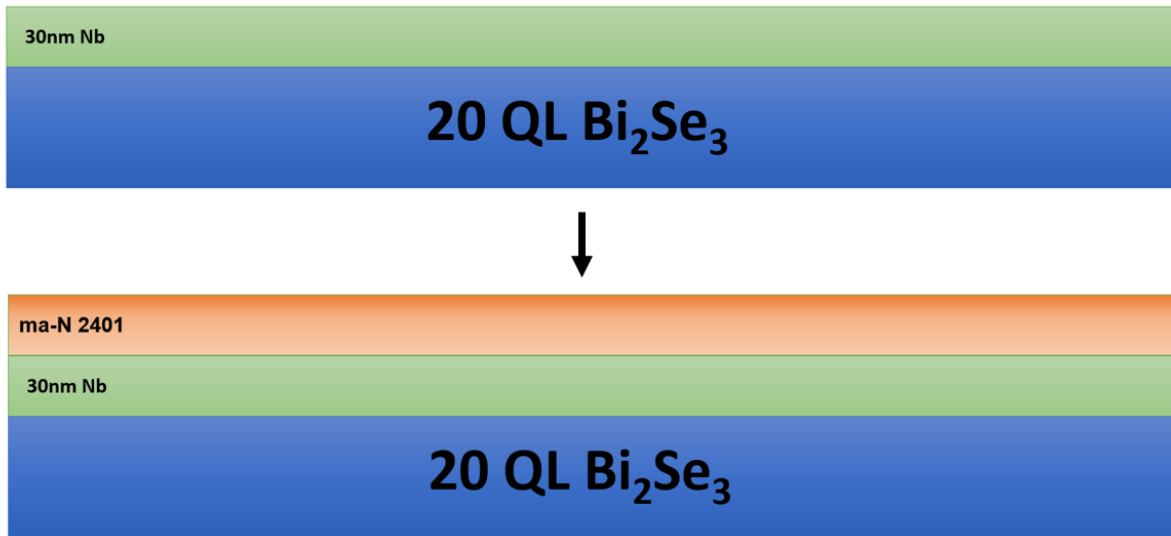


Figure 6.5 (Top) This is the condition of the device when I begin my portion of the device fabrication process. This is 20 QL of Bi₂Se₃ grown via molecular beam epitaxy with 30 nm of sputtered Nb mounted on a sapphire substrate. (Bottom) This is the condition of the device after spin-coating with resist. ma-N 2401 is a negative e-beam resist. Negative resist remains on the sample after patterning and developing. The role of the resist is to protect portions of the Nb during etching.

from the material are collected and used to create an image of the surface. In analogy with optical microscopes, the beam needs to be focused on the plane of the material, and astigmatism needs to be corrected [34]. To get the microscope to focus at the correct depth of field, it's helpful to find an imperfection on the surface of the sample such as a dust particle. This enables the user to see how well-resolved the image of the particle is, especially if the particle is irregularly-shaped. The smaller the particle, the better. It's obvious when the edge of the particle become sharper. If the image of the particle moves laterally across the screen, then that means there is astigmatism to correct. There is an astigmatism correction mode in the software that will move the focal plane in and out. This makes it clear on which axes the astigmatism needs to be corrected. There are control knobs that the user can use to adjust as needed, one axis at a time until the image is steady on the screen. Ideally, the image should just oscillate between being sharply-defined and blurry without moving laterally while in the astigmatism correction mode. It's important that the user performs these operations quickly, as the SEM is constantly exposing the resist while it is producing images.

After the image is focused, it's time to write the pattern. The software uses two user-created files for the writing process: the design file and the run file. The design file is created in Design CAD (Computer Automated Design) or Auto CAD and converted to the Design CAD file type (.dc2.) This design file tells the software the dimensions of the pattern in μm . For this device, that means there are parallel fingers $50\mu m$ long, $0.5\mu m$ wide, and separated by a $0.3\mu m$ gap. The run file tells the software the array size, the charge dosage, the dwell time, the spot size for the beam, and the magnification. All of these parameters affect the quality of the final device.

Determining the correct charge dosage requires trial and error. The first sample we received from the PSU collaborators was used for a dosage test. This means that I set a run file with a 2×5 array of 10 different dosages, ran through the full device fabrication procedure on it, and characterized the final pattern with atomic force microscopy (AFM) to see which dosage would produce the best patterns. The device characterization process will be described in more detail later in this Section. This dosage test procedure showed that $80\mu C/cm^2$ was the ideal charge dose for these devices. Next, the spot size is chosen such that the dwell time is greater than $1\mu s$ so that the uncertainty in dwell time does not greatly impact the dosage. The spot size, charge dose, and dwell time are related by $D = \frac{It}{\pi s^2}$ where D is the dose, t is the dwell time, s is the spot size, and I is the beam current. The beam current is fixed at $65pA$, so a spot size of $6nm$ gives the correct dose at a viable dwell time. This spot size provides better resolution than necessary to create the desired pattern which has features on the scale of 100s of nanometers. The pattern is written as a 20×20 array of $50 \times 50 \mu m$ array elements separated by a $10 \mu m$ buffer region creating a $1.2 \times 1.2 mm$ area with 70% coverage. This is sufficient to overcome the needle-in-a-haystack problem. It takes over four hours to finish writing.

After the pattern has finished writing, it is time for it to be developed. This is a very quick and simple process. The sample is submerged in AZ-MIF 300 developer for 10 seconds. Next, it is rinsed with deionized (DI) water for 30 seconds and blown dry with N_2 gas to remove any water spots. The resist that was exposed with the e-beam will be insoluble in the developer while the

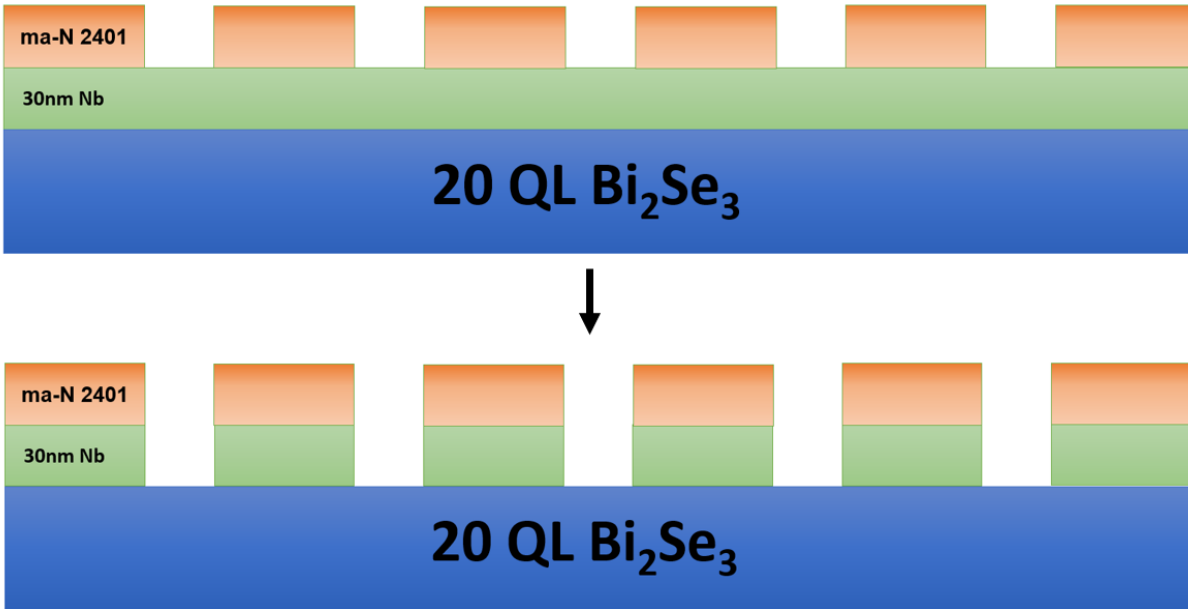


Figure 6.6 (Top) This is the state of the device after patterning and developing. The resist that was exposed by the e-beam during patterning is insoluble, so it remains on the surface of the sample. (Bottom) This is the state of the device after RIE. The resist protects the Nb during etching leaving the Nb patterned into the desired geometry.

resist that was not exposed is washed away. Now the sample is in the state shown at the top of Figure 6.6. No changes have actually been made in the materials that comprise the device, all that has happened is the resist has been shaped into the desired pattern.

The next step is reactive ion etching (RIE) to etch away the Nb that is not protected by the resist. This process utilizes a plasma of highly reactive gas to remove material. Because this process involves chemical reactions, there are several drawbacks to take into account. First, the process can be slightly inconsistent between different devices based on what compounds are left over in the chamber. This can be mitigated by first running an etching process on the empty chamber before loading the sample. The other drawback is that the plasma could etch the underlying material, Bi₂Se₃, and chemically alter the surface. To avoid this, the etching time is a crucial parameter to control. The etching rate is non-linear. It begins slowly and increases in speed, as shown in Figure 6.7. This means that after the Nb has been etched, there is some delay before the Bi₂Se₃

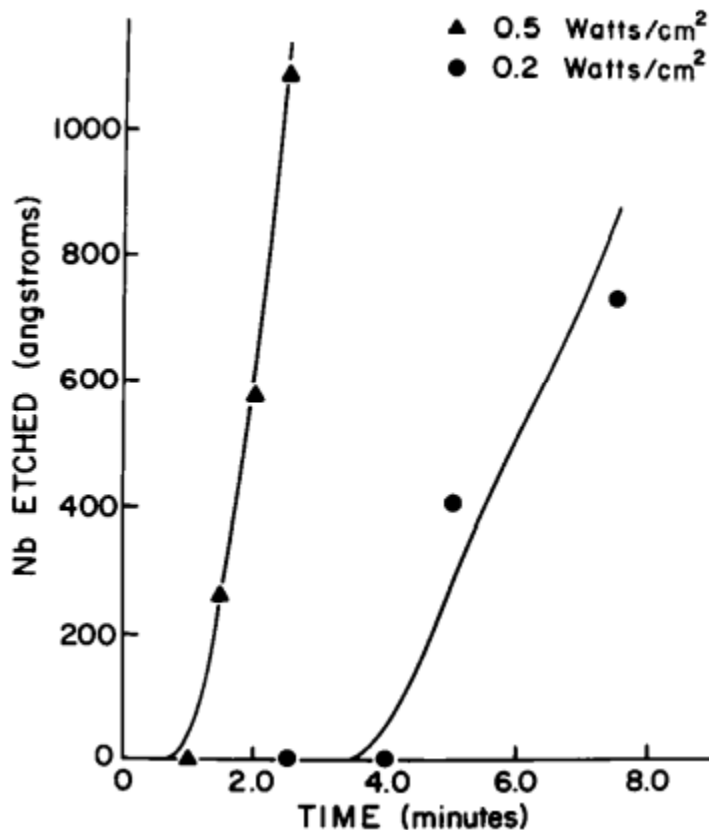


Figure 6.7 Amount of Nb etched as a function of time. This process used CBrF_3 plasma instead of CF_4 . It's clear that there is a delay before the etching process takes off. The parameters of the RIE should be selected such that the Nb is quickly etched away after the delay. This makes it easier to terminate the process before the plasma begins to etch the Bi_2Se_3 . Adapted from Ref [1].

undergoes significant etching. To estimate the time necessary to etch through the niobium, 30nm of niobium are first sputtered onto glass substrates. The RIE apparatus has a camera mounted in the vacuum chamber, so it's possible to observe the etching in real time with a fully transparent substrate. This is not typically possible with Nb grown on Bi_2Se_3 as both materials have too similar of an appearance to tell apart through the camera. On the transparent glass substrate, however, when the niobium is etched, it appears as if the sample is fading away over time. Using this method, I determined that it takes approximately 80s for the niobium to be fully etched. For the process to create devices, I use 90s to ensure there is no niobium left over in the spaces between fingers.

There are other crucial parameters for the RIE process. These include: the power used to create the plasma, the choice of gas, the pressure of the gas during etching, and the base pressure before etching. Tuning these parameters involves a great deal of trial and error. First, the gas selected needs to be reactive with the material to be etched. For niobium, I chose CF_4 . The power of the RIE plasma and the pressure of the gas during etching affect the etching time of the niobium. If the etching happens too quickly, then the uncertainty in the etching time will cause large variations from run-to-run. Otherwise, if the etching rate is too slow, then the uncertainty in the etching time will mean that it's likely that the Bi_2Se_3 has begun etching long enough for its etching rate to increase. It's ideal for the etching to finish just after the rate of etching increases. This means that when doing tests of niobium on glass substrates, I wanted to see the niobium totally disappear quickly after the etching became noticeable. The parameters that achieved this goal were an RIE power of 150 W and a pressure during etching of 100 mTorr. For consistent results run-to-run the base pressure before etching should be as low as is practical. During my time with the machine, there were many problems with its ability to reliably pump to low base pressures. Ultimately, I settled for any base pressure lower than 10^{-4} torr. After the devices have been etched, they are in the state shown at the bottom of Figure 6.6.

There is only one step left to create a finished device: remove the resist. E-beam resist is an insulating material, so leaving the resist on the finger would be unworkable for an STM experiment. The STM feedback would push the tip into the resist while trying to reach the tunneling current set point, ruining the tip. While it's important to remove the resist, it's also important that the device remains intact. In several attempts to remove the resist, I would use an ultra-sonic bath to agitate the sample and increase the rate that resist dissolved, or I would heat up the sample and solvent. These methods would frequently cause the Bi_2Se_3 to lift off of the substrate. Bi_2Se_3 is a difficult material to work with in this context due to its layered structure. The most reliable method was to simply let the device soak in Remover PG for 45 minutes, soak in IPA for 30 seconds, soak in DI water for 30 seconds, then blow dry. This method consistently removed all of the resist without



Figure 6.8 The completed device after removing the remaining e-beam resist.

agitating the Bi₂Se₃. Once the resist has been removed, the device is in the state shown in Figure 6.8 which is the same as the experimental plan shown in Figure 6.3.

Developing this recipe for the devices required testing a new set of parameters at a variety of stages in the fabrication process. To understand how the final devices were affected by these parameters, I needed to take a look at the surface topography. STM experiments require a significant time commitment in cutting tips, testing tips, and aligning the samples, as explained in Chapter 3. This makes STM an unsuitable tool for quick and easy device characterization in the testing process. The Cypher atomic force microscope (AFM) was the ideal tool for this task. AFM is yet another scanning probe microscopy technique. It utilizes a hard, sharp tip at the end of a flexible cantilever. The cantilever and tip act as a damped, driven harmonic oscillator. Oscillations are driven into the cantilever while the amplitude of these oscillations is measured by laser light reflected onto a photodiode. This microscope operates by bringing the tip into contact with the surface of the sample. Contact with the sample causes the amplitude of the oscillations to diminish. Next, the tip is scanned across the surface of the sample while keeping the amplitude constant. This is similar to how an STM takes topography with the primary difference being that it's the oscillation amplitude that's kept constant and not the tunneling current. AFM also uses piezoelectrics for the fine manipulation of the tip and sample, another similarity to STM.

AFM operation begins with adhering the sample to a metal disc with double-sided tape. The metal disc is held in place with magnets and moved laterally with piezoelectrics. Next, the tip is selected and carefully loaded into place with tweezers. The cantilever and tip are small and easily

broken, so care must be taken to only hold it from the sides and not allow the cantilever to brush against anything while loading. This is also important to keep in mind while moving the sample after the tip is in place. To preserve the tips, it's wise to move the tip at least 0.5 mm away from the sample before moving the sample.

After the tip is loaded, the tip is manually brought within 1 mm of the surface. All tasks can now be completed in the software. Next, I need to look for the tip on the optical microscope and bring it into focus and then bring the sample into focus. By setting the focus on the tip and sample, the software knows how far to move the tip to bring it close to the sample. Using the optical microscope while focusing on the sample, it's easy to find the large pattern and move the sample such that it is underneath the tip. Now, the tip is brought into "pre-engage" position above the sample (0.05 mm above the sample.) The optical microscope also controls the position of the laser, so with the focus set to the tip, the microscope is moved such that the bright, red spot of the laser can be seen hitting the cantilever. Once this is done, I zero the photodiode. The photodiode has to be zero'd periodically after shifts in the tip or sample position.

Next, it's necessary to auto tune the driving frequency to the resonant frequency of the tip. The software will vary the driving frequency while measuring the amplitude and phase until it finds a driving frequency that maximizes the amplitude and has a phase relationship like that shown in Figure 6.9. If the software fails to find a resonant frequency, I narrow the search space to a more narrow band about the manufacturer's suggested resonant frequency for the tip. Now the tip is ready to be used for tapping mode AFM. The tip is brought into contact with the surface and topography is acquired. If there is an error message during approach, it can typically be resolved by lowering the set amplitude. By default, the set amplitude is 80% of the amplitude in open air. A set amplitude of 60% will cause greater wear and tear on the tip but improve image quality and resolve most approach errors.

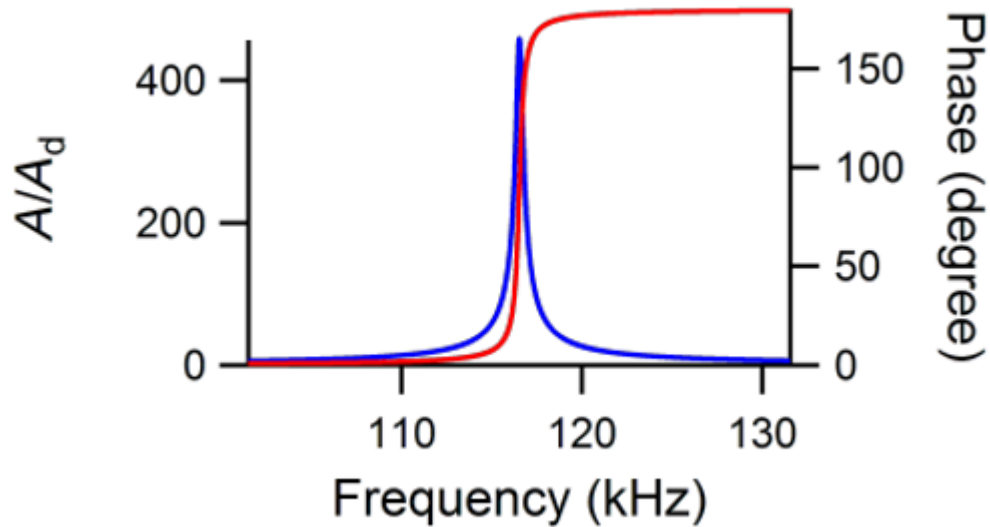


Figure 6.9 An example of ideal amplitude and phase response as a function of driving frequency. The amplitude should peak at the resonant frequency while the phase resembles a sigmoid function. Adapted from Ref [40].

To characterize a device array, I start with a $20 \times 20 \mu\text{m}$ scan range. This lets me see if the pattern is consistent on a large scale. Next, I go to the edge of the array element and do a $3 \times 3 \mu\text{m}$ scan. The smaller range scan is more detailed, showing the spaces between the fingers. It's important that the fingers are well-separated with no niobium spanning the gaps between them. If the fingers are 30 nm tall, and the space between the fingers is the same height as the buffer region between array elements, then the array element is suitable for the experiment. This process is repeated for each array element in the four corners of the array. That way, we can be confident that the device will be of high quality everywhere we may randomly land during the STM experiment. Figure 6.10 shows how the line junctions are arranged into an array.

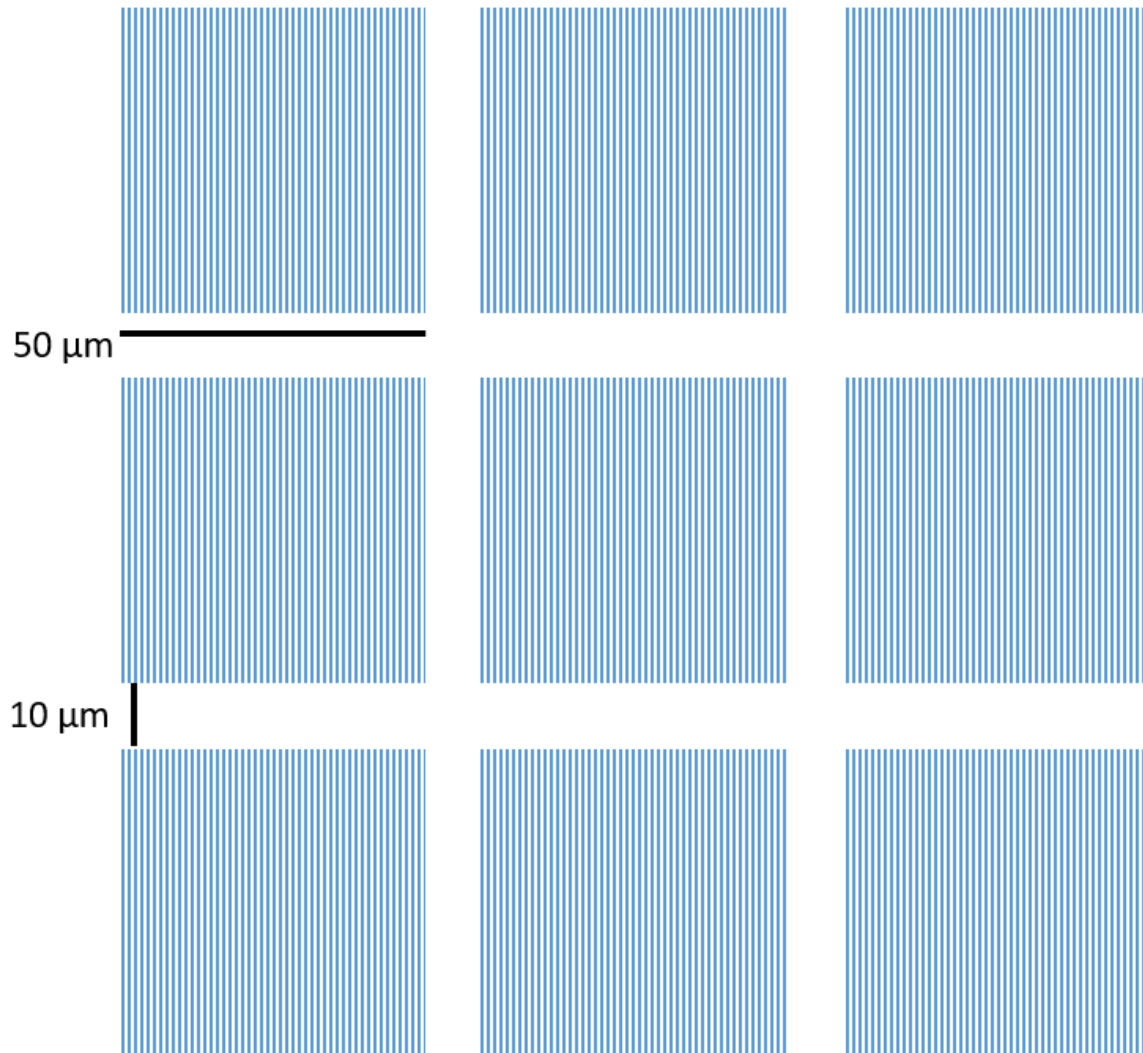


Figure 6.10 A diagram of a 3 x 3 array of line junction array elements. Arrays used for the experiment are 20 x 20. The array elements are 50 x 50 μm with a 10 μm buffer region between them. The buffer region is simply Bi_2Se_3 with no Nb on top.

6.3 Theoretical Calculations

During the COVID-19 pandemic, we were unable to perform lab experiments for several months due to the public-health shutdowns. This coincided with when we were ready to begin work on the experiment described in this chapter. I used the time during the shutdown to learn the Kwant Python package [10] and use it to simulate my experiment. This powerful package can efficiently solve tight-binding Hamiltonian eigenvalue problems, calculate transport properties, calculate energy as a function of crystal momentum in periodic systems, and approximate the value of the density operator in a lattice. In this section, I will explain the calculation and present the simulation results. The full code can be found in the CMPTessmer group drive. We were interested in understanding what the tunneling conductance measurements would look like in a S-TI-S junction. To do this, I translated the Hamiltonian in ref [8], i.e. Equation 6.2 into a tight-binding Hamiltonian, spatially varied the phase, ϕ , and used the kernel polynomial method (KPM) to calculate the expectation value of the density operator on the lattice.

For simplicity, we will only be discussing tight-binding Hamiltonians with nearest-neighbor hopping. These Hamiltonians are comprised of two primary terms (ignoring hermitian conjugates): onsite potential, H_{onsite} and hopping amplitude, H_{hop} . The onsite potential represents the energy of an electron bound to site i , eigenstate $|i\rangle$. Hopping amplitude represents the energy gained or lost when the electron moves from site i to site $i + 1$. In bra-ket notation a generic 1-dimensional tight-binding Hamiltonian with N sites can be written as:

$$H = \sum_{i=1}^N H_{onsite} |i\rangle \langle i| + H_{hop} |i+1\rangle \langle i| + h.c.. \quad (6.5)$$

This Hamiltonian can be represented by a sparse $N \times N$ matrix. The H_{onsite} terms occupy the main diagonal of the matrix and H_{hop} are one space off-diagonal. In the case where there are m orbitals, H_{onsite} and H_{hop} can be represented with $m \times m$ matrices, and H would be an $Nm \times Nm$ dimensional matrix. Now H_{onsite} terms still occupy the main diagonal as $m \times m$ block matrices, and H_{hop} terms similarly are one $m \times m$ block off-diagonal.

Continuous Hamiltonians can be transformed into tight-binding Hamiltonians with some simple prescriptions. Consider the generic two-dimensional Hamiltonian with kinetic and potential energy:

$$H = \frac{-\hbar^2}{2m}(\partial_x^2 + \partial_y^2) + V(x, y) \quad (6.6)$$

This Hamiltonian is defined everywhere in the 2D plane with arbitrary accuracy with the position coordinates x and y . Transforming to a tight-binding model loses the arbitrary precision of the coordinates and instead moves to a lattice defined as:

$$|i, j\rangle \equiv |ai, aj\rangle = |x, y\rangle. \quad (6.7)$$

The variable a is the lattice spacing. One-to-one correspondence is achieved in the limit as $a \rightarrow 0$. Similarly, the derivatives can only be defined in this limit with a finite-difference approximation. First and second derivatives, respectively, transform like so:

$$\partial_x = \lim_{a \rightarrow 0} \frac{1}{a} \sum_{i,j} |i+1, j\rangle \langle i, j| + |i, j\rangle \langle i+1, j| \quad (6.8)$$

$$\partial_x^2 = \lim_{a \rightarrow 0} \frac{1}{a^2} \sum_{i,j} |i+1, j\rangle \langle i, j| + |i, j\rangle \langle i+1, j| - 2|i, j\rangle \langle i, j| \quad (6.9)$$

The first derivative is approximated as a hopping amplitude, and the second derivative includes both a hopping amplitude and onsite correction. Applying this prescription to the generic Hamiltonian in Equation 6.6 results in:

$$H = \sum_{i,j} (V(ai, aj) + 4t) |i, j\rangle \langle i, j| - t |i+1, j\rangle \langle i, j| - t |i, j+1\rangle \langle i, j| \quad (6.10)$$

With t defined as $t = \frac{\hbar^2}{2a^2m}$.

Implementing this Hamiltonian in Kwant is a straightforward exercise outlined in the documentation for the package [10]. First, the lattice needs to be created along with a system object:

```
lat = kwant.lattice.square(a)
syst = kwant.Builder()
```

Next, onsite and hopping terms can be defined as functions that take in the lattice position as an input.

```
def onsite(site, t):  
    return 4*t  
  
def hopping(site1, site2, t):  
    return -t
```

These functions can be applied to the system by looping over the lattice sites and using the built-in neighbors function.

```
syst[(lat(x,y) for x in range(L) for y in range(W))] = onsite  
syst[lat.neighbors()] = hopping
```

This will create a square lattice system L units long and W units wide. The onsite potential is 4t everywhere with nearest-neighbor hopping -t. Calculating transport through this system requires attaching leads to it. To keep things simple, I will attach normal metal leads using more Kwant built-in functions.

```
lead = kwant.Builder(kwant.TranslationalSymmetry((-a, 0)))  
lead[(lat(0,j) for j in range(W))] = onsite  
lead[lat.neighbors()] = hopping  
syst = syst.finalized()
```

Transport through the wire means calculating the transmission component of the scattering matrix. Kwant, of course, has a built-in function for this, as well. The only inputs it requires are the parameters, which, as a best practice are stored in a Python dictionary, the energy eigenvalues, and the system. This data can then be stored in an array and plotted using matplotlib, as shown in Figure 6.11.

```
params = dict(t=t)  
smatrix = kwant.smatrix(syst, energy, params=params)
```

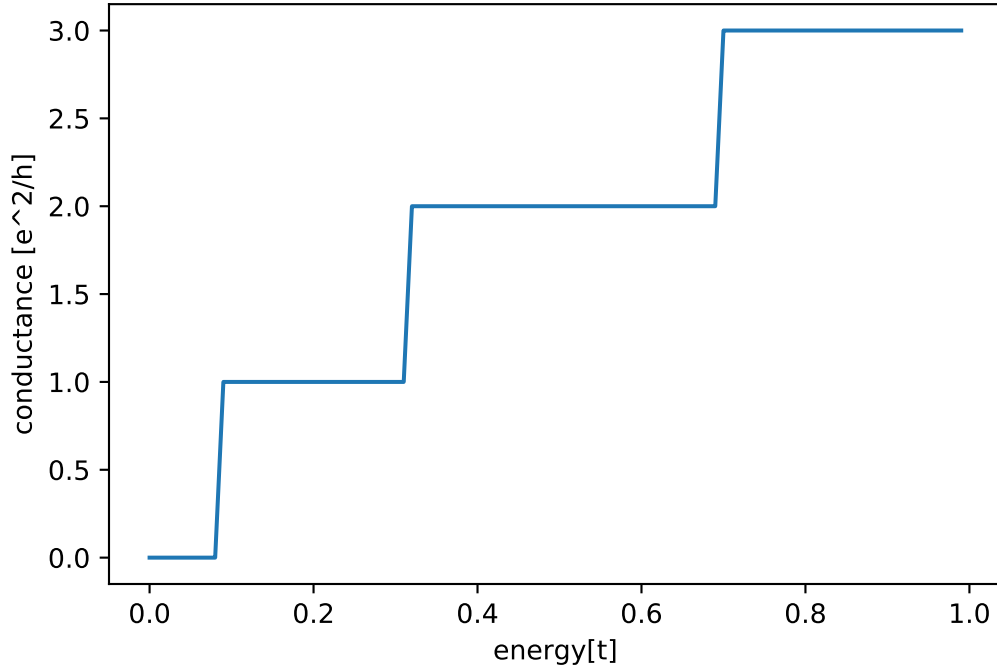


Figure 6.11 A plot of conductance in units of conductance quanta as a function of energy in units of $t = \frac{\hbar^2}{2a^2m}$. The system is a quantum wire, and the plot shows the expected quantized conductance steps.

```
data.append(smatrix.transmission(1,0))
```

Applying this prescription to Equation 6.2 proceeds similarly with a few key differences. The first difference is that Equation 6.2 only includes first derivatives. The other difference is that Equation 6.2 has spin and particle-hole degrees of freedom. These two degrees of freedom are separated into two 2 x 2 block matrices that make up the 4 x 4 matrix orbital degrees of freedom in the tight-binding model. The 2 x 2 matrices are cast into the 4 x 4 form with ordered Kronecker products.

$$H = -iv(\sigma_x \partial_x + \sigma_y \partial_y) \otimes \tau_z - \mu \mathbb{1} \otimes \tau_z + \Delta_0(\mathbb{1} \otimes \tau_x \cos \phi - \mathbb{1} \otimes \tau_y \sin \phi) + B(\sigma_z \otimes \mathbb{1}) \quad (6.11)$$

Here I am using τ_i for Pauli matrices acting on the particle-hole degrees of freedom and σ_i for Pauli matrices acting on the spin degree of freedom, but in the code these matrices are identical. The

only distinction between the degrees of freedom is in the ordering of the Kronecker products. I have also included a Zeeman term, as the experiment will include an external magnetic field. With this out of the way, the translation to a tight-binding Hamiltonian is straightforward. The terms containing x-derivatives are assigned as x-hopping amplitudes, the terms containing y-derivatives are assigned as y-hopping amplitudes, and the terms with no derivatives are the onsite potentials. The superconducting phase, ϕ , varies from 0 to 2π along the y-axis in the left half of the system. In the right half of the system $\phi = 0$.

```
def JJ_onsite(site, mu, delta, phi, B, A, L, W):
    (x, y) = site.pos
    normal = - mu*np.kron(s0, sz) + B*np.kron(sz, s0)
    if x > 0:
        gap = delta*(np.cos(A*np.pi*y/W + phi)*np.kron(s0, sx) +
                    np.sin(A*np.pi*y/W + phi)*np.kron(s0, sy))
    else:
        gap = delta*np.kron(s0, sx)
    return normal + gap

def JJ_xhop(site1, site2, v):
    return -1j*v*np.kron(sx, sz)

def JJ_yhop(site1, site2, v):
    return -1j*v*np.kron(sy, sz)
```

Numpy (np) is used for math operations and manipulation of array objects. s_0 , s_x , s_y , and s_z are, respectively $\mathbb{1}$, σ_x , σ_y , σ_z . The np.kron() function is the Kronecker product. With the system built, all that is left is to calculate the local density of states. Kwant has built-in methods for defining the density operator and for calculating the density map using a KPM. Adding moments and vectors increases the accuracy of the KPM at the expense of using more computer resources.

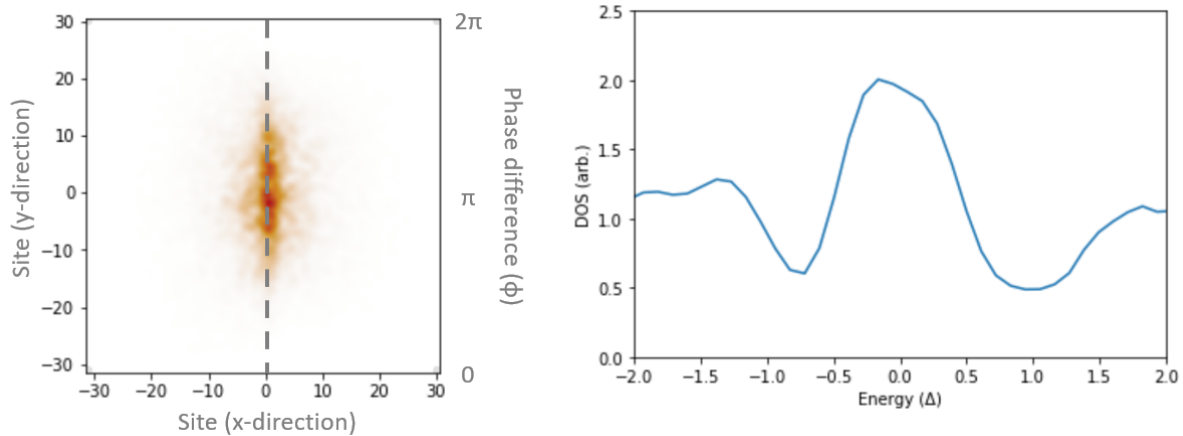


Figure 6.12 (Left) An electron density map at zero energy over sites in a tight-binding model using Equation 6.11 with a spatially varying phase. The density map was calculated in the Kwant Python package using a kernel polynomial method (KPM). There is noise in the calculation due to the fact that the KPM uses random vectors. The system is divided into two regions. For sites with $x < 0$ the phase is set to $\phi = 0$. Sites with $x > 0$ have phase $\phi = y2\pi/W + \pi$ where $W = 60$ is the width of the system. This means that the phase difference varies linearly along the width of the system from 0 to 2π . The phase offset is chosen such that $\phi = \pi$ in the center of the system. We observe a bright region in the junction where $\phi = \pi$, indicating enhanced density of states at zero energy. (Right) A plot of the density of states as a function of energy in units of the superconducting gap Δ . This plot was taken by averaging together the contributions of the 5 central sites from the map on the left. We see that there is a peak in the DOS at zero energy. This is the expected experimental signature in future studies on these system.

```

density_op = kwant.operator.Density(syst)
local_dos = kwant.kpm.SpectralDensity(syst, params=params, operator=density_op)
local_dos.add_moments(100)
local_dos.add_vectors(5)

```

Figure 6.12 shows the resulting density map in a line junction geometry. Figure 6.13 shows the resulting density map in a tri-junction geometry. The tri-junction geometry was a test of the code to see if it could reproduce a result in Ref [8], and it was successful. With the phases tuned to the gray region in Figure 6.1(d) a zero energy state appears in the tri-junction.

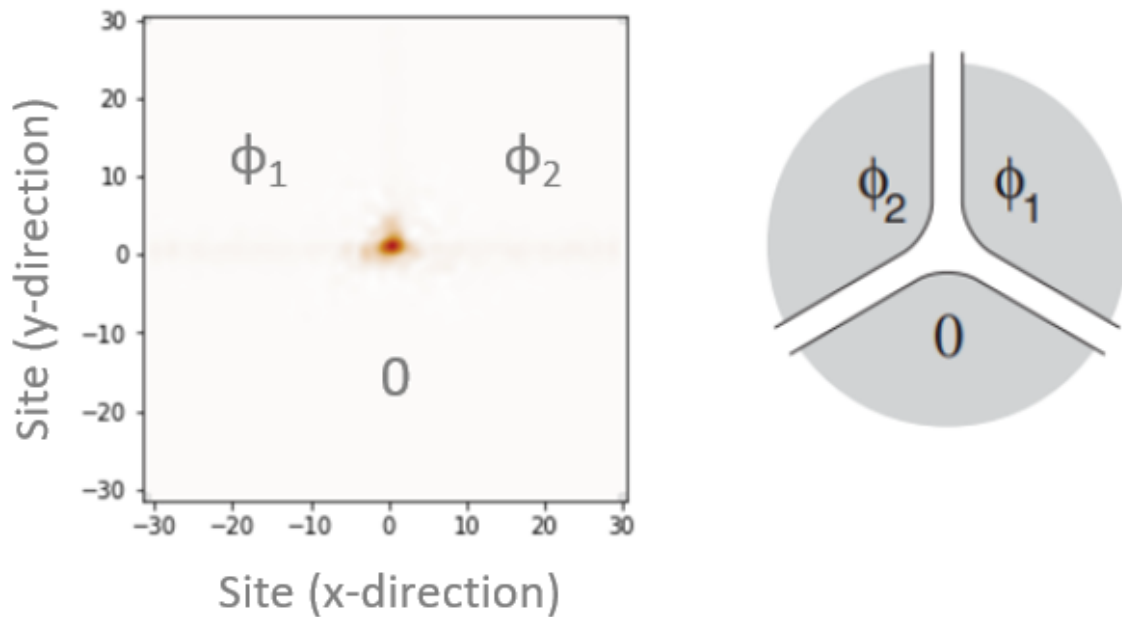


Figure 6.13 (Left) An electron density map at zero energy over sites in a tight-binding model using Equation 6.11 with a spatially varying phase. The density map was calculated in the Kwant Python package using a kernel polynomial method. The system is divided into three regions with three different superconducting phases. All sites with $y < 0$ have $\phi = 0$, sites with $y > 0$ and $x < 0$ have $\phi = \phi_1 = \pi/2$, and sites with $y > 0$ and $x > 0$ have $\phi = \phi_2 = 3\pi/2$. This puts the junction into the shaded region of phase space shown in Figure 6.1(d) that corresponds to the topological state. We observe a bright spot in the junction when the phases are tuned to lie in this region, indicating enhanced density of states at zero energy. (Right) Tri-junction diagram adapted from [8].

CHAPTER 7

JOSEPHSON VORTEX RESULTS

This chapter shares the device fabrication and STM measurement results for the Josephson vortex experiment. Early iterations of the devices had inconsistent geometries that were generally unsuitable for STM study. Issues with the device fabrication process were eventually overcome and now devices can be consistently made with high quality junctions over wide ranges. Tapping mode atomic force microscopy (AFM) topography demonstrates the quality of the junctions. For STM experiments to be successful, the array elements need to be consistent across the array. STM experiments demonstrate the viability of the Josephson vortex experiment by successfully topographically imaging Nb fingers at low temperature and showing clear evidence of superconductivity.

7.1 Device Fabrication Results

Using the methods outlined in Section 6.2, I fabricated dozens of S-TI-S Josephson junction devices. Early attempts at the devices were used to help tune the parameters. Many of the fabrication steps require trial and error to get the process working for these materials. There are several ways that the completed device can be unsuitable for experiments. The most common failure mode is for the pattern to be poorly-resolved. Similar to how objects in a blurry image can have their edges blend together, the same is true for e-beam lithography (EBL) processes. Imperfections in the focus and astigmatism settings cause the edges of the pattern to blur together. This causes a thin layer of resist to remain between the fingers after development. The resist will protect the niobium between the fingers during the etching process, leaving a device with a "webbed fingers" pattern. A U-shaped residue of niobium will remain where there should be only Bi_2Se_3 . If this residue is thin enough, the experiment could still be functional due to proximity effects. However, if the residue is thicker than 10 nm, then the device will be unsuitable for vortex experiments. This failure mode can only be overcome by choosing a good charge dose, executing the EBL procedure quickly and accurately, and etching for sufficient time. Essentially all of the parameters in the

procedure need to be dialed-in and acted on correctly.

Another failure mode is for the sample to be over-etched. In this situation, the fingers would appear thicker than their nominal 30 nm. In early iterations of the procedure, I would use 10 quintuple layers (QL) of Bi_2Se_3 rather than 20. This means that there is only approximately 10 nm of Bi_2Se_3 beneath the Nb. If AFM topography shows fingers thicker than 35 nm, then this could mean that half of the Bi_2Se_3 has been etched, ruining the topological surface states critical for the experiment and creating a trivial insulator. AFM, however, is not an ideal test for this failure mode. There is some uncertainty in the thickness of the sputtered niobium. Furthermore, from the AFM topography, alone, it's not clear if the Bi_2Se_3 has been over-etcher or if there is residual resist on the fingers making them appear thicker. This failure mode is best tested for with simple resistance measurements with a standard multimeter. Before any fabrication steps are taken, I will measure the corner-to-corner resistance of the Bi_2Se_3 . If this resistance is reproduced after the final stages of device fabrication, then I can be confident that the Bi_2Se_3 was not over-etched. Using 20 QL of Bi_2Se_3 helps, as well. Even if 10 QL were etched away, the sample would still be viable.

The final main failure mode is for the resist to not fully lift off in the last step of device fabrication. This was a fairly common occurrence before I tested much longer cleaning times. An example of topography on a device where this happened is Figure 7.1. As discussed before, it's not always clear from topography if the issue is lift-off or etching. Cases like Figure 7.1 are clearly a lift-off issue because the resist has lifted off of some fingers but not others. If the lift-off was particularly poor, the effect can be seen with an optical microscope. 30 nm Nb is almost totally transparent, so if there are any fingers that stick out starkly against the Bi_2Se_3 , then it's likely that there was a lift-off problem.

It's not sufficient for individual fingers or array elements to be high quality, as it's impossible to pick out the high quality portions of the sample during STM experiments. The devices need to be high quality over large distance scales. An example of long-range topography on an array element

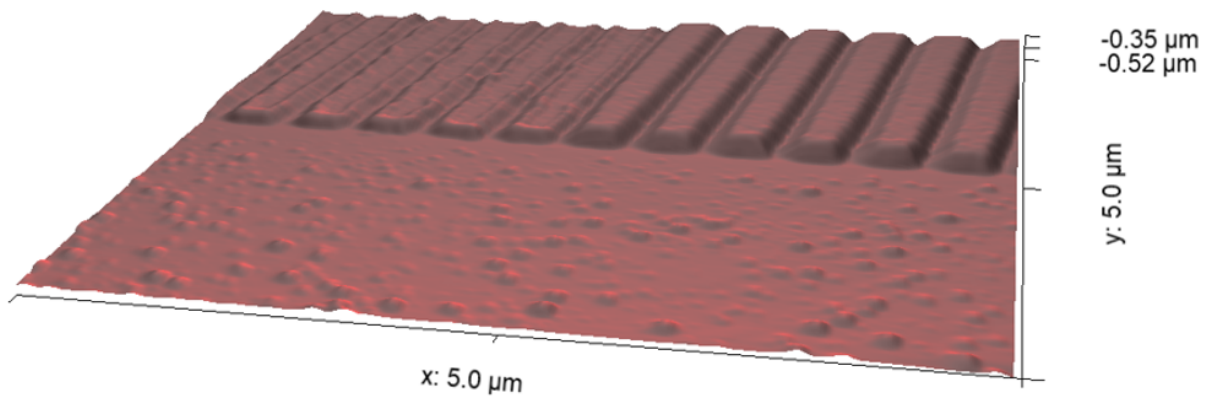


Figure 7.1 3D image of tapping mode AFM topography on an early S-TI-S device made with 30 nm of Nb sputtered on Bi_2Se_3 . The Nb is $50\ \mu\text{m}$ long, $0.35\ \mu\text{m}$ wide, spaced $0.15\ \mu\text{m}$ apart. This topography shows the edge of an array element so that the depth of the fingers can be compared with the Bi_2Se_3 buffer region. We can see that the Nb fingers have small gaps partially filled in with tapered edges. This device was made before the recipe was finalized. We can see clear evidence of leftover resist on the six fingers on the right side of the image.

is shown in Figure 7.2. With a $20 \times 20\ \mu\text{m}$ scan range, I can see that the quality of the junctions are consistent. These long range scans lack the detail necessary to determine if the Nb fingers are well-separated. To show that, I take short-range topography at the edges of the array element. In order for a device to be suitable for STM experiments, three criteria need to be met: the junctions have the correct dimensions in short-range scans with line profiles as seen in Figure 7.3, the fingers appear to be of high quality in long-range scans like Figure 7.2, and both of these criteria are met on the four corners of the array. In dozens of trials only six devices that I fabricated met all of these criteria; however, the success-rate should be higher in the future now that the recipe has been fine-tuned.

7.2 Scanning Tunneling Microscopy Results

With several viable devices prepared, it's time for STM experiments. The first step is mounting the device on an STM sample disc as shown in Figure 7.4. With the device adhered to the sample disc in this manner, it's possible to move the device laterally to aid in alignment. From specific

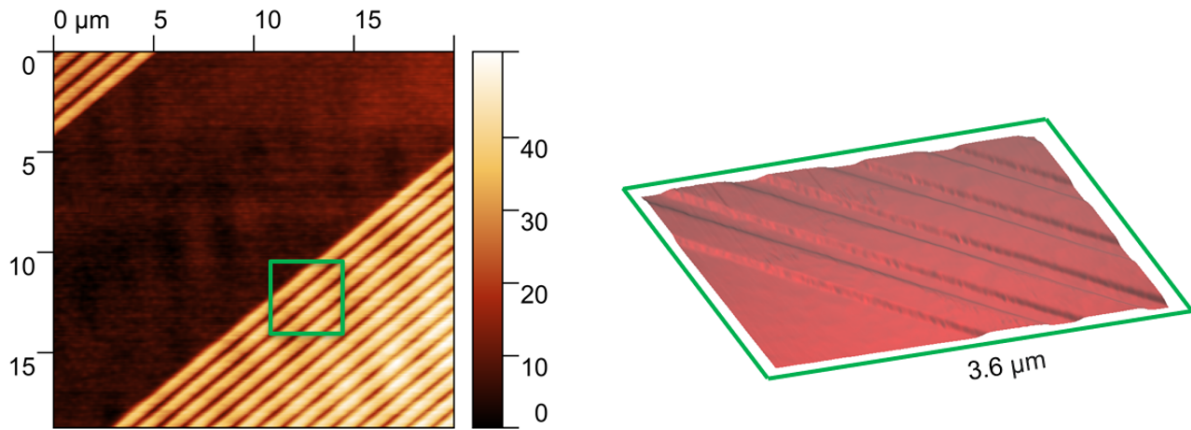


Figure 7.2 Tapping mode AFM topography on an S-TI-S device made with 30 nm of Nb sputtered on Bi_2Se_3 . The Nb is $50 \mu\text{m}$ long, $0.5 \mu\text{m}$ wide, spaced $0.3 \mu\text{m}$ apart. This device was made after the recipe was finalized. (Left) A wide-range $20 \times 20 \mu\text{m}$ scan showing the quality of the device over large distance scales. (Right) 3D image of $3.6 \times 3.6 \mu\text{m}$ topography taken from the region highlighted in green. Small-range topography is necessary to get detailed images of the junctions. The fingers are fully separated, and the height of the topography in the junctions is the same as the buffer region, indicating that the Nb in the junctions fully etched.

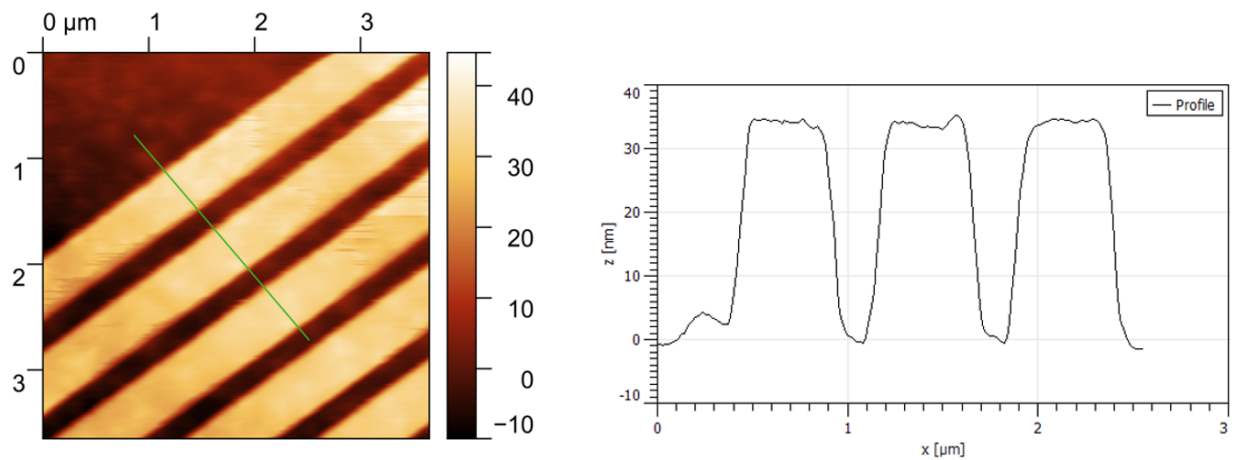


Figure 7.3 (Left) Short-range AFM topography on the highlighted region in Figure 7.2. This image was corrected with a standard 3-point flattening procedure and polynomial background correction. (Right) The height profile along the green line in the topography image. The Nb is $30 \pm 1 \text{ nm}$ tall. This indicates that virtually no Bi_2Se_3 was etched.

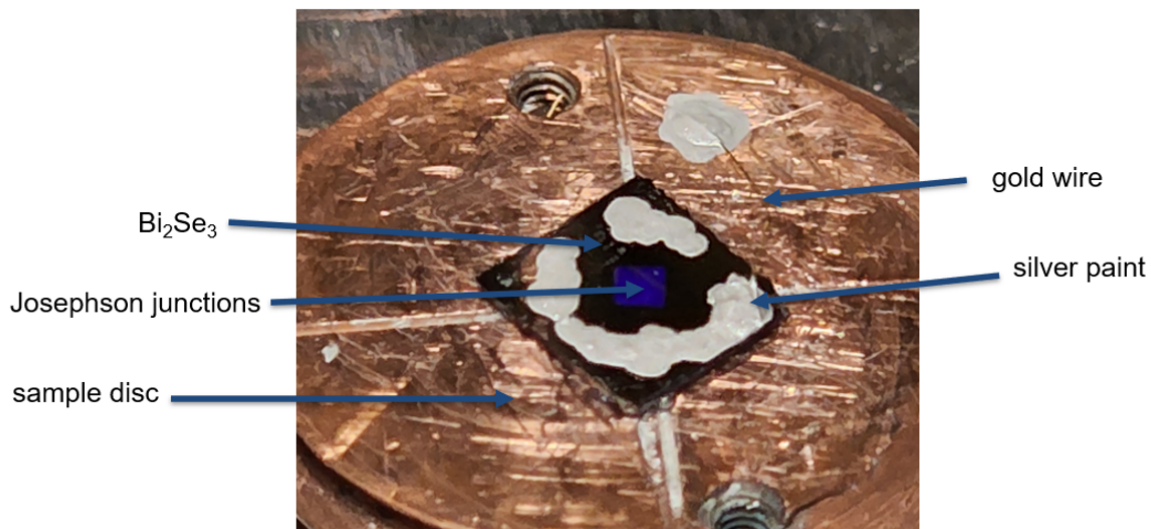


Figure 7.4 A completed device mounted on an STM sample disc. This device is adhered to the sample disc with vacuum grease, so we can move the device laterally when aligning the STM tip. The device is on an insulating sapphire substrate, so there needs to be a conducting path from the surface of the device to the sample disc. This is accomplished with a gold wire silver painted to the sample disc and the device. The 1.2 x 1.2 mm array of junctions is visible to the naked eye from certain angles. It's almost impossible to see the junctions after the sample disc is loaded in the microscope, so I used silver paint to frame the array.

angles, it's possible to see the array with the naked eye while the sample is on the benchtop; however, it's virtually impossible to see the array after it's been loaded into the microscope, as shown in Figure 7.5. The array is framed with silver paint to help with alignment.

Aligning the tip with the region of interest is accomplished through trial and error. The procedure begins with mounting the microscope on the glove box, a suitably stable platform for room temperature topography. This glove box is overpressured with N₂ gas (the Bi₂Se₃ used for these experiments has few vacancies, so the N₂ exposure effect is irrelevant) to avoid surface contamination while testing. The glove box has the advantages of being a more stable and controlled environment, but it has the disadvantage of forcing me to look at the tip and sample from a distance during alignment. To overcome this, a quick fix was to use my phone's camera to zoom in on the tip and sample. I compared photos of my tip and sample, like that in Figure 7.5, and photos of the

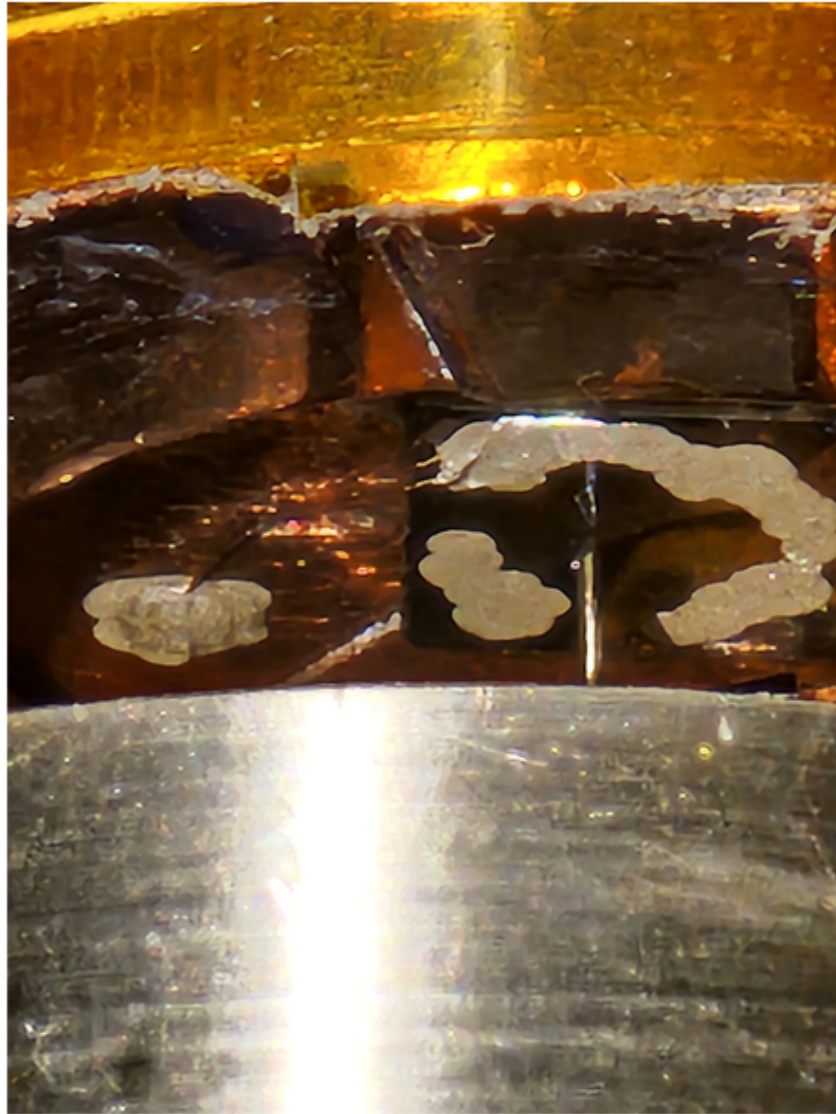


Figure 7.5 A photo taken with a Samsung Galaxy S22 Ultra at 100x zoom of a completed device loaded into the STM. The array is invisible to the naked eye, but the silver paint provides land marks to guide me during alignment. It's ideal for the device to be properly aligned while the sample disc is in the full +Y direction, so that during low temperature experiments, there is a simple prescription to find the area of interest.

sample on the tabletop, like Figure 7.4 to align the tip and sample.

Once the tip and sample are visually aligned, the next step is to take topography. With a topography range of $1 \times 1 \mu\text{m}$, two fingers can fit in a single scan window, as shown in Figure 7.6. This is a clear signal that the tip and sample are correctly aligned. If the topography is flat

and featureless, then it's possible that the tip landed in a buffer region. For that reason, several topographical images were acquired in nearby locations before changing the alignment. If several topography scans do not show evidence of the pattern, it's likely that the tip and sample are incorrectly aligned, so the sample is then repositioned. This process is repeated until the pattern is found consistently at room temperature. At low temperature there is no visual indication of where the sample disc is within its lateral coarse positioning range, and the tip and sample disc will not be in the same alignment after they are lowered into the cryostat. To increase the odds of finding the region of interest at low temperatures, I can walk the sample disc using the piezo-tubes it's resting on in the +Y direction for several minutes. Room temperature tests with reduced piezo voltage amplitude inform how long this walking is likely to take. Choosing a maximal position means that it's impossible to overshoot, so at low temperature I simply have to let the sample disc walk for several times longer than the room temperature tests indicated. In previous attempts, I did not mount the device on the sample disc with the vacuum grease trick, making it highly unlikely that the region of interest could be reached at the maximum +Y position. This led to low temperature data runs that would go on for days without clear topographic evidence that the tip was in the region of interest.

With the tip and sample aligned, the low temperature phase of the experiment is ready to begin. The cryostat chambers are pumped out according to the procedures outlined in Chapter 3. This experiment relies on the superconducting properties of Nb which has a T_C of 9.25 K, so the cryostat is cooled with liquid helium to 4.2 K. The sample and microscope are loaded together onto the cryostat, the chamber is pumped out, and the microscope and sample are lowered slowly into the cryostat to avoid damaging the piezo-tubes. At 4.2 K the piezo-tube response to applied voltage is diminished by a factor of 5.5. This means that coarse positioning of the sample can take much longer than it did at room temperature (generally it's even slower than the factor of 5.5 would suggest because there's a minimum amount of force required to overcome static friction and move the sample disc over microscopic imperfections.) Following the plan of walking in the +Y direction

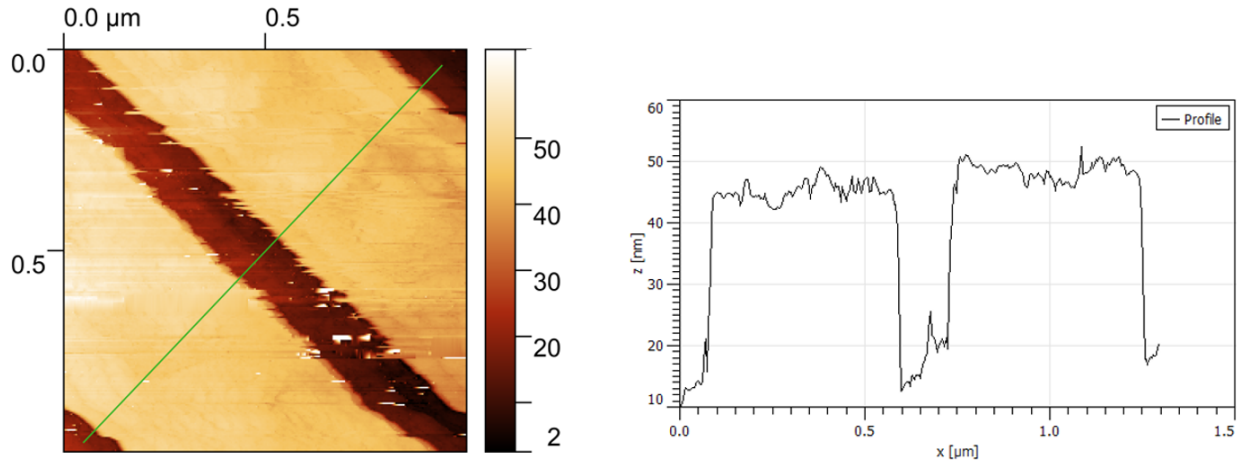


Figure 7.6 (Left) Room temperature STM 1 x 1 μm topography on an S-TI-S device. STM topography is higher-resolution than AFM topography, but the scan range is more limited. STM topography is also generally noisier than AFM topography at room temperature. At room temperature, it is possible to fit two fingers in one scan window. (Right) The height profile along the green line in the topography image. The Nb is 32 ± 3 nm tall, as expected.

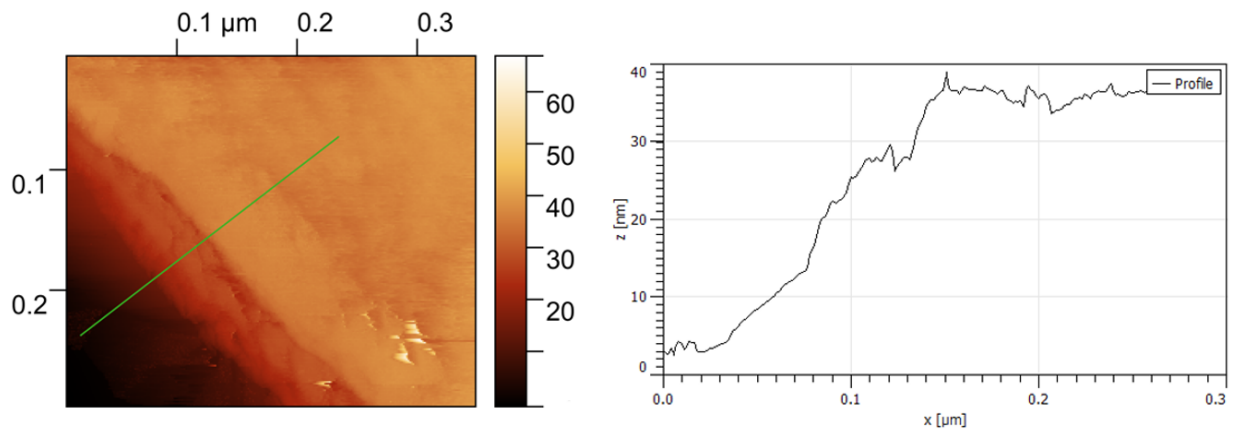


Figure 7.7 (Left) STM topography on the edge of a Nb finger at 4.2 K. The topography shows an extended, sloping edge of the finger. (Right) The height profile along the green line in the topography image.

saves wasted time randomly searching for the pattern. With no visual guides at low temperature, the only indication of the pattern is with STM topography. Figure 7.7 is low temperature topography that shows clear evidence of a finger edge. The topography range is limited to $0.35 \times 0.35 \mu\text{m}$ at 4.2 K. This is barely larger than the gaps between fingers. The height of the fingers reproduces nicely at low temperature, but the particular finger edge captured in this measurement has a sloped edge.

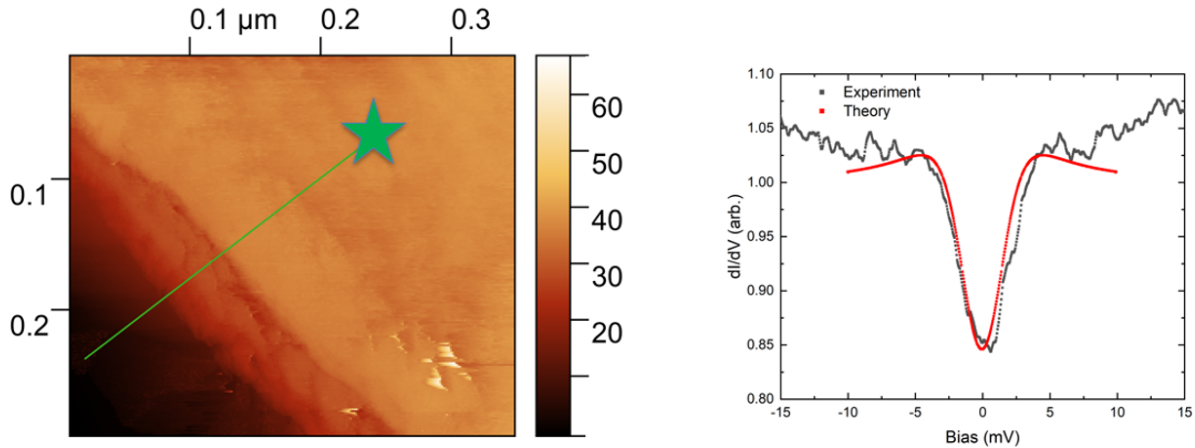


Figure 7.8 (Left) The same STM topography as shown in Figure 7.7. A green star shows a single spectroscopy location. (Right) STM spectroscopy taken at the green star. In black is the experimental data showing a clear gap at zero bias. A theoretical BCS spectroscopy is plotted in red. The theory uses the mean free path of the Cooper pairs as the only free parameter with the superconducting energy gap at zero temperature fixed at the nominal value for Nb at $\Delta = 3.05$ meV and the temperature fixed at $T = 4.2$ K.

The next step in the experiment is spectroscopy. Spectroscopy confirms that the tip is on a Nb finger, as the spectroscopy exhibits a clear superconducting energy gap at zero bias, as shown in Figure 7.8. The experimental data is compared to a theoretical BCS plot. It was unclear going into the experiment if Nb would be superconducting at 30 nm thick. Superconductivity theoretically only requires dimensions to be at least half as long as the coherence length, but in practice thin film superconductors have diminished T_C [32]. ***The thinnest superconducting Nb film I could find in the literature was 180 nm in this paper [32] correct me if I'm wrong, Stuart.*** Niobium has a coherence length of $\xi = 38$ nm, so 19 nm of Nb is theoretically sufficient to support superconductivity. Observations of the expected topography and spectroscopy prove the concept of the experiment is valid. All that is left is to combine the topography and spectroscopy with an external applied magnetic field and search for zero energy states. Soon after the data in Figure 7.7 was taken, the tip crashed and the liquid helium ran out. Continuing this experiment will be left to the next Tessmer group graduate student, Elinore McLain.

CHAPTER 8

CONCLUSIONS

The gas exposure experiment concluded with solid experimental evidence of a novel N₂ exposure effect on Bi₂Se₃. With the supporting theory and *ab initio* simulations, we believe that N₂ dissociates into N atoms in the presence of Se vacancy pairs. This undoes the n-type doping of the Se vacancies, moving the Dirac point closer to the Fermi level. This effect should be considered in future work on this material. It's often desirable for the Dirac cone to be centered on the Fermi level, so this also provides a simple method for restoring that condition for samples with Se vacancies.

A great deal of progress was made on the Josephson vortex experiment. Now there is a recipe that consistently produces high-quality junctions. The next step for this experiment is to take the devices and image vortices with the conductance mapping technique. After that, it's possible that these vortices can be characterized with a scanning quantum dot measurement probe designed by the last PhD to come out of the Tessmer group, Eric Goodwin. Combining these two experiments together will be left to Elinore McLain.

BIBLIOGRAPHY

- [1] Foxe T. T. Hunt B. D. Rogers C. Kleinsasser A. W. Buhrman R. A. Reactive ion etching of niobium. *Journal of Vacuum Science and Technology*, 19(4):1394, jun 1998. ISSN 0022-5355. doi: 10.1116/1.571217. URL <https://avs.scitation.org/doi/abs/10.1116/1.571217>.
- [2] J. Bardeen. Tunnelling from a many-particle point of view. *Phys. Rev. Lett.*, 6:57–59, Jan 1961. doi: 10.1103/PhysRevLett.6.57. URL <https://link.aps.org/doi/10.1103/PhysRevLett.6.57>.
- [3] K. Besocke. An easily operable scanning tunneling microscope. *Surface Science*, 181(1): 145–153, 1987. ISSN 0039-6028. doi: [https://doi.org/10.1016/0039-6028\(87\)90151-8](https://doi.org/10.1016/0039-6028(87)90151-8). URL <https://www.sciencedirect.com/science/article/pii/0039602887901518>.
- [4] P. Cherin and P. Unger. Refinement of the crystal structure of α -monoclinic Se. *Acta Crystallographica Section B*, 28(1):313–317, Jan 1972. doi: 10.1107/S0567740872002249. URL <https://doi.org/10.1107/S0567740872002249>.
- [5] Jixia Dai, Damien West, Xueyun Wang, Yazhong Wang, Daniel Kwok, S.-W. Cheong, S. B. Zhang, and Weida Wu. Toward the intrinsic limit of the topological insulator Bi_2Se_3 . *Phys. Rev. Lett.*, 117:106401, Aug 2016. doi: 10.1103/PhysRevLett.117.106401. URL <https://link.aps.org/doi/10.1103/PhysRevLett.117.106401>.
- [6] D. C. Frost, C. A. McDowell, and Cecil Edwin Henry Bawn. The dissociation energy of the nitrogen molecule. *Proceedings of the Royal Society of London. Series A. Mathematical and Physical Sciences*, 236(1205):278–284, 1956. doi: 10.1098/rspa.1956.0135. URL <https://royalsocietypublishing.org/doi/abs/10.1098/rspa.1956.0135>.
- [7] Liang Fu and C. L. Kane. Topological insulators with inversion symmetry. *Phys. Rev. B*, 76:045302, Jul 2007. doi: 10.1103/PhysRevB.76.045302. URL <https://link.aps.org/doi/10.1103/PhysRevB.76.045302>.
- [8] Liang Fu and C. L. Kane. Superconducting proximity effect and majorana fermions at the surface of a topological insulator. *Phys. Rev. Lett.*, 100:096407, Mar 2008. doi: 10.1103/PhysRevLett.100.096407. URL <https://link.aps.org/doi/10.1103/PhysRevLett.100.096407>.
- [9] Michael Gottschalk, Mal-Soon Lee, Eric Goodwin, Camille Mikolas, Thomas Chasapis, Duck Young Chung, Mercouri Kanatzidis, S. D. Mahanti, and Stuart Tessmer. Evidence for nitrogen gas surface doping of the Bi_2Se_3 topological insulator, 2020. URL <https://arxiv.org/abs/2004.01631>.

- [10] Christoph W Groth, Michael Wimmer, Anton R Akhmerov, and Xavier Waintal. Kwant: a software package for quantum transport. *New Journal of Physics*, 16(6):063065, jun 2014. doi: 10.1088/1367-2630/16/6/063065. URL <https://doi.org/10.1088/1367-2630/16/6/063065>.
- [11] Soumyajyoti Haldar, Hakkim Vovusha, Manoj Kumar Yadav, Olle Eriksson, and Biplab Sanyal. Systematic study of structural, electronic, and optical properties of atomic-scale defects in the two-dimensional transition metal dichalcogenides mX_2 ($m = \text{Mo, w}$; $x = \text{S, se, te}$). *Phys. Rev. B*, 92:235408, Dec 2015. doi: 10.1103/PhysRevB.92.235408. URL <https://link.aps.org/doi/10.1103/PhysRevB.92.235408>.
- [12] E. H. Hall. On a new action of the magnet on electric currents. *American Journal of Mathematics*, 2(3):287–292, 1879. ISSN 00029327, 10806377. URL <http://www.jstor.org/stable/2369245>.
- [13] M. Z. Hasan and C. L. Kane. Colloquium: Topological insulators. *Rev. Mod. Phys.*, 82:3045–3067, Nov 2010. doi: 10.1103/RevModPhys.82.3045. URL <https://link.aps.org/doi/10.1103/RevModPhys.82.3045>.
- [14] D. Hsieh, Y. Xia, D. Qian, L. Wray, J. H. Dil, F. Meier, J. Osterwalder, L. Patthey, J. G. Checkelsky, N. P. Ong, A. V. Fedorov, H. Lin, A. Bansil, D. Grauer, Y. S. Hor, R. J. Cava, and M. Z. Hasan. A tunable topological insulator in the spin helical dirac transport regime. *Nature*, 460(7259):1101–1105, Aug 2009. ISSN 1476-4687. doi: 10.1038/nature08234. URL <https://doi.org/10.1038/nature08234>.
- [15] D. A. Ivanov. Non-abelian statistics of half-quantum vortices in p -wave superconductors. *Phys. Rev. Lett.*, 86:268–271, Jan 2001. doi: 10.1103/PhysRevLett.86.268. URL <https://link.aps.org/doi/10.1103/PhysRevLett.86.268>.
- [16] C. L. Kane and E. J. Mele. Quantum spin hall effect in graphene. *Phys. Rev. Lett.*, 95:226801, Nov 2005. doi: 10.1103/PhysRevLett.95.226801. URL <https://link.aps.org/doi/10.1103/PhysRevLett.95.226801>.
- [17] A Yu Kitaev. Unpaired majorana fermions in quantum wires. *Physics-Uspekhi*, 44(10S):131–136, oct 2001. doi: 10.1070/1063-7869/44/10s/s29. URL <https://doi.org/10.1070/1063-7869/44/10s/s29>.
- [18] K. v. Klitzing, G. Dorda, and M. Pepper. New method for high-accuracy determination of the fine-structure constant based on quantized hall resistance. *Phys. Rev. Lett.*, 45:494–497, Aug 1980. doi: 10.1103/PhysRevLett.45.494. URL <https://link.aps.org/doi/10.1103/PhysRevLett.45.494>.
- [19] Mohammad Koleini, Thomas Frauenheim, and Binghai Yan. Gas doping on the topological insulator Bi_2Se_3 surface. *Phys. Rev. Lett.*, 110:016403, Jan 2013. doi: 10.1103/PhysRevLett.110.016403. URL <https://link.aps.org/doi/10.1103/PhysRevLett.110.016403>.

- [20] Yaacov E. Kraus, Assa Auerbach, H. A. Fertig, and Steven H. Simon. Majorana fermions of a two-dimensional $p_x + ip_y$ superconductor. *Phys. Rev. B*, 79:134515, Apr 2009. doi: 10.1103/PhysRevB.79.134515. URL <https://link.aps.org/doi/10.1103/PhysRevB.79.134515>.
- [21] G. Kresse and J. Hafner. Ab initio molecular dynamics for liquid metals. *Phys. Rev. B*, 47: 558–561, Jan 1993. doi: 10.1103/PhysRevB.47.558. URL <https://link.aps.org/doi/10.1103/PhysRevB.47.558>.
- [22] G. Kresse and D. Joubert. From ultrasoft pseudopotentials to the projector augmented-wave method. *Phys. Rev. B*, 59:1758–1775, Jan 1999. doi: 10.1103/PhysRevB.59.1758. URL <https://link.aps.org/doi/10.1103/PhysRevB.59.1758>.
- [23] Thomas D. Kühne, Marcella Iannuzzi, Mauro Del Ben, Vladimir V. Rybkin, Patrick Seewald, Frederick Stein, Teodoro Laino, Rustam Z. Khaliullin, Ole Schütt, Florian Schiffmann, Dorothea Golze, Jan Wilhelm, Sergey Chulkov, Mohammad Hossein Bani-Hashemian, Valéry Weber, Urban Borštnik, Mathieu Taillefumier, Alice Shoshana Jakobovits, Alfio Lazzaro, Hans Pabst, Tiziano Müller, Robert Schade, Manuel Guidon, Samuel Andermatt, Nico Holmberg, Gregory K. Schenter, Anna Hehn, Augustin Bussy, Fabian Belleflamme, Gloria Tabacchi, Andreas Glöß, Michael Lass, Iain Bethune, Christopher J. Mundy, Christian Plessl, Matt Watkins, Joost VandeVondele, Matthias Krack, and Jürg Hutter. CP2K: An electronic structure and molecular dynamics software package - Quickstep: Efficient and accurate electronic structure calculations. *The Journal of Chemical Physics*, 152(19):194103, may 2020. ISSN 0021-9606. doi: 10.1063/5.0007045. URL <https://aip.scitation.org/doi/abs/10.1063/5.0007045>.
- [24] Irving Langmuir. The adsorption of gases on plane surfaces of glass, mica and platinum. *Journal of the American Chemical Society*, 40(9):1361–1403, 1918. doi: 10.1021/ja02242a004. URL <https://doi.org/10.1021/ja02242a004>.
- [25] Ettore Majorana. Teoria simmetrica dell’elettrone e del positrone. *Il Nuovo Cimento (1924-1942)*, 14(4):171, Sep 2008. ISSN 1827-6121. doi: 10.1007/BF02961314. URL <https://doi.org/10.1007/BF02961314>.
- [26] John P. Perdew, Kieron Burke, and Matthias Ernzerhof. Generalized gradient approximation made simple. *Phys. Rev. Lett.*, 77:3865–3868, Oct 1996. doi: 10.1103/PhysRevLett.77.3865. URL <https://link.aps.org/doi/10.1103/PhysRevLett.77.3865>.
- [27] N. Read and Dmitry Green. Paired states of fermions in two dimensions with breaking of parity and time-reversal symmetries and the fractional quantum hall effect. *Phys. Rev. B*, 61:10267–10297, Apr 2000. doi: 10.1103/PhysRevB.61.10267. URL <https://link.aps.org/doi/10.1103/PhysRevB.61.10267>.
- [28] Dimitri Roditchev, Christophe Brun, Lise Serrier-Garcia, Juan Carlos Cuevas, Henrique Loiola Bessa, Milorad Vlado Milošević, François Debontridder, Vasily Stolyarov, and Tristan

- Cren. Direct observation of Josephson vortex cores. *Nature Physics*, page 23, 2015. doi: 10.1038/NPHYS3240. URL www.nature.com/naturephysics.
- [29] Megan Romanowich, Mal-Soon Lee, Duck-Young Chung, S. D. Mahanti, Mercuri G. Kanatzidis, and Stuart H. Tessmer. Interplay of topological surface and bulk electronic states in Bi_2Se_3 . *Phys. Rev. B*, 87:085310, Feb 2013. doi: 10.1103/PhysRevB.87.085310. URL <https://link.aps.org/doi/10.1103/PhysRevB.87.085310>.
- [30] Philipp R  bmann, Phivos Mavropoulos, and Stefan Bl  gel. Lifetime and surface-to-bulk scattering off vacancies of the topological surface state in the three-dimensional strong topological insulators Bi_2Te_3 and Bi_2Se_3 . *Journal of Physics and Chemistry of Solids*, 128:258–264, 2019. ISSN 0022-3697. doi: <https://doi.org/10.1016/j.jpcs.2017.12.009>. URL <https://www.sciencedirect.com/science/article/pii/S0022369717313951>. Spin-Orbit Coupled Materials.
- [31] M M Sharma, Prince Sharma, N K Karn, Martin Leijnse, and Karsten Flensberg. Introduction to topological superconductivity and Majorana fermions. *Semiconductor Science and Technology*, 27(12):124003, nov 2012. ISSN 0268-1242. doi: 10.1088/0268-1242/27/12/124003. URL <https://iopscience.iop.org/article/10.1088/0268-1242/27/12/124003><https://iopscience.iop.org/article/10.1088/0268-1242/27/12/124003/meta>.
- [32] J Sosniak and G W Hull. Superconductivity of Niobium Thin Films Deposited by dc Diode Sputtering. *Journal of Applied Physics*, 38:4390, 1967. doi: 10.1063/1.1709136. URL <https://doi.org/10.1063/1.1709136>, 4390.
- [33] Michiel Sprik and Giovanni Ciccotti. Free energy from constrained molecular dynamics. *The Journal of Chemical Physics*, 109(18):7737, nov 1998. ISSN 0021-9606. doi: 10.1063/1.477419. URL <https://aip.scitation.org/doi/abs/10.1063/1.477419>.
- [34] L.W. Swanson and A.E. Bell. Recent advances in field electron microscopy of metals. In L. Marton and Claire Marton, editors, *Advances in Electronics and Electron Physics*, volume 32 of *Advances in Electronics and Electron Physics*, pages 193–309. Academic Press, 1973. doi: [https://doi.org/10.1016/S0065-2539\(08\)60236-X](https://doi.org/10.1016/S0065-2539(08)60236-X). URL <https://www.sciencedirect.com/science/article/pii/S006525390860236X>.
- [35] D. J. Thouless. Topological interpretations of quantum hall conductance. *Journal of Mathematical Physics*, 35(10):5362–5372, 1994. doi: 10.1063/1.530757. URL <https://doi.org/10.1063/1.530757>.
- [36] S. Urazhdin, D. Bilc, S. H. Tessmer, S. D. Mahanti, Theodora Kyratsi, and M. G. Kanatzidis. Scanning tunneling microscopy of defect states in the semiconductor Bi_2Se_3 . *Phys. Rev. B*, 66:161306, Oct 2002. doi: 10.1103/PhysRevB.66.161306. URL <https://link.aps.org/doi/10.1103/PhysRevB.66.161306>.

- [37] Lee A. Walsh, Avery J. Green, Rafik Addou, Westly Nolting, Christopher R. Cormier, Adam T. Barton, Tyler R. Mowll, Ruoyu Yue, Ning Lu, Jiyoung Kim, Moon J. Kim, Vincent P. LaBella, Carl A. Ventrice, Stephen McDonnell, William G. Vandenberghe, Robert M. Wallace, Alain Diebold, and Christopher L. Hinkle. Fermi level manipulation through native doping in the topological insulator Bi_2Se_3 . *ACS Nano*, 12(6):6310–6318, 2018. doi: 10.1021/acsnano.8b03414. URL <https://doi.org/10.1021/acsnano.8b03414>. PMID: 29874037.
- [38] Dan Wang, Min Zhang, Ligang Liu, Xinyou An, Xiaoyang Ma, Yongzheng Luo, and Tingting Song. First-principles study of electronic, magnetic and optical properties of n doping topological insulator Bi_2Se_3 . *Superlattices and Microstructures*, 132:106161, 2019. ISSN 0749-6036. doi: <https://doi.org/10.1016/j.spmi.2019.106161>. URL <https://www.sciencedirect.com/science/article/pii/S0749603619305075>.
- [39] Wikipedia. Scanning tunneling microscope. https://en.wikipedia.org/wiki/Scanning_tunneling_microscope, September 2022.
- [40] Stan Gheorghe Solares Santiago D Schwarz U D Baykara M Z. Frequency, amplitude, and phase measurements in contact resonance atomic force microscopies. *Beilstein J. Nanotechnol.*, 5:278–288, 2014. doi: 10.3762/bjnano.5.30.
- [41] Haijun Zhang, Chao Xing Liu, Xiao Liang Qi, Xi Dai, Zhong Fang, and Shou Cheng Zhang. Topological insulators in Bi_2Se_3 , Bi_2Te_3 and Sb_2Te_3 with a single Dirac cone on the surface. *Nature Physics* 2009 5:6, 5(6):438–442, may 2009. ISSN 1745-2481. doi: 10.1038/nphys1270. URL <https://www.nature.com/articles/nphys1270>.